Universitat Autònoma de Barcelona

Measurement of the W mass from the $WW \to q\bar{q}q\bar{q}$ channel with the ALEPH detector [1]

Imma Riu
Universitat Autònoma de Barcelona
Departament de Física
Institut de Física d'Altes Energies
Edifici Cn
E-08193 Bellaterra (Barcelona)

December 1998

[1] Ph.D. Dissertation

Contents

List of Figures

List of Tables

Chapter 1

Introduction

During almost 40 years the Physics model of electroweak and strong interactions between particles, the Standard Model [1] (SM), has successfully survived every check. In recent years new powerful tests of the model have been performed, mainly at LEP but also at SLC and at the Tevatron. At LEP, the high statistics data collected at the Z^0 peak allowed very accurate measurements of the parameters of the SM and provided a very good test at the quantum level of the electroweak theory. The mass of the Z^0 boson was measured with a relative error of 0.002% while the mass of the W boson was measured at hadron colliders with a relative error of 0.1%.

In June 1996, a second phase of LEP (LEP2) started at a centre-of-mass energy of 161 GeV, the kinematical threshold of W pair production. For the first time at LEP, the interest was focussed in W physics and the W mass measurement became one of the main purposes of this running period. Its accurate measurement can constrain the allowed range of values of the mass of the Higgs boson, the only particle of the SM not discovered yet, as well as indicate the existence of new physics beyond the SM.

At 161 GeV the W's are produced at rest and the sensitivity of the $W^+W^\perp$ cross-section to the W mass allowed a first measurement of the W boson mass at LEP. In November 1996 the centre-of-mass energy was raised up to 172 GeV. At this energy, the W cross-section is big enough to allow the reconstruction of the W decay products. Making use of a very good performance, LEP reached an unprecedented centre-of-mass energy of 183 GeV in 1997, and high statistics

(compared to what was collected at 172 GeV) were accumulated allowing the best accurate W mass measurement at LEP so far. Even higher statistics with higher centre-of-mass energies are expected to be accumulated by LEP during the coming years, hopefully allowing a final accuracy of 30 MeV for the W mass.

In this thesis, the measurement of the W mass using the hadronic channel in the data collected by ALEPH at 172 GeV and 183 GeV centre-of-mass energies is presented. The direct reconstruction method is used to determine the mass of the W boson. Particular problems to the fully hadronic decay channel, which come from the large background contamination, the important distortions due to fragmentation, and detector effects when reconstructing the hadronic jets, are explained. Due to the similarities of the signal and background processes, the selection is based on a multidimensional analysis which achieves a good signal-background separation. Taking the algorithm which best pairs the jets, the invariant masses of both W's can be reconstructed, and using a kinematical fit, their resolutions are improved. The W mass is measured using a reweighting procedure that reweights the Monte Carlo with a known W mass to the W mass value which best fits to the data.

Important systematic uncertainties to the W mass measurement from the hadronic channel are the possible final state interactions, that would obscure the W decays which may no longer be considered independent. Detailed interconnection effects studies are described.

Chapter 2 describes the theoretical framework of the analysis. Chapter 3 gives a description of the ALEPH detector emphasizing the parts of the apparatus used for the analysis. The description of the measurement of the W mass in the hadronic channel using the data collected at 172 GeV centre-of-mass energy is detailed in chapter 4. In chapter 5 the W mass is measured with the data collected at 183 GeV centre-of-mass energy. The combination of both results, together with the combination with the other LEP and hadron collider W mass measurements are given in chapter 6. Finally, the conclusions are given in chapter 7. A list of appendices give some more detailed information on the formulae used.

Chapter 2

Theoretical framework

After a brief introduction of the Standard Model theory in section 2.1, the W pair production in $e^+e^\perp$ annihilation is described. The $W^+W^\perp$ cross-section is detailed in section 2.3, including the W width and a discussion about the gauge invariance. Radiative corrections are given in section 2.4. The role of the W mass in precision tests of the Standard Model is discussed in section 2.5 and details on the W mass measurement at LEP are given in section 2.6. Finally, the interconnection phenomena are described in section 2.7.

2.1 The Standard Model structure

The Standard Model (SM) is a gauge theory, based on the group $SU(3)_C \otimes SU(2)_L \otimes U(1)_Y$, describing electroweak and strong interactions between particles. The model describing electroweak interactions was firstly introduced by Glashow, Weinberg and Salam [1]. Later, through the GIM mechanism (Glashow, Iliopoulos and Maiani) [2], the electroweak interactions of quarks were also introduced. This theory predicted the existence of neutral and charged currents mediated by the gauge bosons ($W^\pm$, Z^0) which were for the first time observed in the $p\bar{p}$ collider at CERN in 1983.

The unification of the electromagnetic (mediated by photons) and weak interactions (mediated by $W^\pm$ and Z^0) is done by requiring a gauge invariance under the $SU(2)_L \otimes U(1)_Y$ transformation group. As a result of a spontaneous symmetry breaking process, the vector bosons acquire masses without breaking the local

gauge invariance of the lagrangian, and a new scalar particle, the Higgs, is predicted to exist although it has not been observed experimentally yet. The renormalization was established in 1971 by 't Hooft [3] ensuring the systematic cancellations of divergences order by order of the perturbative expansion of the hamiltonian and its absorption in the definition of a finite set of "bare" parameters. The strong interaction between quarks (mediated by eight massless gluons) is included in the Standard Model by a field theory, local gauge invariant under the symmetry group $\mathrm{SU(3)_C}$.

The Standard Model consists of fermionic families of quarks and leptons, gauge bosons and the Higgs boson. There are experimental results showing the existence of only three families with the hypothesis of light neutrinos [4]. The fermionic matter content is organized in a 3-fold family structure, as shown in table 2.1. An antiparticle corresponds to each particle with the same mass and opposite quantum numbers. The left- (right-) handed fields transform as $\mathrm{SU(2)_L}$ doublets (singlets). Each quark appears in three different 'colours' and transform as $\mathrm{SU(3)_C}$ via the exchange of gluons. The $\{d', s', b'\}$ weak isospin eigenstates are related to the $\{d, s, b\}$ mass eigenstates through the unitarity matrix of Cabibbo-Kobayashi-Maskawa [5], which depends on three mixing angles and a phase which have to be determined experimentally. This phase is responsible for the CP symmetry breaking in the Standard Model and it is widely believed that CP non-conservation in the early Universe is one of the sources of the apparent imbalance between matter and antimatter. Recent experiments [6] seem to indicate the existence of $\nu_\mu - \nu_\tau$ oscillations, thus introducing flavour mixing in the leptonic sector and invalidating the hypothesis of massless neutrinos.

The mass of the Higgs boson is constrained by direct searches at LEP to be greater than $89.8\,\mathrm{GeV}/c^2$ [7]. The precise electroweak measurements at LEP have some sensitivity to $\log(M_\mathrm{H}/\mathrm{GeV})$ through loop corrections, and have constrained M_H to be below $280\,\mathrm{GeV}/c^2$ at 95% confidence level [8]. The next generation machine, the LHC, as well as the data collected by LEP2 and Tevatron in the near future should be able to decide whether the simplest Higgs model is correct or not. At LEP2, the precise measurement of M_W will be of big importance in order to place more stringent limits on the mass of the Higgs, as well as further constrain the allowed regions in the space of parameters of the Minimal Supersymmetric Standard Model (MSSM).

Leptons

$$\begin{array}{ccc} \begin{pmatrix} \nu_{e_L} \\ e_L \end{pmatrix}_{Y=\perp\frac{1}{2}} & \begin{pmatrix} \nu_{\mu_L} \\ \mu_L \end{pmatrix}_{Y=\perp\frac{1}{2}} & \begin{pmatrix} \nu_{\tau_L} \\ \tau_L \end{pmatrix}_{Y=\perp\frac{1}{2}} \\ \begin{pmatrix} e_R \end{pmatrix}_{Y=\perp 1} & \begin{pmatrix} \mu_R \end{pmatrix}_{Y=\perp 1} & \begin{pmatrix} \tau_R \end{pmatrix}_{Y=\perp 1} \end{array}$$

Quarks

$$\begin{array}{ccc} \begin{pmatrix} u_L \\ d'_L \end{pmatrix}_{Y=\frac{1}{6}} & \begin{pmatrix} c_L \\ s'_L \end{pmatrix}_{Y=\frac{1}{6}} & \begin{pmatrix} t_L \\ b'_L \end{pmatrix}_{Y=\frac{1}{6}} \\ \begin{pmatrix} u_R \end{pmatrix}_{Y=\frac{2}{3}} & \begin{pmatrix} c_R \end{pmatrix}_{Y=\frac{2}{3}} & \begin{pmatrix} t_R \end{pmatrix}_{Y=\frac{2}{3}} \\ \begin{pmatrix} d'_R \end{pmatrix}_{Y=\perp\frac{1}{3}} & \begin{pmatrix} s'_R \end{pmatrix}_{Y=\perp\frac{1}{3}} & \begin{pmatrix} b'_R \end{pmatrix}_{Y=\perp\frac{1}{3}} \end{array}$$

Table 2.1: Gauge group representations of fermion fields. Y is the *hypercharge* quantum number.

2.2 W pair production in e^+e^- annihilation

The W bosons at LEP2 are produced in pairs by the annihilation of electrons and positrons: $e^+e^\perp \to W^+W^\perp$.

At tree-level (lowest order) a W pair is produced either through the *annihilation* diagram $e^+e^\perp$ into a Z^0 boson or a virtual γ (first and second diagrams of figure 2.1), or via the double *conversion* diagram with a t-channel neutrino exchange [1] (third diagram of the same figure). This set of processes are the `CC03` diagrams—three Charged-Current processes.

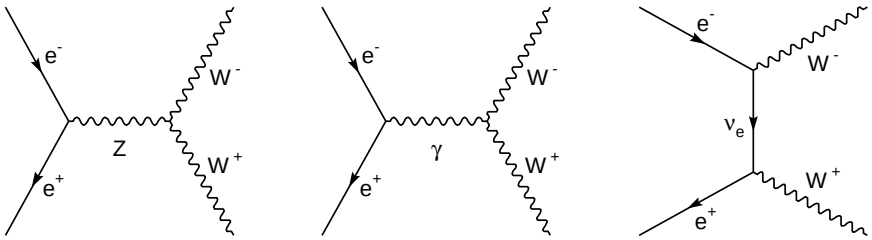

Figure 2.1: `CC03` diagrams of W^+W^- production.

[1] The Higgs boson exchange diagram is neglected since it is suppressed by a factor m_e/M_W.

A second phase of the process follows when each of the initial W's decay into two fermions, and produces a detectable final state of four fermions.

Besides the $e^+e^\perp \to W^+W^\perp$ production other four-fermion processes like

$$\begin{aligned} e^+e^\perp &\to Z^0Z^0\,, \\ e^+e^\perp &\to We\nu_e\,, \\ e^+e^\perp &\to Z^0e^+e^\perp, \\ e^+e^\perp &\to Z^0\nu_e\bar{\nu}_e \end{aligned} \tag{2.1}$$

occur at LEP2. The actual measurable final states in the above reactions are their decay products. The number of Feynman diagrams contributing to a given final state can be very large and the same four-fermion final state can originate from several reactions. For example, $e^+e^\perp\nu_e\bar{\nu}_e$ can originate from any of the reactions above. To distinguish them, they are called *signal* when coming from $W^+W^\perp$ production and *background* when coming from other reactions. A classification of the four-fermion processes follows.

Classification of four-fermion processes

In general all possible four-fermion final states are subdivided into two classes (for certain final states the two classes overlap):

- Charged-Current processes ('`CC`'-type): via the production of (up, antidown) and (down, antiup) fermion pairs. These are the contributing processes to the $W^+W^\perp$ signal events.
- Neutral-Current processes ('`NC`'-type): via a pair of virtual neutral vector bosons. These diagrams contribute to the background processes.

One may distinguish three different cases for '`CC`'-type processes, all of them containing the `CC03` processes as a subset:

(i) The `CC11` family.

The two fermion pairs are different and the final state does not contain identical particles, neither electrons nor electron neutrinos. A typical four-quark process with 11 contributing Feynman diagrams is $u\bar{d}s\bar{c}$.

(ii) The `CC20` family.

The final state contains one $e^\pm$ together with its neutrino. The additional diagrams to (i) have a t-channel gauge boson exchange. In figure 2.2 all the diagrams contributing to $e^+e^\perp \to e^\perp \nu_e u\bar{d}$ are shown. Graphs numbered 11 to 14 are called *bremsstrahlung* diagrams (graphs 4 to 10 are also bremsstrahlung diagrams of a W from Bhabha-like scattering, usually called singly-resonant diagrams) while graphs numbered 15 and 16 are called *fusion* diagrams, and graphs numbered 17 to 20 *multiperipheral* diagrams.

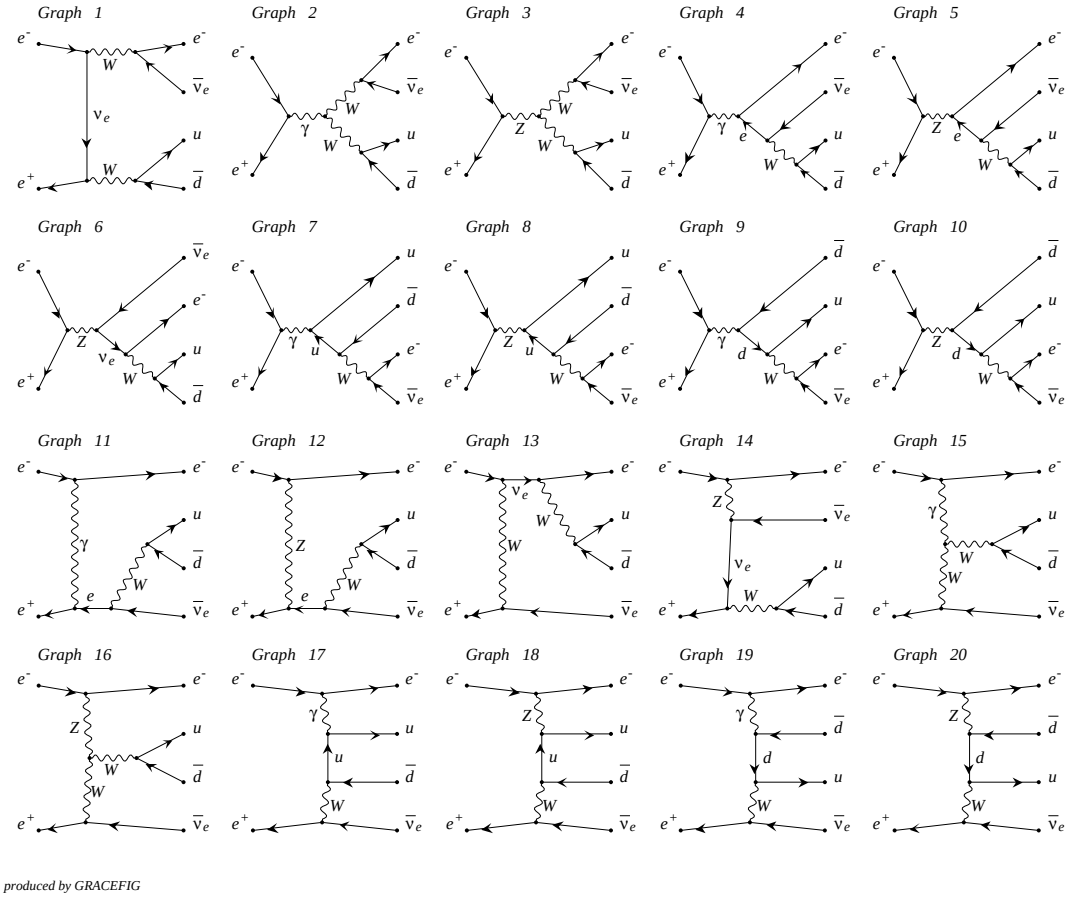

Figure 2.2: Set of the 20 charged current diagrams (`CC20`) contributing to the process $e^+e^- \to e^-\nu_e u\bar{d}$. The first three diagrams correspond to the `CC03` diagrams containing two resonating W bosons. The figure has been produced using the GRACE [9] programme.

(iii) The `mix43` and `mix56` families.

Two mutually charge conjugated fermion pairs are produced. Differing from the cases (i) and (ii), the diagrams may contain neutral boson exchanges ('`NC`'-type diagrams), and therefore these families are named `mix-`.

A classification of the final states corresponding to the '`NC`'-type diagrams is divided into the families: `NC32` when the final state does not contain electrons or identical fermions; `NC48` and `NC21` when taking the final states involving electrons and ν_e respectively, except the ones containing two $e^+e^\perp$ or $\nu_e\bar{\nu}_e$ pairs; `NC4·16` when identical fermions not being e, ν_e in the final states are taken; among others.

2.3 W^+W^- cross-section

Schematically the cross-section of the process $e^+e^\perp \to 4f\ (+\gamma, g, ...)$, $\sigma_{\rm tot}$, can be decomposed into signal (σ) and background ($\sigma_{\rm bkg}$) contributions although neither contribution is separately exactly gauge invariant nor experimentally distinguishable in general:

$$\sigma_{\rm tot} = \sigma + \sigma_{\rm bkg}. \tag{2.2}$$

$\sigma_{\rm bkg}$ is the background contribution from, for example, non-resonant diagrams (e.g. $e^+e^\perp \to \mu^+\nu_\mu W^\perp$) and QCD contributions $e^+e^\perp \to q\bar{q}gg(\gamma), q\bar{q}q\bar{q}(\gamma)$ to the four-jet final state. The $W^+W^\perp$ contribution (σ) can be further decomposed in the form:

$$\sigma = \sigma^0\ (1 + \delta_{\rm EW} + \delta_{\rm QCD}), \tag{2.3}$$

where the various terms correspond to:

(i) σ^0: the Born contribution from the three `CC03` diagrams (figure 2.1) for $e^+e^\perp \to W^+W^\perp$.

(ii) $\delta_{\rm EW}$: higher-order electroweak radiative corrections, including loop corrections, real photon emission, etc.

(iii) $\delta_{\rm QCD}$: higher-order QCD corrections to $W^+W^\perp$ final states containing quark pairs. They can lead to additional jets in the final state and affect the reconstruction of the W boson.

More detailed descriptions of (i) and (ii) are given in section 2.4.

2.3.1 The W^+W^- on-shell cross-section

The expression of the cross-section which results when neglecting the width of the W boson is called *on-shell* cross-section, different from the one when including the W boson width, called *off-shell* cross-section. The total on-shell cross-section at lowest order (Born approximation) can be analytically calculated, leading to the following expression:

$$\sigma^0_{\mathrm{on}\perp\mathrm{shell}} \sim \frac{\pi\alpha^2}{s} \cdot \frac{1}{4\sin^4\theta_W} \cdot 4\beta + \mathcal{O}(\beta^3), \tag{2.4}$$

where θ_W is the Weinberg angle, α is the electroweak coupling constant, and $\beta = \sqrt{1 - 4M_{\mathrm{W}}^2/s}$ (M_{W} being the W boson mass).

The contribution to the cross-section proportional to β is due to the t-channel (S-wave threshold behaviour), while the contribution from the s-channel and the s–t interference is proportional to β^3 (P-wave behaviour) [2]. Hence, in the threshold region the t-channel neutrino exchange is the dominant contribution to the cross-section. In figure 2.3 the rapid increase of the $W^+W^\perp$ on-shell cross-section in the threshold region is shown.

2.3.2 The W width

The width of the W boson is the responsible for the 'off-shellness' of the W boson. Its precise measurement, like the Z^0 width measurement, may yield evidence for non-standard decays involving, for example, supersymmetric particles or heavy quarks [11]. It importantly distorts the W line-shape close to the threshold (see figure 2.3).

The W bosons may be described as resonances with a Breit-Wigner shape distorted by effects such as detector response, background contamination, initial state radiation, etc. The W boson Breit-Wigner has a total finite width (Γ_{W}) (to avoid singularities, see section 2.3.4) which corresponds to the sum of the partial decay width $\Gamma_{\mathrm{W}\to f_i f'_j}$ of each of the W channels: leptonic decay ($W \to \nu_i l_i$ where i means the lepton specie) 32.2% of the time, and hadronic decay ($W \to u_i d_j$ where i and j mean the different quark combinations: ud and cs, as the decay involving a b quark

[2] This is a consequence of CP conservation, fermion-helicity conservation in the initial state, and the orthogonality of different partial waves [10].

is negligible) 67.8% of the time [12] [3]. The partial W width for each decay channel at lowest order can be obtained from the matrix element:

$$\Gamma^{\mathrm{Born}}_{\mathrm{W}\to f_i f'_j} = \frac{\alpha}{6} \cdot \frac{M_{\mathrm{W}}}{2\,\sin^2\theta_W} \cdot |V_{ij}|^2 N_C^f, \tag{2.5}$$

where massless fermions are assumed. For leptonic decays the mixing matrix (V_{ij}) is diagonal and the colour factor (N_C^f) equal to one; for hadronic decays V_{ij} is the relevant element of the CKM matrix, and (neglecting QCD corrections) N_C^f is three.

By summing over the partial decay widths and neglecting the fermion masses, a simple formula in the Born approximation for the total width is obtained:

$$\Gamma_{\mathrm{W}}^{\mathrm{Born}} \simeq \frac{3\alpha}{2} \cdot \frac{M_{\mathrm{W}}}{2\,\sin^2\theta_W}. \tag{2.6}$$

When taking into account electroweak and QCD radiative corrections—the electroweak corrections can be accounted for by parametrising the lowest order width in terms of G_μ (the Fermi constant determined from the muon lifetime) and M_{W} instead of α and $\sin^2\theta_{\mathrm{W}}$, and the QCD corrections are practically constant and equal to $2\alpha_s(M_{\mathrm{W}}^2)/(3\pi)$ where α_s is the strong coupling constant—an improved Born approximation for the partial widths is obtained [13]:

$$\begin{aligned}
\Gamma_{\mathrm{W}\to\ell_i\nu_i} &\simeq \frac{G_\mu M_{\mathrm{W}}^3}{6\sqrt{2}\pi}, \\
\Gamma_{\mathrm{W}\to u_i d_j} &\simeq \frac{G_\mu M_{\mathrm{W}}^3}{2\sqrt{2}\pi}|V_{ij}|^2 \left(1 + \frac{\alpha_s(M_{\mathrm{W}}^2)}{\pi}\right),
\end{aligned}$$

as well as for the total width:

$$\Gamma_{\mathrm{W}} \simeq \frac{3G_\mu M_{\mathrm{W}}^3}{2\sqrt{2}\pi} \left(1 + \frac{2\alpha_s(M_{\mathrm{W}}^2)}{3\pi}\right). \tag{2.7}$$

Note that Γ_{W} is proportional to the third power of M_{W}.

Concerning the impact of Γ_{W} on the determination of M_{W}, different points of view can be adopted. Either the total width of the W boson is extracted simultaneously with the mass, or a fixed Γ_{W} at its nominal value is imposed, or

[3] The $\mathrm{W^+W^-}$ decay channels can therefore be divided into: fully leptonic ($\mathrm{W^+W^-} \to \ell\nu\ell\nu$) with 10.4% branching ratio, semileptonic ($\mathrm{W^+W^-} \to \mathrm{qq}\ell\nu$) with 43.7% branching ratio, and hadronic ($\mathrm{W^+W^-} \to 4\mathrm{q}$) with 45.9% branching ratio.

the functional dependence $\Gamma_W = \Gamma_W(M_W)$ from eq. (2.7) of the Standard Model is imposed as a constraint. The world average W width experimental value is $\Gamma_W = 2.062 \pm 0.059\,\mathrm{GeV}/c^2$ measured at Tevatron [14], in agreement with the Standard Model prediction $\Gamma_W = 2.094 \pm 0.002\,\mathrm{GeV}/c^2$ [15].

2.3.3 The W^+W^- off-shell cross-section

The description of the W's as stable particles, neglecting its W width (on-shell), is only an approximation. They should be described as resonances with a finite width (off-shell) to avoid singularities inside the physical space, and analysed through their decay products.

The leading-order cross-section for off-shell W pair production (see figure 2.3) can be described by a two-fold convolution of a hard-scattering off-shell cross-section with Breit-Wigner density functions [16]:

$$\sigma(s) = \int_0^s ds_1\ \rho(s_1) \int_0^{(\sqrt{s}\perp\sqrt{s_1})^2} ds_2\ \rho(s_2)\ \sigma^0(s; s_1, s_2), \tag{2.8}$$

where

$$\rho(s) = \frac{1}{\pi}\frac{\Gamma_W}{M_W}\ \frac{s}{(s - M_W^2)^2 + s^2\Gamma_W^2/M_W^2} \tag{2.9}$$

is the relativistic Breit-Wigner spectral function associated to the $W^\pm$ propagators.

The $\sigma^0(s; s_1, s_2)$ is the cross-section of the W pair with invariant masses s_1 and s_2 at the leading-order. It contains terms corresponding to the `CC03` W pair production diagrams and their interferences. Explicit expressions for the various contributions can be found in ref. [16]. The on-shell cross-section is simply $\sigma^0_{\mathrm{on}\perp\mathrm{shell}}(s) = \sigma^0(s; M_W^2, M_W^2)$.

From eq. (2.8) and (2.9), one can conclude that the influence of the W mass to the cross-section is exclusively through the off-shell W propagators (not taking into account radiative corrections yet). All other parts are independent of M_W and Γ_W.

In the W propagator of eq. (2.9) an s-dependent W width (*running-width*) is used, similarly as for the Z^0 boson at LEP1:

$$\Gamma_W(s) = \frac{s}{M_W^2}\,\Gamma_W, \tag{2.10}$$

where $\Gamma_{\rm W} \equiv \Gamma_{\rm W}(M^2_{\rm W})$. Therefore, the resonance associated to the W boson is a definition of the W mass, similar to the Z^0 boson definition at LEP1.

From the theoretical point of view another possible approach is the use of a constant W width in the propagator:

$$\overline{\rho}(s) = \frac{1}{\pi} \frac{\overline{M}_{\rm W}\overline{\Gamma}_{\rm W}}{\left(s - \overline{M}^2_{\rm W}\right)^2 + \overline{M}^2_{\rm W}\overline{\Gamma}^2_{\rm W}}. \tag{2.11}$$

This approach introduces a different W mass definition. For a discussion see ref. [17]. Numerically the values of the mass and the width of the W from both definitions are related by [18]:

$$\overline{M}_{\rm W} = M_{\rm W} - \frac{1}{2}\frac{\Gamma^2_{\rm W}}{M_{\rm W}} \simeq M_{\rm W} - 27\,{\rm MeV}/c^2, \tag{2.12}$$

$$\overline{\Gamma}_{\rm W} = \Gamma_{\rm W} - \frac{1}{2}\frac{\Gamma^3_{\rm W}}{M^2_{\rm W}} \simeq \Gamma_{\rm W} - 0.7\,{\rm MeV}. \tag{2.13}$$

These relations may be derived from the following relation:

$$(s - \overline{M}^2_{\rm W} + i\overline{M}_{\rm W}\overline{\Gamma}_{\rm W}) = \frac{s - M^2_{\rm W} + i\,s\Gamma_{\rm W}/M_{\rm W}}{1 + i\,\Gamma_{\rm W}/M_{\rm W}}. \tag{2.14}$$

In the present analysis, the running-width in the propagator is adopted as the definition of the W mass.

2.3.4 Gauge invariance

When going from on-shell W pair production to the off-shell case, two sources of gauge non-invariance arise.

First of all, the use of incomplete sets of contributions. Only the `CC03` diagrams have been taken into account instead of all four-fermion diagrams, which would give a gauge independent result for a given final state. For example, for a final state with four different fermions and no electrons or positrons the gauge invariance is fulfilled when adding the singly-resonant diagrams (bremsstrahlung diagrams of a W from Bhabha-like scattering, described in section 2.2) to the doubly-resonant ones (`CC03` diagrams).

Secondly, more fundamental sources of gauge non-invariance are the poles at $s = M^2_{\rm W}$ that appear in the resonant graphs. They should be cured by introducing

a finite width while preserving unitarity through a proper energy dependence. In field theory, such a width arises naturally from the imaginary parts of higher-order diagrams describing the boson self-energies, resummed to all orders. However, in the past, (for the Z^0 resonance) only a subset of all possible diagrams was considered when summing the self-energy graphs, leaving a residual gauge dependence. Many schemes are developed to solve this problem:

- *fixed-width* scheme:

$$\frac{1}{s - M_W^2} \longrightarrow \frac{1}{s - M_W^2 + i\, M_W \Gamma_W}. \tag{2.15}$$

  This gives an unphysical width for $s < 0$, but retains U(1) gauge invariance in the `CC20` process [23]. This scheme has no physical motivation since, in perturbation theory, the propagator for space-like momenta do not develop an imaginary part. Consequently, unitarity is violated.

- *running-width* scheme: To avoid unitarity violation

$$\frac{1}{s - M_W^2} \longrightarrow \frac{1}{s - M_W^2 + i\, M_W \Gamma_W(s)}, \tag{2.16}$$

  where $\Gamma_W(s)$ is given by eq. (2.10). Still it does not solve the gauge dependence. This scheme leads to completely unreliable results when collinear singularities are present.

- *fermion-loop* scheme [19]:
  It selects an appropriate set of higher-order contributions (fermionic one-loop corrections) to restore gauge invariance. Collinear limits are properly behaved. It is well justified in standard perturbation theory. However, since the computation is very time consuming, it is not used in practice.

- Others as *fudge-factor* scheme [20], *pole* scheme [21] or *pinch-technique* [22].

A study of the cross-section for the process $e^+e^\perp \to e^\perp \bar{\nu}_e u\bar{d}$ (highly sensitive to U(1) electromagnetic gauge violation) using different schemes was done in ref. [23]. In table 2.2 the cross-section corresponding to the t-channel photon-exchange diagrams, responsible for the amplification of the gauge-breaking terms in the collinear limit, is shown using different schemes. The results are given for two values of the

minimum electron scattering angle ($\theta_{\min}$), displaying the effect of cutting away the collinear limit when $\theta_{\min} = 10^\circ$ is used. A naive introduction of the running-width scheme—with no correction—yields completely unreliable results for $\theta_{\min} = 0^\circ$, while the fixed-width scheme gives numerical results close to the ones obtained with the fermion-loop scheme, even though the gauge dependence is not solved.

In the Monte Carlo generation of this work, the fixed-width scheme is used.

Scheme	Cross-section (pb)	
	$\theta_{\min} = 0^\circ$	$\theta_{\min} = 10^\circ$
Fixed-width	0.8887(8)	.01660(3)
Running-width, no correction	60738(176)	.01713(3)
Fudge factor, with running-width	.08892(8)	.01671(3)
Pole scheme, with running-width	.08921(8)	.01666(3)
Fermion-loop scheme	.08896(8)	.01661(3)

Table 2.2: Cross-section in different schemes for the t-channel photon-exchange diagrams of $e^+e^- \to e^-\bar{\nu}_e u\bar{d}$.

2.4 Radiative corrections

In order to determine the W mass at LEP with a precision of $30 - 40\,\mathrm{MeV}/c^2$, the theoretical accuracy of the Standard Model prediction for the W pair production at LEP2 should be of half a percent [24] [4]. Therefore, it is necessary to fully understand and control higher-order QCD and electroweak corrections to the W production.

Ideally one would like to have the full radiative corrections to the final state of four fermions originating from the two decaying vector bosons. In practice such a calculation does not exist and appears to be unnecessary for the level of precision required at LEP2.

The complete set of $\mathcal{O}(\alpha)$ next-to-leading order radiative corrections to W^+W^- production is available for the on-shell case, comprising the virtual one-loop corrections and the real-photon bremsstrahlung [25] [26], but not for the off-shell case (see ref. [24] for a discussion). However, by using the on-shell calculation as a guide, some

[4] This accuracy is taken to be half the expected statistical error, taking into account that 10^4 W pair events are anticipated during the running of the LEP2 period.

of the largest effects can be predicted, as for example, the contribution coming from the Coulomb correction (the long-range electromagnetic interaction between almost stationary heavy particles (see section 2.4.1)), initial state radiation (emission of photons with the initial state e^+e^-), and further corrections. The coefficients of these corrections involve large factors like: $\sqrt{M_W/\Gamma_W}$, $\log(s/m_e^2)$, m_t^2/M_W^2. Once these corrections are taken into account the remaining ones are expected not to be larger than $\mathcal{O}(\alpha)$.

The division of the $\mathcal{O}(\alpha)$ radiative corrections into different parts differs from the one applied at LEP1. In the W pair production, it is not possible to divide them into electromagnetic and weak contributions as was done, for example, in the $e^+e^- \to Z^0 \to \mu^+\mu^-$ process, because the photon should couple to all charged particles in a line of the Feynman diagram to be separately gauge invariant, and this is not the case for the t-channel diagram in the W^+W^- production. Another natural division of the radiative corrections is: virtual, soft photonic and hard photonic contributions. Soft and hard photonic contributions are essential to establish the cancellations of infrared divergences coming from the virtual corrections (see section 2.4.2).

2.4.1 Coulomb singularity

This correction is associated to the long-range electromagnetic interaction [27] between the two charged W's in the final state: when oppositely charged particles have low relative velocity $v \ll 1$ (in units of c) Coulomb effects enhance the cross-section.

In the on-shell case, the Coulomb correction, which to leading-order in α/v, is $(1 + \alpha\pi/v)$, would diverge. Concerning the off-shell case, the W width acts as a natural cut-off for multiple soft photon interchange between both W's and, as a result, the divergence disappears—the perturbative expansion is in terms of $\alpha\pi\sqrt{M_W/\Gamma_W}$ [28] instead of $\alpha\pi/v$. However, the Coulomb effect is particularly significant (changing by approximately +6% the cross-section) near the W^+W^- production threshold (as the relative velocity v of the W bosons approaches zero), while negligible for centre-of-mass energies satisfying $\sqrt{s} - 2M_W \gg \Gamma_W$. Higher-order Coulomb corrections can be safely neglected above threshold ($\ll 1\%$) [29]. Concerning the W invariant mass shape, Coulomb corrections could lead to a downwards shift in the average reconstructed mass of $\sim 20\,\mathrm{MeV}/c^2$ in the threshold

region, while this shift may be an overestimation at higher LEP2 energies [30].

Similarly as in eq. (2.8) the $W^+W^\perp$ cross-section for off-shell bosons including the Coulomb correction at lowest order can be expressed as [28]:

$$\sigma(s) = \int_0^s ds_1\ \rho(s_1) \int_0^{(\sqrt{s}\perp\sqrt{s_1})^2} ds_2\ \rho(s_2)\ \sigma^0(s; s_1, s_2)\ [1 + \delta_C(s; s_1, s_2)]. \tag{2.17}$$

The term $\delta_C(s; s_1, s_2)$ represents the Coulomb correction, which, at $\mathcal{O}(\alpha)$ is:

$$\delta_C(s; s_1, s_2) = \frac{\alpha}{v}\left[\pi - 2\arctan\left(\frac{|\kappa|^2 - p^2}{2p\,\Re(\kappa)}\right)\right], \tag{2.18}$$

where p is the centre-of-mass momentum of a virtual W boson and v is the average velocity of the W bosons in their centre-of-mass system, which can be expressed as:

$$v = \frac{4p}{\sqrt{s}} = 2\sqrt{1 - \frac{(2s\,(s_1 + s_2) - (s_1 - s_2)^2)}{s^2}} \tag{2.19}$$

$$\kappa = \sqrt{-M_{\mathrm{W}}(E + i\Gamma_{\mathrm{W}})}, \quad E = \frac{s - 4M_{\mathrm{W}}^2}{4M_{\mathrm{W}}}.$$

Figure 2.3 shows how the exchange of soft photons distorts the line-shape of the $W^\pm$.

2.4.2 Initial state radiation

Initial state radiation (ISR) is one of the largest electroweak corrections to the $W^+W^\perp$ cross-section. It comes from the emission of photons from the incoming e^+ and $e^\perp$, and is the reason why, in the $W^+W^\perp$ production, the effectively available centre-of-mass energy is lower than without emission, thus reducing the cross-section (see figure 2.3).

The emission of virtual photons leads to divergent corrections (infrared divergences), compensated for when adding hard photon radiation. The collinear photon radiation off the electron or positron leads to logarithmic corrections $\sim \log(s/m_{\mathrm{e}}^2)$, which can be resummed and incorporated in the cross-section using a *flux function* or a *structure function* [31] approach. Both approaches assume that the ISR correction factorises.

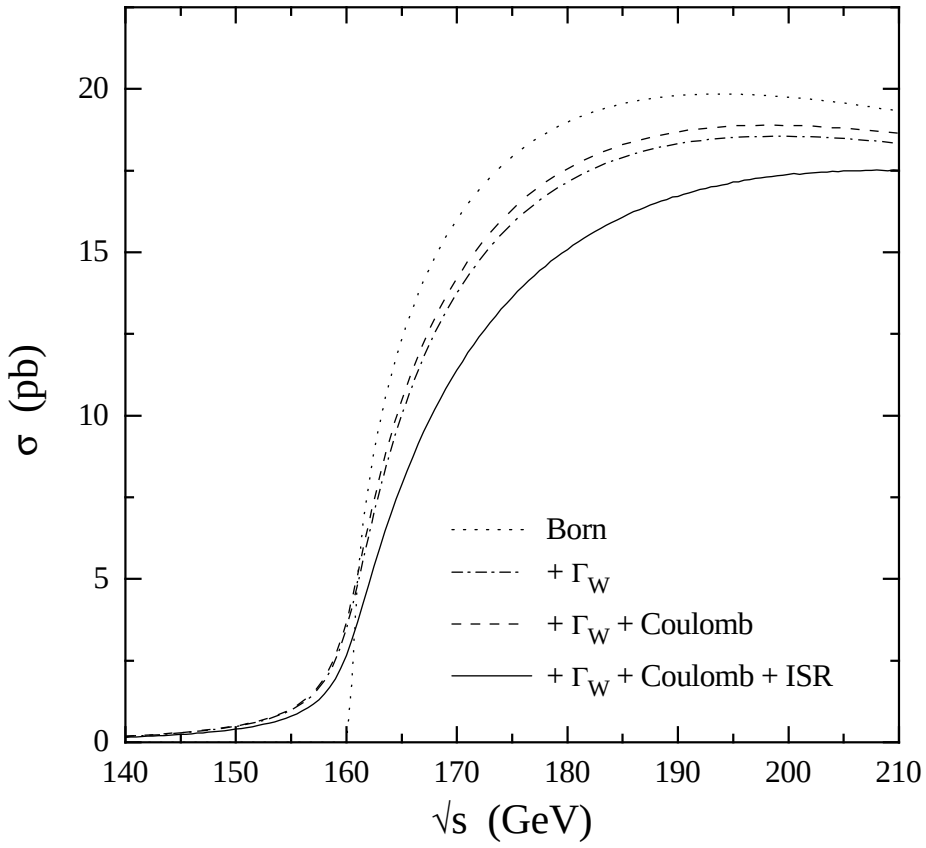

Figure 2.3: The cross-section for $e^+e^- \to W^+W^-$ in various approximations: (i) Born (on-shell) cross-section, (ii) Born (off-shell) cross-section, (iii) with first-order Coulomb corrections, and (iv) with initial state radiation.

The ISR corrected cross-section in the flux function (FF) approach is given by:

$$\sigma^{\mathrm{ISR}}(s) = \int_{s_{min}}^{s} \frac{ds'}{s} F(x,s)\, \sigma(s'), \tag{2.20}$$

where s' is the reduced centre-of-mass energy squared, $x = 1 - s'/s$, and σ follows eq. (2.17). The radiator function $F(x,s)$ in the flux approach is:

$$F(x,s) = t\, x^{t \perp 1}\, (1 + \mathcal{S}(s)) + \mathcal{H}(x,s), \tag{2.21}$$

with t containing all mass singularities terms $\log(s/m_e^2)$:

$$t = \frac{2\alpha}{\pi} \left[\log\left(\frac{s}{m_e^2}\right) - 1 \right]. \tag{2.22}$$

The $\mathcal{S}(s)$ term comes from soft and virtual photon emission and the $\mathcal{H}(x,s)$ term comes from hard photon emission [32].

Alternatively, the structure function (SF) approach may be used [33]:

$$\sigma^{\mathrm{QED}}(s) = \int_{x_1^{min}}^{1} dx_1 \int_{s_2^{min}}^{1} dx_2\, \mathcal{D}(x_1,s)\, \mathcal{D}(x_2,s)\, \sigma(x_1 x_2 s), \tag{2.23}$$

where:

$$\mathcal{D}(x,s) = \frac{t}{2}\,(1-x)^{t/2\perp 1}\,(1+\overline{\mathcal{S}}) + \overline{\mathcal{H}}(x,s) \tag{2.24}$$

and

$$\begin{aligned} x_1^{min} &= \frac{\left(\sqrt{s_1}+\sqrt{s_2}\right)^2}{s} \\ x_2^{min} &= \frac{\left(\sqrt{s_1}+\sqrt{s_2}\right)^2}{x_1 s}. \end{aligned} \tag{2.25}$$

2.5 The role of M_{W} in precision tests of the Standard Model

A precise measurement of the W mass, being sensitive to m_{t} and M_{H}, could lead to a better constraint of the Higgs mass—for a given top mass value—serving as a stringent test of the Standard Model [5].

[5] The parameters sufficient to parametrise the electroweak interactions in the Standard Model are conventionally chosen to be $\{\alpha, G_\mu, M_{\mathrm{Z}}\}$ (M_{Z} is the Z^0 boson mass) since these are accurately measured (M_{W}, in this case, is a prediction of the model). However, for the determination of the $\mathrm{W^+W^-}$ cross-section, a variation of the parameter M_{W} has to be accompanied by an adjustment of the charged and neutral couplings—a complicated procedure beyond leading-order. Consequently, this choice does not appear to be well suited.

A more appropriate choice is the set $\{M_{\mathrm{W}},\, G_\mu,\, M_{\mathrm{Z}}\}$ (the so-called G_μ scheme) [34], since in this case, M_{W} is one of the parameters of the model. With the tree-level relation:

$$g^2 = \frac{e^2}{\sin^2\theta_{\mathrm{W}}} = 4\sqrt{2} G_\mu M_{\mathrm{W}}^2, \tag{2.26}$$

(g is the coupling of an $\mathrm{SU(2)_L}$ symmetry) the dominant t-channel neutrino exchange amplitude, and hence the corresponding contribution to the cross-section depends only on the parameters M_{W} and G_μ. In this G_μ scheme there are no large next-to-leading order contributions to the cross-section depending on m_{t}, either quadratically or logarithmically [34]. It seems to be the most model independent approach when defining the parameters for computing the $\mathrm{W^+W^-}$ cross-section.

An example of the possible impact of a given W mass precision on the Higgs mass is shown in table 2.3, which lists the errors in M_{H} that would result from measurements of M_{W} with errors of 25 and 50 MeV/c^2 assuming that the top mass is measured to be $m_{\mathrm{t}} = 180 \pm 5\,\mathrm{GeV}/c^2$ [35] (the present measurement is $m_{\mathrm{t}} = 173.8 \pm 5.0\,\mathrm{GeV}/c^2$ [36]). With such M_{W} errors a significant impact on the prediction of M_{H} within the Standard Model is expected. It could also constrain possible extensions of the Standard Model such as supersymmetry.

Nominal $M_{\mathrm{H}}(\mathrm{GeV}/c^2)$	ΔM_{W}	
	25 MeV/c^2	50 MeV/c^2
100	(+86, −54)	(+140, −72)
300	(+196, −126)	(+323, −168)

Table 2.3: Estimated error in M_{H} for different assumed uncertainty values of the W mass (ΔM_{W}).

The W gauge boson mass was measured indirectly at LEP1 using the Fermi constant (G_μ), accurately known from the muon decay:

$$G_\mu = \frac{\pi\ \alpha(M_{\mathrm{Z}}^2)}{\sqrt{2}\ M_{\mathrm{W}}^2\ \sin^2\theta_{\mathrm{W}}}\ \frac{1}{1-\Delta r}, \tag{2.27}$$

where:

$$\sin^2\theta_{\mathrm{W}} = 1 - \frac{M_{\mathrm{W}}^2}{M_{\mathrm{Z}}^2}, \tag{2.28}$$

and Δr is a radiative correction which depends on m_{t}^2 and $\log(M_{\mathrm{H}}/\mathrm{GeV})$ when one-loop corrections are included. The combination of the results obtained from LEP1 and SLD gives [37]:

$$M_{\mathrm{W}}^{\mathrm{LEP1/SLD}} = 80.332 \pm 0.037\,\mathrm{GeV}/c^2, \tag{2.29}$$

in agreement with the result obtained so far by the hadron collider experiments (CDF, D0 and UA2) using the direct determination method through the process $p\bar{p} \to \mathrm{W}^{\pm}X \to \ell^{\pm}\nu X$ [38]:

$$M_{\mathrm{W}}^{p\bar{p}} = 80.41 \pm 0.09\,\mathrm{GeV}/c^2. \tag{2.30}$$

In the LEP2 period, a better accuracy of the W mass is expected to be achieved. The aim is a precision of $30 - 40\,\mathrm{MeV}/c^2$ with an expected integrated luminosity of $500\,\mathrm{pb}^{\perp 1}$. With the first data taken at LEP at the W production threshold (161.3 GeV) the combination of the four LEP experiments results of the cross-section measurement leads to a W mass value of [39]:

$$M_{\mathrm{W}} = 80.40 \pm 0.22\,\mathrm{GeV}/c^2, \tag{2.31}$$

in good agreement with $M_{\mathrm{W}}^{p\bar{p}}$. The limit on the Higgs mass will improve whenever the results from M_{W} direct measurements at higher LEP energies are taken into account. It is important to compare also the W mass value obtained from direct to the indirect measurements to see if there is some contradiction, thus indicating a breakdown of the Standard Model.

2.6 W mass at LEP

The determination of the W mass at LEP2 is possible using different methods:

(i) **Threshold cross-section measurement** of the process $\mathrm{e}^+\mathrm{e}^\perp \rightarrow \mathrm{W}^+\mathrm{W}^\perp$. It makes use of the rapid increase of the $\mathrm{W}^+\mathrm{W}^\perp$ production cross-section at $\sqrt{s} \sim 2M_{\mathrm{W}}$ to measure the W mass. It relies on the comparison of an absolute cross-section measurement with a theoretical calculation which has M_{W} as a free parameter. The smallness of the cross-section near the threshold is compensated by the enhanced sensitivity to M_{W} in this region. Combining the M_{W} results from the analysis of 161.3 GeV data collected by the four experiments at LEP, the achieved accuracy of M_{W} is of $\sim 220\,\mathrm{MeV}/c^2$ (eq. (2.31)).

(ii) **Direct reconstruction** method. The W mass can be measured reconstructing the Breit-Wigner resonant shape from the $\mathrm{W}^\pm$ final states, using kinematic fitting techniques to improve the mass resolution. This method makes use of the large $\mathrm{W}^+\mathrm{W}^\perp$ statistics at the higher LEP energies, $\sqrt{s} \geq 175\,\mathrm{GeV}$. Here, the most important issue is the accurate determination of the invariant mass distribution of the $\mathrm{W}^\pm$ decay products. This is the method used in this thesis, and it is explained in more detail in the following chapters.

(iii) **Determination of M_{W} from the lepton end-point energy**. The end-points of the lepton spectrum in semileptonic decays depend quite sensitively on the W mass. For on-shell W bosons at leading-order:

$$E_{\perp} \leq E_l \leq E_{+}, \qquad E_{\pm} = \frac{\sqrt{s}}{4}\left(1 \pm \sqrt{1 - 4M_{\mathrm{W}}^2/s}\right).$$

In this case the statistical error on M_{W} is determined by the statistical error on the measurement of the lepton end-point energy:

$$\Delta M_{\mathrm{W}} = \frac{\sqrt{s - 4M_{\mathrm{W}}^2}}{M_{\mathrm{W}}} \Delta E_{\pm}. \tag{2.32}$$

Unfortunately, the end-point is so smeared by finite width effects and initial state radiation, and so limited in statistics—the statistical power of this method has a naive estimate in eq. (2.32)—that it does not appear to be a competitive way to determine the W mass. It has not been used so far by any of the four LEP experiments.

2.7 Interconnection effects

The decay products of the produced W pair may interact (QCD interconnection phenomena and QED interactions) and the final state may no longer be considered as a superposition of two separate W decays.

In general, QCD and QED interconnection phenomena affect differently each method of determining the W mass, the direct reconstruction method being more affected than the cross-section method, as the invariant masses of the W final states are determined in the first method. Only the contribution from the Coulomb interaction between slowly moving W bosons, already described in section 2.4.1, has a bigger effect in the threshold region, hence in the cross-section method. A good theoretical knowledge of these effects is needed in order to have a precise measurement of the W boson mass.

Specific to the fully hadronic decay channel are QCD interconnection phenomena (the so-called colour reconnection effects) and Bose-Einstein correlations between identical bosons (in practice pions). Both are potential sources of shifts in the measurement of the W mass. Although there exist a lot of models for colour reconnection, only those tested in this thesis are briefly described below.

2.7.1 Colour reconnection

A first attempt to describe the process: $e^+e^- \rightarrow W^+W^- \rightarrow q_1\bar{q}_2q_3\bar{q}_4$ would be to assume that the $q_1\bar{q}_2$ pair from W^+ forms one colour-singlet and the $q_3\bar{q}_4$ pair from W^- forms a second one, and then the two systems hadronise independently of each other. The W particles, however, exist only for a very short time, as a result of the large W width ($\tau_W \sim 1/\Gamma_W \approx 0.5\,\mathrm{GeV}^{-1}$). Therefore, the space-time separation between the production points of the two $q\bar{q}$ pairs is very small ($< 0.1\,\mathrm{fm}$) compared to the typical distance scale of hadronisation ($\sim 1\,\mathrm{fm}$). In one extreme case the production of the four quarks at the same point could be assumed. Thus, in addition to the original colour dipoles $q_1\bar{q}_2$ and $q_3\bar{q}_4$, it could be possible to form another set of dipoles, namely $q_1\bar{q}_4$ and $q_2\bar{q}_3$. These QCD interconnection phenomena between the W^+W^- decay products—most commonly called colour reconnection effects—could influence the reconstructed W mass in the hadronic channel.

The picture is complicated by the possibility of gluon emission. It is useful to discuss the wavelength of gluons at different stages of the process. A hard gluon (energy $\gg \Gamma_W$) in the perturbative region (the parton-shower [6]) has a wavelength much smaller than the decay vertex separation and can therefore resolve the two decay vertices. This is described by perturbative QCD and different reconnection probabilities are expected to be suppressed by factors $1/(N_C^2 - 1)$ (N_C being the number of colours) yielding small effects [41]. On the other hand, in the hadronisation region, gluon wavelengths are much larger and might feel the joint action of all four quarks colour charges. As a result, it is in the non-perturbative hadronisation region where interference effects might be important.

Studies on these effects cannot be described by perturbative methods, thus fully relying on specific model-dependent implementations. All the commonly used models for non-perturbative colour reconnection are based on a space-time picture in which reconnection is a local phenomenon. Objects are formed at the hadronisation stage via a local interaction which may combine products of the two W decays in regions where they overlap. Two classes of models may be distinguished, according to

[6] The parton-shower is the approach taken in JETSET [40] to have high multiplicity already in the perturbative phase. It is based on an iterative use of the following processes: $q \rightarrow qg$, $g \rightarrow gg$, $g \rightarrow q\bar{q}$.

the types of combinations that are permitted. In *singlet* models only colour-singlet objects can be formed whereas in *non-singlet* models there is no such constraint.

All the reconnection models based on string hadronisation proposed by Khoze and Sjöstrand [41] are singlet models, since each string is a colour-singlet (reconnections within a W system are not considered). Within this framework three different models are investigated:

- model I: After the parton-shower, the string-systems are described as spheres and may reconnect with a probability proportional to the volume of overlap of the two independent string-systems. The model contains a free strength parameter that can be adjusted to give any desired reconnection probability.
- model II: Strings are considered to have negligible thickness (thin vortex lines) and reconnection may happen when they intersect each other.
- model II': Similar to model II but reconnection is suppressed if there is no reduction of the total string length.

The reason for these names is the analogy to the two types of superconducting vortices (I and II) which could correspond to colour strings. These three models are implemented in the `EXCALIBUR` [42] Monte Carlo and used for the systematic studies in the W mass measurement.

The main alternative to the string hadronisation model is the cluster model, in which quarks and gluons from the parton-showers combine locally into clusters. These clusters are much less extended and less massive objects than strings, typically light enough to decay more or less isotropically into a small number of hadrons each. The most widely used cluster models have also been colour-singlet models, in which only singlet combinations of partons (quarks and antiquarks) are allowed to form clusters. This model is implemented in `HERWIG` [43] which incorporates a free parameter to set the probability for colour reconnection, called PRECO.

Another model based on colour-singlet is the one which reconnects colour dipoles within the framework of the Dipole Cascade Model [44] with a probability $1/N_C^2$ [7] only if the total string length becomes reduced. In the DCM, colour indices (chosen

[7] It corresponds to the probability that the quark from one W decay could form a colour-singlet with the antiquark from the other.

randomly with some restrictions) are assigned to each dipole, and after each gluon radiation, dipoles with identical indices are allowed to reconnect. Reconnections within each W system and between W's are allowed. At the end, the two systems hadronise. This model is implemented in the `ARIADNE` [45] Monte Carlo.

The only general hadronisation model available at present which includes non-singlet component, allowing reconnections even when the colour is not neutralised, is the so-called 'colour-full' scenario (implemented in the VNI Monte Carlo [46]), of Ellis and Geiger [47], which is based on a transport-theoretical treatment (see the details of the QCD transport-theory in ref. [48] [8]) of parton-showering and cluster formation. It uses an effective Lagrangian containing both partonic and hadronic degrees of freedom to generate the parton shower. The cluster formation begins whenever partons start to move too far away from their neighbours, preventing them from becoming widely separated (a requirement for colour confinement). Big effects on the W mass are predicted.

2.7.2 Bose-Einstein correlations

In hadronic W^+W^- decays, large number of pions are produced. As a consequence of Bose statistics, an enhancement of the production in the hadronisation process of identical particles (typically charged pions of the same sign) at small momentum separation, relative to the hypothetical state of uncorrelated production, is expected (Bose-Einstein (BE) effect [49])—almost four times as many identical pion pairs as in a single W decay. Therefore, the softest particles from each W would be "dragged" closer to each other and this would reduce the momentum of the W's. Then, an increase of the measured W mass would be expected. On the other hand, there is a prejudice that this cross-talk effect should be small, because it affects the overlapping regions of the jets, i.e. low-energy hadrons, whereas fast hadrons, which are critical for the di-jet masses, should not be affected.

The problem with estimating such effects is that they are purely quantum-mechanical in nature, whereas the Monte Carlo programmes used to generate simulated events are based on classical models, dealing with probabilities and not with

[8] The QCD transport-theory describes the dynamical interplay of quantum and statistical-kinetic properties of non-equilibrium multi-parton systems produced in high-energy QCD processes.

amplitudes. In response to this problem, several methods of introducing Bose-Einstein correlations onto existing event generators have been proposed.

The most developed model is implemented in JETSET [40] [50]. In this approach, the momenta of identical final state particles are redistributed (shifted) to reproduce the expected two-boson momentum correlations [9]. The main problem is that the momentum shifts spoil overall energy-momentum conservation and so, some momenta of non-identical particles have to be modified in order to compensate for this (the so-called global rescaling procedure) thus introducing spurious long-range correlations. The advantage is that it is a unit-weight event generator since it does not involve reweighting of events. It was found that the implications of this model for the W mass measurement could be quite severe [50], which would make the hadronic channel essentially useless for the W mass determination.

Another method for imposing Bose-Einstein correlations is to use reweighting of events. Connected to the method explained before, recent studies—done by the same authors—on the 'local event weighting strategy' [51] with improved algorithms of handling locally energy and momentum conservation indicate lower shifts due to Bose-Einstein correlations (models called BE_3 and BE_{23}). A global BE weight (w_{BE}) is assigned to the simulated events according to the momentum distribution of the final state boson: pairs of equal-sign particles closer in momentum space should have slightly bigger weight than the distant ones. The method arises very naturally in a quantum-mechanical approach, where the weight, assigned to the event as a whole, can be constructed as the ratio of the square matrix elements of the

[9] The standard quantity to measure such correlations is the correlation function ($c_2(Q)$) which, assuming a spherical space-time distribution of the source emitting identical bosons with known momenta (p_1 and p_2), takes the phenomenological form:

$$c_2(Q) = 1 + \lambda\rho(Q), \tag{2.33}$$

where Q is the four-momentum difference, $Q^2 = -(p_1 - p_2)^2$, and ρ is the absolute square of the Fourier transform of the particle emitting source density, with the normalization condition $\rho(0) = 1$. The *incoherence* or *strength* or *chaoticity* parameter (λ) takes into account the fact that, for various reasons, the strength of the correlations can be reduced. For a Gaussian model for the source density:

$$\rho(Q) = \exp(-R^2Q^2), \tag{2.34}$$

where R is the *source radius*.

production process with and without BE respectively. Such an approach assumes that a model exists for particle production in the absence of Bose statistics, and that a lot of our ignorance divides out in the ratio so that an absolute knowledge of non-perturbative QCD is not needed. The problem is that, even if the correct calculation of the weight function is known, this would be too laborious, involving a sum over all permutations of particles. This has led to the investigation of 'partial symmetrization' procedures that aim to include the most important permutations for each event. Two different procedures are discussed in more detail below.

A possible way is to organize the identical particles into clusters such that only the permutations within clusters are considered in computing the Bose-Einstein weights [10]. This approach is applied in ref. [52], with the conclusion that negligible influence on the reconstruction of the W mass due to Bose-Einstein correlations is found. Another possibility is that applied in ref. [53], where only permutations up to some maximum number of identical particles are taken into account [11]. Negligible (below $30\,\mathrm{MeV}/c^2$) W mass shifts are also found.

Other methods found in the context of nuclear physics, as for example in ref. [54], or the one developed from the Lund string model of hadronisation [55] are not studied in this thesis, and not described here.

[10] The weight of a cluster depends on the cluster multiplicity and two model parameters p and R, controlling the strength of Bose-Einstein correlations.

[11] The only parameter of this model is a Gaussian half-width (σ) of the two-particle weight factors, controlling the source radius.

Chapter 3

Description of the experiment

The ALEPH detector [56] is one of the four large detectors installed in the LEP collider. The other three experiments are DELPHI [57], L3 [58] and OPAL [59]. ALEPH was designed to study in detail the parameters of the Standard Model, to test QCD at large Q^2 and to search for new physics (such as the Higgs boson or supersymmetric particles) in the $e^+e^\perp$ interactions taking place at LEP. The detector was conceived to be as hermetic as possible, covering the maximum allowed solid angle with good track resolution and fine calorimetric granularity.

The first section of this chapter is devoted to giving a brief description of the LEP collider with stress on the determination of the beam energy, of great importance for this analysis. Then, the ALEPH detector, with some emphasis on the performances relevant to the analysis, is described. At the end, a few words are devoted to the event reconstruction, including the tracking and energy-flow algorithms used in ALEPH, and to the simulation processes.

3.1 The LEP collider

The LEP machine (Large Electron Positron collider) [60] is an $e^+e^\perp$ storage ring of 26.7 km of circumference sited at the European Centre for Particle Physics (CERN) in Geneva, Switzerland, and in operation since 1989. It is located in a tunnel nearly horizontal (with a tilt of 1.42%, due to geological reasons) at a depth between 80 and 137 m, under the French and Swiss territories and it is the largest collider of this type in the world (see figure 3.1).

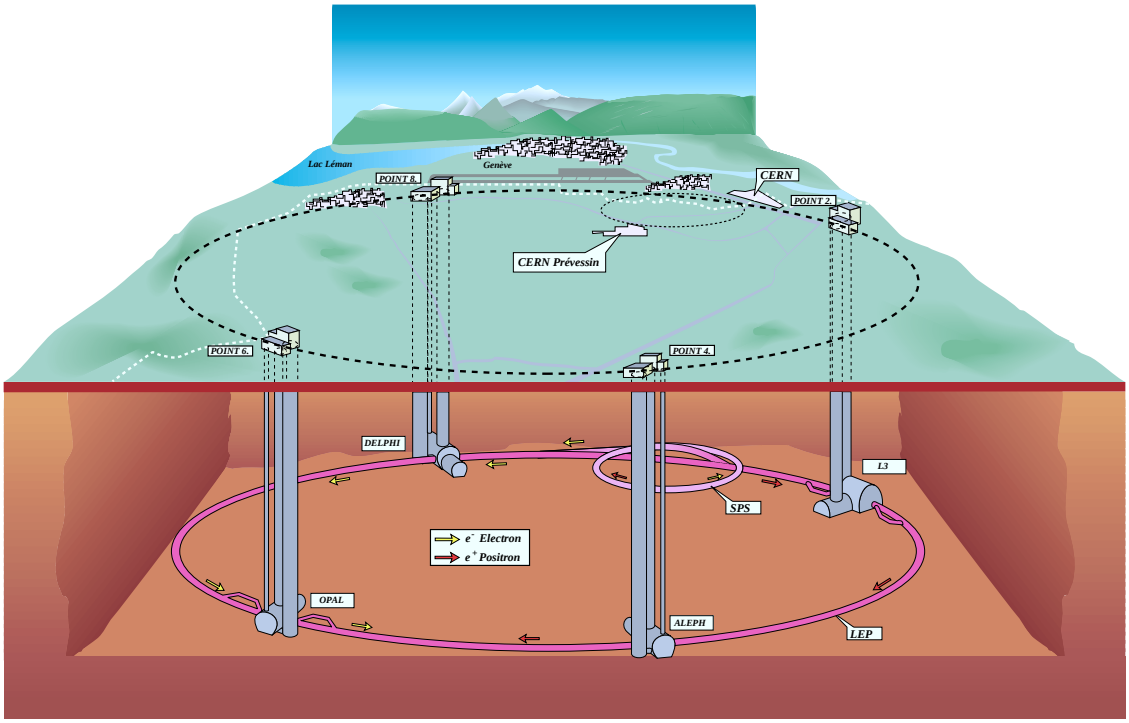

Figure 3.1: View of the LEP ring and the four interaction points.

The beams that circulate around the ring inside the beam pipe, which consists of eight arcs alternating with eight straight sections, are formed by bunches of electrons and positrons. They are accelerated in opposite directions and cross in eight or sixteen points in the case where the number of bunches is four or eight, respectively. But it is only in the four points where the detectors ALEPH, DELPHI, L3 and OPAL are installed, where they collide every 22 μs (or 11 μs). The other collision points are avoided by means of a system of electrostatic separators.

The LEP injection chain is shown in figure 3.2. It starts with the LINear ACcelerator (LINAC) which accelerates electrons and positrons in two stages. The electrons are first accelerated up to 200 MeV. Part of these electrons are used to produce positrons by collision with a fixed target of tungsten and the rest, together with the positrons, are accelerated up to 600 MeV. These two first linear accelerations constitute the LEP Linear Injector (LIL). Then, the particles are inserted into a small (0.12 km of circumference) storage ring, the Electron Positron Accumulator

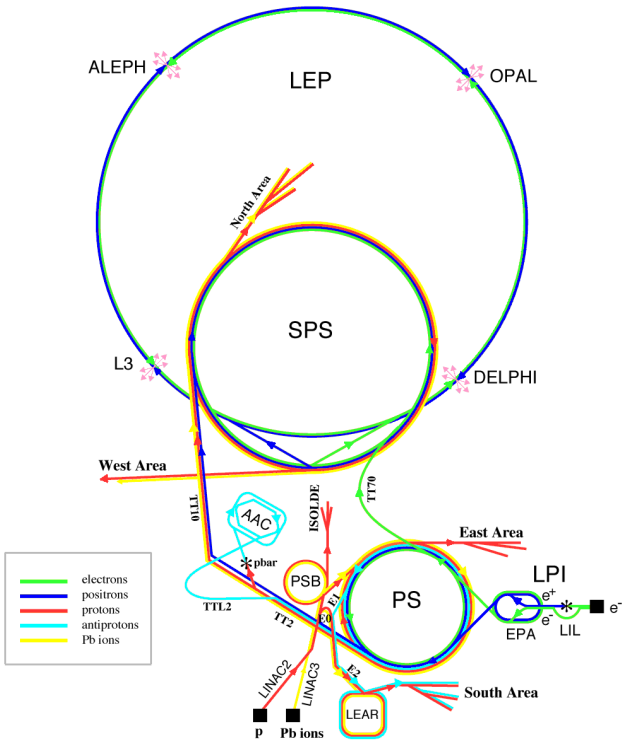

Figure 3.2: Scheme of the LEP injectors and accelerators.

(EPA), where they are separated into bunches and accumulated until the beam intensities achieve $\sim 10^{10}$ particles. From there, the bunches are inserted in the Positron Synchrotron (PS) storage ring where they achieve an energy of 3.5 GeV. Afterwards, the particles are injected into the Super Proton Synchrotron (SPS) storage ring reaching an energy of 20 GeV [1], and finally, injected into the LEP main ring and accelerated up to the energy of collision.

In circular $e^+e^\perp$ colliders the maximum beam energy is limited by the energy loss of the beam particles due to the synchrotron radiation, which is proportional to E^4/R, with E being the particle energy and R the radius of curvature. This loss of energy is compensated for by means of a continuous energy supply from cavities of radio-frequency (RF), providing an extra-acceleration.

The accelerator programme comprises two phases. In the first phase (the so-called LEP1 phase), finished in 1995, the LEP machine was operated at a centre-

[1] This energy was increased up to 22 GeV during 1997.

of-mass energy of $\sim 91\,\mathrm{GeV}$, the peak of Z^0 production, with luminosities (number of events per unit of time per unit of cross-section) at the level of $10^{31}\,\mathrm{cm}^{\perp 2}\mathrm{s}^{\perp 1}$. Around four million visible Z^0 decays were produced per experiment. In 1998, with four bunches, luminosities of about $10^{32}\,\mathrm{cm}^{\perp 2}\mathrm{s}^{\perp 1}$ were achieved. The LEP2 programme started in summer 1996, when $e^+e^\perp$ collisions at a centre-of-mass energy of $\sqrt{s} = 161\,\mathrm{GeV}$ (above the W pair production threshold) and, afterwards, at 172 GeV were produced for the first time. In order to achieve this energy and compensate for the increased synchrotron radiation, new niobium superconducting RF cavities had to be installed, partially replacing the old room temperature copper cavities. During 1997, the $e^+e^\perp$ collisions were produced at $\sqrt{s}$ =183 GeV and during 1998 an energy of $\sqrt{s} = 189\,\mathrm{GeV}$ has been achieved with the installation of more superconducting cavities. A total integrated luminosity per experiment of about $500\,\mathrm{pb}^{\perp 1}$ is expected to be collected during the whole LEP2 phase, which is expected to finish by the year 2000.

3.1.1 Determination of the LEP centre-of-mass energy

A precise knowledge of the LEP beam energy is of great importance in the measurement of the W boson mass: the beam energy sets the absolute energy scale for this measurement, leading to an uncertainty of: $\Delta M_\mathrm{W}/M_\mathrm{W} \approx \Delta E_{beam}/E_{beam}$. With the full LEP2 data sample, the expected statistical W mass uncertainty is $25\,\mathrm{MeV}/c^2$. To avoid a significant contribution to the total error, a target of 10 to $15\,\mathrm{MeV}/c^2$ uncertainty for a beam energy of about 90 GeV is set [61].

During the LEP1 period, the average beam energy was measured directly at the physics operating energy with high precision (typically 1 MeV), which allowed a very good determination of the Z^0 mass and width. The method used to determine the beam energy was the so-called resonant depolarization (RD) [62] method.

The RD method takes advantage of the fact that a non-negligible transverse beam polarization can be built up in a circular machine such as LEP, due to the interaction of the electrons with the magnetic field (Sokolov-Ternov effect [63]): the *spin tune*, or number of spin precessions in one turn around the ring (ν), determined by RD, is proportional to the beam energy (E_{beam}) averaged around the beam trajectory:

$$\nu = \frac{g_e - 2}{2} \frac{E_{beam}}{m_e c^2}, \tag{3.1}$$

where m_e is the electron mass, c the speed of light, and $(g_e - 2)/2$ the anomalous magnetic-moment of the electron. This relation is exact only for ideal storage rings and needs to be corrected for small imperfections as a depolarization takes place over many thousand turns of the beams. E_{beam} is proportional to the total integrated vertical magnetic field (B) around the beam trajectory (l):

$$E_{beam} = \frac{e}{2\pi c} \oint_{LEP} B \cdot \mathrm{d}l. \tag{3.2}$$

Unfortunately, at LEP2 this method cannot be applied, since at the energies achieved in this period, the beam transverse polarization cannot be maintained: depolarization effects increase sharply with the beam energy due to broadening resonances. The highest beam energy at which a sufficiently high level of transverse polarization was achieved in 1997 was 55 GeV [61].

Therefore, the measurement of the beam energy at LEP2 is obtained from depolarization measurements at lower energies (up to 55 GeV) and extrapolated to higher energies. The extrapolation to physics energy depends on a comparison of the measured RD energies with the magnetic fields, measured by 16 Nuclear Magnetic Resonance (NMR) probes installed in 1996 inside some selected LEP main bend dipoles [2] (see figure 3.3). The relation between NMR's records and the beam energy can be precisely calibrated against RD measurements. It is assumed to be linear (with zero intercept in the 1996 data measurement), and to be valid up to physics energies. The NMR's sample a small fraction of the field while flux-loops [3], installed in each LEP dipole magnet (see figure 3.3), provide a measurement of 97% of the total bending field. Flux-loop measures are used to cross-check the beam energy determined by the NMR probes.

[2] There is at least one probe in each octant, and in octants 1 and 5 there are strings of probes in several adjacent dipoles. These probes are read out continuously (typically every 30 seconds) during physics running and during RD measurements.

[3] Each flux-loop is made of thin wires embedded in grooves machined in the lower poles of the magnets [64]. Flux-loop experiments are performed only occasionally, without beam in the machine.

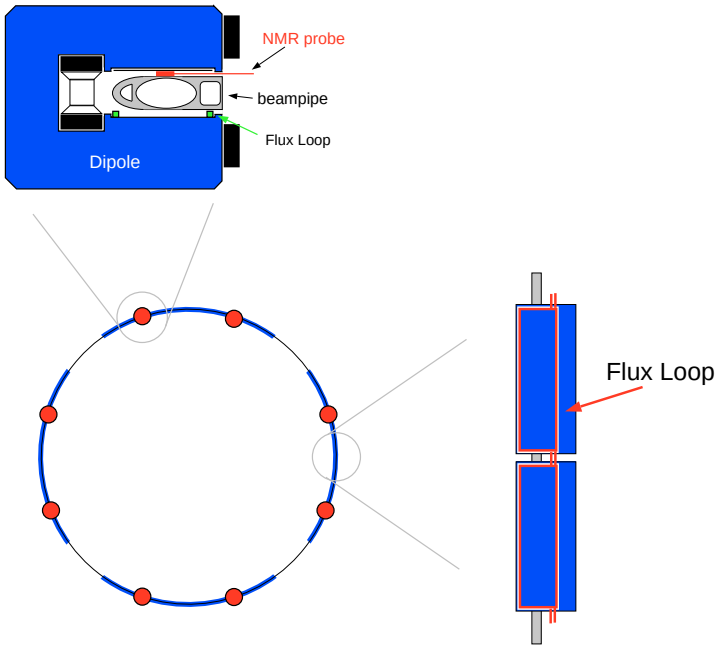

Figure 3.3: The NMR probes and flux-loop used for monitoring the LEP magnetic field.

The use of magnetic measurements becomes the largest source of uncertainty (20 MeV at physics energy), which is inferred from the agreement between the NMR fields and the total bending field measured by the flux-loop. Systematic errors on the NMR calibration are evaluated from the reproducibility of different experiments, and the variations from probe to probe.

Having fixed the overall normalisation, the energy is corrected for variation as a function of time, due to earth tides, temperature effects, leakage currents from neighbourhood Geneva-Paris TGV electric trains and so on. There are also corrections to relate the average energy to the collision energy at each interaction point, in particular due to the exact accelerating RF configuration. All of these effects have been rather well understood at LEP1 [62], and contribute a total additional uncertainty below 10 MeV [61] at LEP2.

The beam energy is determined with a precision of 25 MeV [61] for the data taken in 1997, about 10 times larger than the uncertainty at LEP1. The analysis of the 1996 data led to a beam energy uncertainty of 30 MeV [65].

3.2 The ALEPH detector

The ALEPH [66] (Apparatus for LEp PHysics) detector is located at the experimental point number four (next to Echenevex in France) in a cavern 143 m below the surface of the earth and 6 m below the LEP beam line (it is the deepest point where the beam passes through). ALEPH is a 12 m diameter by 12 m length cylinder weighting about 4000 tons and positioned around the beam pipe, which is a tube of 10 cm of radius that forms part of the accelerator, covering 95% of the solid angle around the interaction point (in the middle). In the ALEPH reference system (its origin is the theoretical beam crossing point), the z direction is along the beam line, positive in the direction followed by the electrons, thereby slightly different from the local horizontal direction due to the fact that the accelerator is slightly tilted. The positive x direction points to the centre of LEP, and is horizontal by definition. The positive y direction is orthogonal to z and x pointing upwards, and deviates 3.5875 mrad from the local vertical direction.

The detector consists of independent and modular subdetectors arranged in layers, each one specialized in a different task. The two main type of subdetectors are tracking devices, which allow to reconstruct the trajectories of charged particles and to classify them using the ionization left in the detectors, and calorimeters (electromagnetic and hadronic) which give a measurement of the energy of the particles, being also the only detectors capable to give position information for the neutral particles. Muons are identified using the muon chambers and/or the final planes of the hadronic calorimeter. Specialized detectors situated at low angle give a precise measurement of the luminosity. Some other subdetectors monitor the instantaneous luminosity and the background. Finally, the trigger and data acquisition systems are used to decide when to read the events and to record them, respectively. A brief description of these devices follows, mainly stressing their performances [67]. A detailed and complete description can be found in refs. [56] [66].

Main detectors

A particle leaving the central interaction point will encounter the following subdetectors (see figure 3.4):

- **The Mini Vertex DETector (VDET)** is a double sided silicon strip device with two layers of strips, one parallel (z) and one perpendicular ($r\phi$) to the beam, situated around the beam pipe. It provides a very accurate vertex tagging of tracks (with $|\cos\theta| < 0.95$) coming from the interaction point with a coordinate spatial resolution of $10\,\mu$m in $r\phi$ and $15\,\mu$m in z. It plays a very important role in the reconstruction of particles with very short lifetime, like the τ lepton or hadrons containing b or c quarks, through the accurate measurement of the impact parameter of their charged decay products.

- **The Inner Tracking Chamber (ITC)** is a cylindrical multiwire drift chamber. It can provide up to eight precise $r\phi$ coordinates per track, with an accuracy of $150\,\mu$m per coordinate. It contributes to the global ALEPH tracking and is also used for the triggering of charged particles coming from the interaction region.

- **The Time Projection Chamber (TPC)**, the main tracking detector of ALEPH, is a very large cylindrical imaging drift chamber: 4.7 m long with 31 cm and 180 cm inner and outer radius respectively. The three coordinates of the particle trajectories are measured by the TPC: the z-coordinate is obtained from the drift time and the known drift velocity, the ϕ coordinate is calculated interpolating the signals induced on cathode pads located precisely on the sectors (the end-plate where the charged particles are collected is divided into 18 wire chambers or sectors), and the r-coordinate is given by the radial position for the pads involved in the measurement. It provides up to 21 three-dimensional coordinate points for each charged track crossing the chamber. The single coordinate resolution is $173\,\mu$m in the azimuthal direction and $740\,\mu$m in the longitudinal direction. From the curvature of tracks, due to the presence of a magnetic field, the TPC gives a measurement of transverse particle momenta (p_T) with an accuracy of $\Delta p_T/p_T^2 = 0.6 \times 10^{\perp 3}\,(\mathrm{GeV/c})^{\perp 1}$ at 45 GeV, if used together with the ITC and the VDET. The chamber also contributes to charged particle identification through measurements of energy loss (dE/dx) derived from about 320 samples of the ionization for a track traversing the full radial range.

- **The Electromagnetic CALorimeter (ECAL)** is a sampling calorimeter consisting of alternating lead sheets and proportional wire chambers read out

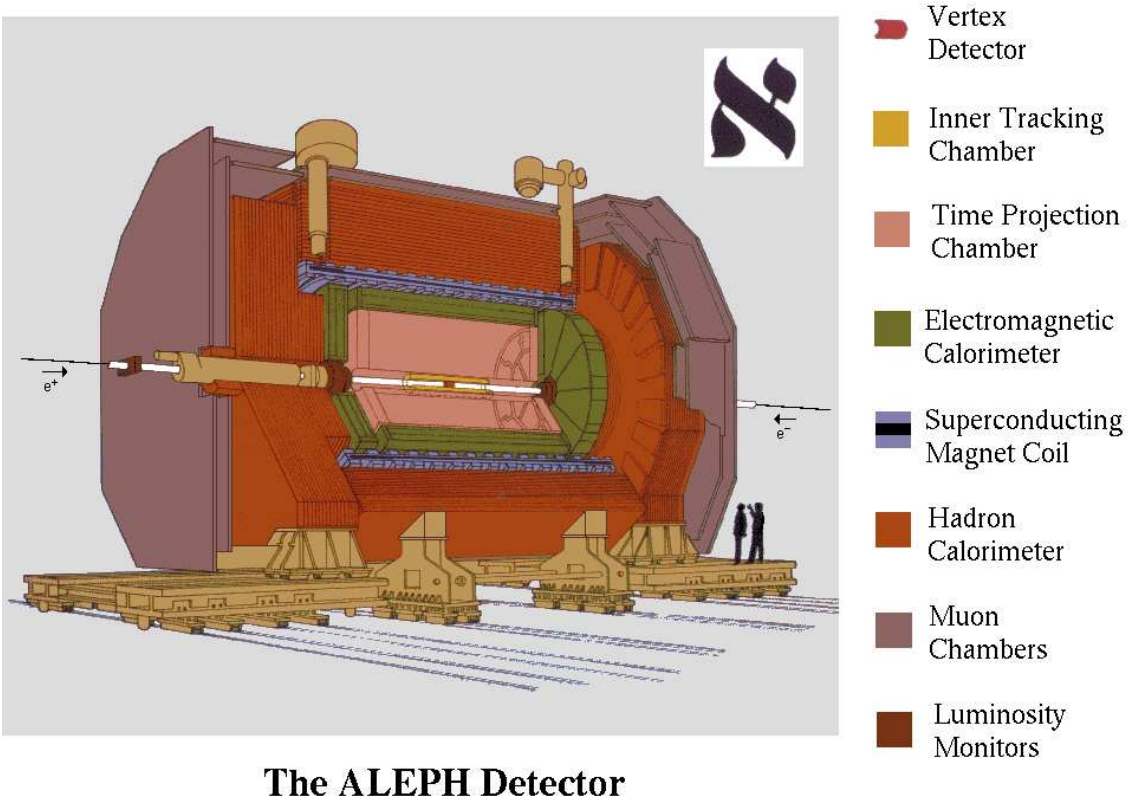

Figure 3.4: The ALEPH detector.

in projective towers and longitudinally segmented in three compartments (one barrel and two endcaps). A granularity of about $0.9^\circ \times 0.9^\circ$ regions of solid angle pointing to the interaction point is obtained. The ECAL measures the energy and position of electromagnetic showers. The high position (the inner radius is 1.85 m and the outer radius 2.25 m) and the achieved energy resolution, $\sigma(E)/E = 0.18/\sqrt{E/\mathrm{GeV}} + 0.009$, lead to good electron identification and allow to measure photon energy even in the vicinity of hadrons.

– **The Superconducting coil** is a liquid-Helium cooled superconducting solenoid creating, together with the iron yoke, a 1.5 T axial magnetic field in the central detector.

– **The Hadronic CALorimeter (HCAL)** is a sampling calorimeter longitudinally segmented as ECAL, made of layers of iron and streamer tubes, and globally rotated 1.875° with respect to ECAL in order not to superimpose

the crack regions (3.4% of the solid angle for HCAL). It measures energy and position for hadronic showers and, complemented with the muon chambers, acts as a muon detector. The energy resolution for a charged pion is $\sigma(E)/E = 0.85/\sqrt{E/\mathrm{GeV}}$. The readout is performed twice: using cathode pads forming projective towers and using digital readout of the streamer tubes for muon tracking and also for triggering. It also provides the main support of ALEPH, the large iron structure serving both as hadron absorber and as return yoke of the magnet.

- **The MUON chambers (MUON)**, outside HCAL, are two double layers of limited streamer tubes which measure position coordinates of muons, the only detectable particles reaching this subdetector. For a muon travelling through both layers of muon chambers the direction of the track can be determined with an accuracy of about 10-15 mrad.

Luminosity measurement

Precise measurements of the Standard Model parameters require an accurate knowledge of the luminosity ($\mathcal{L}$). The determination of the luminosity is done by measuring the rate of small angle Bhabha scattering events ($e^+e^\perp \to e^+e^\perp$). The integrated luminosity is calculated by using the formula:

$$\int \mathcal{L}\, dt = \frac{N_{\mathrm{Bhabha}}}{\sigma_{\mathrm{Bhabha}}}, \tag{3.3}$$

where N_{Bhabha} is the number of Bhabha events and σ_{Bhabha} is their corresponding cross-section, which is theoretically computed with the programme `BHLUMI` [68] taking into account the experimental acceptance. The statistical and systematic errors in the luminosity measurement are respectively 0.4% and 0.6%. The systematic error includes a theoretical error in the cross-section calculation of 0.11%. .

Three different subdetectors installed around the beam pipe are responsible for providing a luminosity measurement in ALEPH:

- **The Luminosity CALorimeter (LCAL)** is a lead/wire calorimeter similar to ECAL in its operation. It consists of two pairs of semi-circular modules placed around the beam pipe at each end of the detector. Its acceptance in polar angle goes from 45 to 160 mrad. At LEP2, it is the responsible

for providing the "official" ALEPH luminosity. The luminosity measurement consists essentially of "counting" the number of events for which there have been two back-to-back deposits of energy compatible with the beam energy, the standard way for identifying Bhabha scattering events.

- **The SIlicon luminosity CALorimeter (SICAL)** was installed in September 1992 on each side of the interaction region. It is a cylindrical calorimeter around the beam pipe with 12 silicon/tungsten layers used to sample the showers produced by small angle Bhabha events. During the LEP1 phase, it provided the "official" ALEPH luminosity since it improved the statistical precision of the luminosity measurement by sampling at smaller angles than LCAL. The systematic error on the luminosity was also reduced thanks mainly to the greater precision in the positioning of its components. At LEP2, the luminosity provided by SICAL is not used to normalize the physics processes cross-sections in ALEPH, because it is partially "hidden" by the masks installed to protect the central detectors from the synchrotron radiation, much higher than at LEP1. Instead, it is used to improve the ALEPH acceptance at very low angle.
- **The Bhabha CALorimeter (BCAL)**, located behind the final focus quadrupoles, consists of a system of four modules, each of them being a sampling calorimeter made of tungsten converter sheets interspersed with sampling layers of plastic scintillator, plus a single plane of silicon strips with $r\phi$ segmentation. This plane is used to locate the shower position. BCAL gives a measurement of the instantaneous luminosity and acts as a background monitor. It is sited at very low angles, allowing high statistics at the cost of increased systematic errors.

Beam monitoring

A monitoring of the beam conditions is needed for the optimization of the LEP performance. The background is monitored by the Small Angle Monitor of BAckground (SAMBA) positioned in front of LCAL at each end of the detector. Other devices located around the circumference of LEP, called Beam Orbit Monitors (BOM's), are used to measure the mean position and angle of the beam orbits. This information is used by LEP to optimize the beam conditions, and by ALEPH to determine the

(x, y) position of the beam spot as a starting point for offline reconstruction of the primary vertex.

Trigger system

The main purpose of the ALEPH trigger is to identify all events coming from $e^+e^\perp$ annihilations and reduce to a low level the rate of useless events (mainly due to collisions of the beam with the residual gas, the off-momenta beam electrons hitting the beam pipe walls, electronic noise, cosmic rays, bremsstrahlung radiation photons) in order to avoid dead time in the detector and a large amount of useless data. The trigger system, designed to be sensitive to single particles or single jets, produces a signal that starts the readout of the events, which must be adjusted so that the TPC is gated at an acceptable low rate and the dead time induced by readout is negligible. The trigger system is organized in a three-level structure, the first two levels being hardware implemented in order to give a very fast answer, while the third one is software implemented:

- The **level one trigger** decides whether or not to read out all the detector elements. Its purpose is to operate the TPC at a suitable rate. The decision is taken approximately $5\,\mu$s after the beam crossing (fast decision when compared to the time between two bunch crossings, $11\,\mu$s) from pad and wire information from ECAL and HCAL, and hit patterns from the ITC. The level one rate must not exceed a few hundred Hz. For a negative decision the TPC is reset and kept ready for the next event, while for a positive decision the digitization of the signals is initiated.

- The **level two trigger** refines the level one charged track triggers by using the TPC tracking information for checking if the trajectories of the charged particles originate close to the interaction point. If the level one decision cannot be confirmed, the readout process is stopped and cleared. The decision is taken approximately $50\,\mu$s after the beam crossing (the time at which the TPC tracking information is available). The maximum trigger rate allowed for this level is about 10 Hz.

- The **level three trigger** has access to the information from all detector components and is used to reject background, mainly from beam-gas interactions

and off-momentum beam-particles. It ensures a reduction of the trigger rate to 3-4 Hz, which is acceptable for data storage.

Data Acquisition system

The data acquisition (DAQ) system allows each subdetector to take data independently, processes all the information taken by the detector, activates the trigger system at every beam crossing, writes the data in a storage system following a level two YES decision, and monitors and regulates continuously all the detector and electronic system.

The DAQ [69] architecture is highly hierarchical. Following the data and/or control flow from the bunch crossing of the accelerator down to the storage device, the following components are found:

- Timing, Trigger and Main Trigger Supervisor: synchronize the readout electronics to the accelerator and inform the ReadOut Controllers (ROC's) about the availability of the data.
- ROC's: initialize the front-end modules, read them out and format the data.
- Event Builders (EB's): build a subevent at each subdetector level and provide a "spy event" to a subdetector computer.
- Main Event Builder (MEB): collects the pieces of an event from the various EB's and ensures resynchronization and completeness.
- Level three trigger: performs a refined data reduction, as already seen before.
- Main host and subdetector computers: the main machine (an AXP cluster) initializes the complete system, collects all data for storage and provides the common services. Tasks associated to each subdetector computer get the "spy events" and perform the monitoring of the subdetectors.

The data taken by the online computers is called *raw data* and is reconstructed quasi-online. In less than two hours after the data is taken, the event reconstruction and a check of the quality of the data are done, thus allowing ALEPH to have a fast cross-check of the data and to correct possible detector problems. This task is

performed by the Facility for ALeph COmputing and Networking (FALCON) [70], three AXP processors running the full ALEPH data reconstruction programme JULIA (Job to Understand Lep Interactions in ALEPH) [71] which performs the majority of track fitting and calorimeter reconstruction needed for physics analysis. The output of JULIA provides the quality of the data taken (RunQuality) and is written in POT (Production Output Tape) data files. Finally, the ALPHA (ALeph PHysics Analysis) [72] package is used as an interface allowing easy access to the reconstructed physical quantities of particles such as momenta, energies, etc.

3.3 Event reconstruction and simulation

The reconstruction processes more relevant to the analysis—track reconstruction, energy-flow algorithm—are briefly described together with the different Monte Carlo codes used to generate simulated events.

3.3.1 Tracking in ALEPH

Before any measurement of the momenta and track parameters is performed, the raw data has to be processed and track coordinates have to be measured in order to join them together to finally reconstruct the tracks.

In the TPC, nearby hits are grouped to form clusters (track segments) for which three coordinates are determined. In the ITC, three coordinates are reconstructed as well, taking into account the wire number and the difference of the arrival times of the signals to the two ends of the wire. The reconstruction of the tracks starts in the TPC by connecting track segments to determine tracks consistent with a helix hypothesis. These track candidates are then extrapolated to the inner detectors, ITC and VDET, where consistent hits are assigned [4]. Coordinate errors are determined using the preliminary track parameters. The final track fit, based on Kalman Filter [74] techniques, uses these errors and takes into account multiple scattering

[4] The update of the tracking for VDET is explained in ref. [73]: groups of several nearby tracks which may share common hits are analysed together to find the hit assignments which minimize the overall χ^2 for the event as a whole; and tracks found to originate from a secondary vertex are considered in the VDET hit assignment only after all the other tracks coming from near the interaction point have been considered.

effects between coordinates and the energy loss (when passing through the beam pipe and materials in the tracking detectors) in flight.

The track finding efficiency in the TPC was studied [67] using Monte Carlo hadronic Z^0 events, indicating that 98.6% of tracks that cross at least four pad rows in the TPC are reconstructed successfully; the small inefficiency, due to track overlaps and cracks, is reproduced to better than 0.1% by the simulation. The efficiency of associating a vertex detector hit to an isolated track is about 94% per layer, within the geometrical acceptance. By selecting dimuon events at 45 GeV in the angular acceptance $|\cos\theta| < 0.8$, the transverse momentum resolution is $\sigma(1/p_T) = 1.2 \times 10^{\perp 3}\,(\mathrm{GeV/c})^{\perp 1}$ for the TPC alone, whereas it improves up to $\sigma(1/p_T) = 0.6 \times 10^{\perp 3}\,(\mathrm{GeV/c})^{\perp 1}$ (already mentioned before) when VDET, ITC and TPC are used together.

3.3.2 Energy-flow determination

The energy-flow algorithm [67] is an event-shape algorithm which is used in this work to analyse hadronic events.

The simplest way to determine the energy-flow of an event recorded in the ALEPH detector is to make the sum of the raw energy found in all calorimetric cells without performing any particle identification. The energy resolution of this naive method is very limited:

$$\sigma(E) = 1.2\sqrt{E/\mathrm{GeV}} \tag{3.4}$$

for hadronic Z^0 decays. A better solution is the one performed by the energy-flow reconstruction algorithm, which makes use of the track momenta and takes advantage of the photon, electron and muon identification capabilities to improve the energy resolution.

A first cleaning procedure is applied to eliminate poorly reconstructed tracks, noisy channels of ECAL and HCAL, and fake energy deposits in the calorimeter towers. This is done by identifying the charged particle tracks with at least four hits in the TPC originating from within a cylinder of length 20 cm and radius 2 cm centred at the nominal interaction point and coaxial with the beam direction, reconstructed using the information of the VDET, the ITC and the TPC.

Afterwards, the charged particle tracks are extrapolated to the calorimeters, and groups of topologically connected tracks and clusters (so-called *calorimeter objects*) are formed. The tracking detectors together with the calorimeters give redundant information, for example, when summing up all the energy. In order not to double count the same information, the calorimetric energy already associated to charged particle tracks is not taken into account: photons and π^0's (counted as neutral electromagnetic energy), charged particle tracks identified as muons, and those identified as electrons, together with the energy contained in the associated electromagnetic calorimeter towers, are removed from each calorimeter object.

At this stage, the only particles left in the 'calorimeter object list' should be charged and neutral hadrons. All charged particle tracks coming from the nominal interaction point or belonging to a reconstructed V^0 (long-lived neutral particles decaying into two oppositely-charged particles) are counted as charged energy assuming they are pions. Concerning the neutral hadron energy, a specific identification of neutral hadrons in the calorimeters is not done. However, they are identified as a significant excess of calorimetric energy: in a given calorimeter object, the remaining energy left in the calorimeters is summed, after first scaling that from the electromagnetic calorimeter by the ratio of the calorimeter's response to electrons and pions. If this sum exceeds the energy of any remaining charged particle tracks, and the excess is both larger than the expected resolution on that energy when measured in the calorimeters, and greater than 500 MeV, then it is counted as neutral hadronic energy.

As a result of this algorithm, a set of *energy-flow objects* (electrons, muons, photons, charged or neutral hadrons) is obtained, all of them characterized by their energies and momenta. All the clusters found in the luminosity monitors, where no particle identification is available, are added to this list. This list is expected to be a close representation of the reality, i.e. of the particles actually produced in the collision. Neutrinos, which escape undetected, are indirectly detected by the presence of missing energy in the event.

The energy resolution of the energy-flow algorithm was studied by reconstructing the peak of the invariant mass of the Z^0 from hadronic decays. The resulting energy resolution could be parametrised as [67]:

$$\sigma(E) = (0.59 \pm 0.03)\sqrt{E/\mathrm{GeV}} + (0.6 \pm 0.3)\ \mathrm{GeV}, \tag{3.5}$$

representing a big improvement with respect to what was obtained from the calorimeters alone (eq. (3.4)).

3.3.3 The event simulation

The different physics analyses use Monte Carlo simulated events in order to evaluate background contaminations, compute acceptances and efficiencies and, in general, compare the theoretical models to the experimental results. The chain followed to produce simulated events is:

- Generation of event kinematics. The different particle four-momenta are generated according to the different physics processes. In ALEPH, the different Monte Carlo codes to generate each physics process are unified through a common interface: `KINGAL` [75].

- Simulation of the detector response. This is done by using a `GEANT` [76] based programme (`GALEPH` [77]) where all the information about the geometry and materials involved in the experimental setup are described. For the tracking simulation, the primary long-lived particles are followed through the detector. Secondary particles are also produced by interaction with the detector material. Bremsstrahlung, Compton and ionization are some of the processes simulated. `GEANT` and `GHEISHA` [78] are used to simulate the electromagnetic and nuclear interactions of particles with matter respectively. The energy depositions are converted into measurable electrical signals.

- Reconstruction. The same reconstruction programme (JULIA) used for the real data is used for the simulated events. Therefore, the output of all the simulation processes has the same format as that of the real data.

Monte Carlo generators

Different Monte Carlo packages are used to generate the different physics processes produced in ALEPH at 172 GeV and 183 GeV energies. A brief description of the Monte Carlo's used to simulate the signal (W^+W^-) and background events in this analysis is given in the following.

- `KORALW` **[79]** $W^+W^\perp$ **signal Monte Carlo**:
  This programme (version 1.21) includes multiphoton initial state radiation with finite photon transverse momentum via Yenni-Frautschi-Suura exponentiation [80], final state radiation via `PHOTOS` [81], and Coulomb correction [28]. It can generate `CC03` diagrams, which correspond to the three Feynman diagrams that contribute to the production of two resonant W's at tree-level (fig. 2.1), or include four-fermion diagrams computed with the `GRACE` package [9]. Fixed W and Z^0 widths are used, and loose cuts are applied at the generator level on the outgoing electron angle of the fermion-antifermion pair invariant masses in order to avoid regions of phase space with poles in the cross-section. The $W^+W^\perp$ events produced in these regions would in any case be rejected by the selection cuts. The `JETSET` package [40] takes care of gluon radiation and hadronisation. In four-quark final states, the colour flow between fermions is chosen with probabilities proportional to the matrix elements squared for $W^+W^\perp$ and Z^0Z^0 production [82]. Colour flow between two fermions produced by two different bosons, known as colour reconnection (see section 2.7.1 for a description), is not included.

- `EXCALIBUR` **[42]** $W^+W^\perp$ **signal Monte Carlo**:
  It can generate all diagrams (at tree-level) contributing to a given four-fermion final state, including initial state radiation collinear with the beams [83], final state radiation via `PHOTOS`, Coulomb correction and hadronisation by `JETSET`. In the hadronisation process, colour reconnection can be included following the ansatz of ref. [41]. The same loose cuts as above are applied.

- **Monte Carlo's of background processes**:
  Annihilation into quark pairs, $e^+e^\perp \to q\bar{q}(\gamma)$, are mainly simulated with `PYTHIA` [40] although, in order to assess the systematic effect of a different hadronisation model, a sample of events using `HERWIG` 5.8d [43] is also generated. Two photon ($\gamma\gamma$) reactions into leptons and hadrons are simulated with `PHOT02` [84] and `PYTHIA` generators. Dileptons final states are generated with `KORALZ` [85] and `UNIBAB` [86]. `PYTHIA` is also used for various processes leading to four-fermion final states such as: Z^0Z^0, $Z^0e^+e^\perp$, $Z^0\nu\bar{\nu}$ and $We\nu$. This last process is simulated with the electrons generated to smaller angles than the acceptance cut used in the production of the four-fermion events.

3.3.4 Monte Carlo samples used in the 172 GeV analysis

At 172 GeV, samples of 100000 W^+W^- events are generated with KORALW with three different values of the W mass: 79.25, 80.25 and 81.25 GeV/c^2 for all four-fermion (4f) WW-like diagrams. Seven additional samples of 20000 events each are generated with W masses of 79.25, 79.75, 80.00, 80.25, 80.50, 80.75 and 81.25 GeV/c^2.

A comparison sample is generated with EXCALIBUR with $M_W = 80.25$ GeV/c^2 for all four-fermion diagrams. In order to assess the impact of colour reconnection effects, the same events (at the parton level) are hadronised following the ideas in ref. [41].

Background Monte Carlo samples, with integrated luminosities corresponding to at least ten times that of the data, are fully simulated for all relevant background reactions.

Generator	4f KORALW			
M_W(GeV/c^2)	79.25	79.75	80.00	80.25
Number of events	110000	20000	10000	120000
Cross-section (pb)	13.27	12.98	12.82	12.64
Generator	4f KORALW			CC03 KORALW
M_W(GeV/c^2)	80.50	80.75	81.25	80.25
Number of events	10000	20000	110000	20000
Cross-section (pb)	12.46	12.24	11.80	12.37

Table 3.1: Table of W^+W^- Monte Carlo events used in the 172 GeV analysis.

Generator	PYTHIA				KRLZ08
Process	$q\bar{q}(\gamma)$	Z^0Z^0	Z^0ee	2-γ	τ pairs
Number of events	475000	13056	7000	200000	5000
Cross-section (pb)	121.1	3.066	6.52	1600	10.8

Table 3.2: Table of background Monte Carlo events used in the 172 GeV analysis.

3.3.5 Monte Carlo samples used in the 183 GeV analysis

The same Monte Carlo packages as the ones used for the 172 GeV analysis are used. The KORALW Monte Carlo is used to produce the W^+W^- events with the complete set of four-fermion diagrams. A big W^+W^- Monte Carlo production, 400000 events, is done with a W mass value of $M_W = 80.35\,\mathrm{GeV}/c^2$, chosen because it is closer to the world average value. At this mass, the decay width is calculated from Standard Model predictions with $\alpha_s = 0.118$ to be $\Gamma_W = 2.094\,\mathrm{GeV}$. Four additional samples are generated with W masses of 79.85, 80.10, 80.60 and 80.85 GeV/c^2.

In addition, an independent sample of 300000 signal events is generated with KORALW restricted to the doubly resonant CC03 diagrams with a cross-section of 15.71 pb.

Monte Carlo samples at 183 GeV with integrated luminosities corresponding to at least 80 times that of the data, are fully simulated for the most important background reactions. PYTHIA is used to generate 600000 $e^+e^- \to q\bar{q}(\gamma)$ events with a cross-section of 107.6 pb and also 30000 Z^0Z^0 and 60000 Z^0ee events.

Generator	4f KORALW					CC03 KORALW
$M_W(\mathrm{GeV}/c^2)$	79.85	80.10	80.35	80.60	80.85	80.35
Number of events	48000	48000	400000	50000	50000	100000
Cross-section (pb)	16.037	16.012	16.015	15.972	15.950	15.73

Table 3.3: Table of W^+W^- Monte Carlo events used in the 183 GeV analysis.

Generator	PYTHIA		
Process	$q\bar{q}(\gamma)$	Z^0Z^0	Z^0ee
Number of events	600000	30000	60000
Cross-section (pb)	107.6	2.93	79

Table 3.4: Table of background Monte Carlo events used in the 183 GeV analysis.

Chapter 4

W mass measurement at 172 GeV

This chapter is devoted to describing the W mass measurement using the hadronic channel and the integrated luminosity of $10.65\,\mathrm{pb}^{-1}$ data taken by the ALEPH detector at a mean centre-of-mass energy of 172.09 GeV. The direct reconstruction method is used for the first time at LEP as the kinematical threshold of the W^+W^- production is surpassed. The procedure to select hadronic events is explained in section 4.1. Sections 4.2 and 4.3 are devoted to describing in detail the jet clustering algorithm and the kinematical fit used. The selection of a good jet pairing algorithm is detailed in section 4.4. A method based on a direct comparison of data and reweighted Monte Carlo invariant mass distributions is explained in section 4.5. Section 4.6 is focussed on some Monte Carlo expectations, and the results are given in section 4.7. Some stability checks and systematic studies are summarized in sections 4.8 and 4.9, followed by the conclusions at the end of this chapter.

4.1 Hadronic event selection

The W^+W^- events in the hadronic channel (45.9% of all W^+W^- events) are characterized by a high average multiplicity of charged tracks (~ 35 charged tracks), spherical four-jet like topology and large visible energy, close to the available centre-of-mass energy. The global event topology consists of four (or more) high energetic jets originating from the underlying four-quark structure.

The main source of background to the $e^+e^- \to W^+W^- \to 4q$ process is the $e^+e^- \to Z^0/\gamma \to q\bar{q}(\gamma)$ production. Fortunately, more than 50% of these events are

affected by hard initial state radiation photon emission which boosts the effective two-quark centre-of-mass energy back to the Z^0 mass (the so-called radiative return to the Z^0 events). Such events are characterized by having high missing energy and low invariant mass clustered around the Z^0 mass or, if the γ is detected, a very high energetic γ. In addition, these events tend to have a two-jet structure resulting in a more longitudinal topology, different from the spherical four-jet like topology of the hadronic W's. Additional less important backgrounds come from $e^+e^\perp \to Z^0Z^0$ events and, even less important, $e^+e^\perp \to Z^0ee$ and $e^+e^\perp \to W^+W^\perp \to qq\ell\nu$ events.

In figure 4.1, the first plot on the left compares the high multiplicity of the hadronic events (for which the mean and RMS—root mean square—values are shown) to the multiplicity of semileptonic and $q\bar{q}(\gamma)$ events. The sphericity is shown in the plot on the right, where the highest sphericity values correspond to the hadronic events. The bottom plot on the left shows the total energy, with the semileptonic and radiative return to the Z^0 events showing higher missing energy.

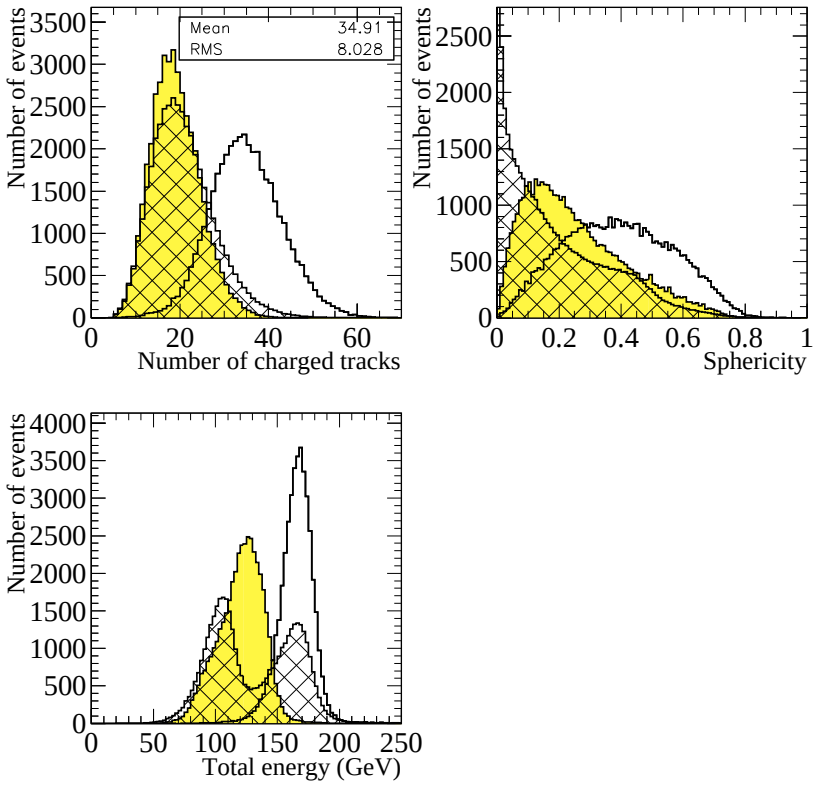

Figure 4.1: Comparison of number of charged tracks, sphericity and total energy distributions for hadronic (empty histogram), semileptonic (full histogram) and $q\bar{q}(\gamma)$ events (hatched histogram). They are normalized to the same number of events.

The purpose of the different steps in the selection is to remove events originating from processes other than $W^+W^- \to 4q$ while keeping high efficiency for the hadronic events.

The initial selection requirements for hadronic candidates to ensure that the event is well detected are the so-called *class* 16 requirements [72], which constitute a minimum set of cuts based entirely on charged tracks measured by the TPC. The events are required to have at least five good tracks [1] in the TPC, and the total energy of all TPC good tracks should have more than 10% of the nominal centre-of-mass energy. These cuts reduce the number of beam-gas, beam-beampipe, cosmic ray, leptonic events (in other words, low multiplicity background events) in the data set.

After these initial requirements, a preselection in order to reject as much background as possible is applied. It consists of the following cuts:

i. The missing energy must be smaller than 40 GeV;

ii. The number of energy-flow objects (defined in section 3.3.2) must be larger than 45;

iii. The number of jets found with the `JADE` algorithm [87] with $y_{cut} = 0.005$ [2] must be larger than three.

   The events are then forced into four jets using the `DURHAM`-P (`DURHAM` cluster algorithm [88] combined with the P-scheme—detailed in appendix A.1). Further preselection cuts are applied to these `DURHAM` jets:

iv. Each jet must contain at least two good tracks;

v. The fraction of electromagnetic to total energy in each jet must be smaller than 0.9 .

To extract the W^+W^- signal with high purity and high efficiency, the main selection is based on the output of a neural network (described in appendix A.4)

[1] A good track must have at least four hits in the TPC, must originate from within a cylinder with radius 2 cm and length 20 cm, centred around the interaction point, and its polar angle θ must satisfy $|\cos\theta| < 0.95$.

[2] The y_{cut} is defined to be the cut-off "distance" from which different clusters are not combined into the same jet. For a detailed explanation see appendix A.1.

with 21 input variables—chosen to optimize the selection efficiency—17 hidden units and one output unit (noted as 21-17-1). The input variables are selected according to their discriminant power (defined in eq. (A.17)) evaluated by comparison of their weight values. The distribution of the output of the neural network conventionally peaks at plus one for signal events and at minus one for background events. Detailed explanations can be found in refs. [89] [90]. The input variables are related to global event properties, flavour tagging to reduce the background from events containing b quarks, properties of jets, and kinematic variables. The most important ones to select $W^+W^\perp$ hadronic events are global event quantities like the total visible energy, followed by jet properties.

The full set of input variables (some of them are defined in appendix A.2) used for the learning [3] of the neural network is listed below, together with their discriminant power (in %):

Global event properties:

- Total visible energy in the event; (4.7%)
- Sum of momenta of all charged tracks in the event; (2.6%)
- Aplanarity; (4.7%)
- Oblateness; (3.8%)
- Fox-Wolfram moment H0; (3.8%)
- Fox-Wolfram moment H2; (5.4%)
- Fox-Wolfram moment H3; (7.0%)
- Fox-Wolfram moment H4. (6.8%)

Heavy Flavour tagging:

- Sum of the b-tag probabilities [4] for the four jets; (4.8%)
- Sum of logarithms of the b-tag probabilities for the four jets; (4.5%)
- Global b-tag probability, constructed from all charged tracks in the event. (2.6%)

[3] The neural network is trained using 8k signal and 8k background—$q\bar{q}(\gamma)$, Z^0Z^0 and semileptonic—events.

[4] The b-tag probability of an ensemble of charged tracks is the product of the probabilities that each track comes from the primary vertex [91]. (b-jets have small probabilities).

Properties of Jets:

– Number of energy-flow objects in the most energetic jet; (5.4%)
– Number of energy-flow objects in the least energetic jet; (3.6%)
– Largest energy fraction carried by one energy-flow object in the most energetic jet; (3.8%)
– Largest energy fraction carried by one energy-flow object in the second most energetic jet; (4.8%)
– Largest energy fraction carried by one energy-flow object in the third most energetic jet; (3.9%)
– Largest energy fraction carried by one charged track in the most energetic jet. (3.5%)

$W^+W^\perp$ **Kinematics:**

– Sum of the cosines of the six angles between the jets; (9.2%)
– Largest of the minimum invariant masses from each of the three possible di-jet combinations; (6.1%)
– Largest invariant mass of all six di-jet combinations; (5.8%)
– Transverse momentum of the highest energetic jet. (3.7%)

The agreement between data and Monte Carlo distributions of each of the input variables above is good (see ref. [89]).

Figure 4.2 shows the neural network output distribution for hadronic $W^+W^\perp$ events generated with $M_W = 80.25\,\mathrm{GeV}/c^2$ and background ($q\bar{q}(\gamma)$ and Z^0Z^0) events. By requiring the neural network output larger than -0.3 , hadronic events are selected with an efficiency of 82.4% and a purity of 77.8% . The efficiency versus purity curve obtained by applying different neural network output cuts is shown in figure 4.3. The arrow in the plot indicates the actual cut (-0.3) applied to the neural network output distribution. The optimization of this cut is discussed in section 4.8.1.

A good performance of a neural network is reflected in a selection efficiency of hadronic $W^+W^\perp$ events independent of the W mass. This is what figure 4.4 shows: the selection efficiencies computed using fully reconstructed four-fermion `KORALW` Monte Carlo's generated with different W mass values as a function of the W mass is independent of the value of the W mass.

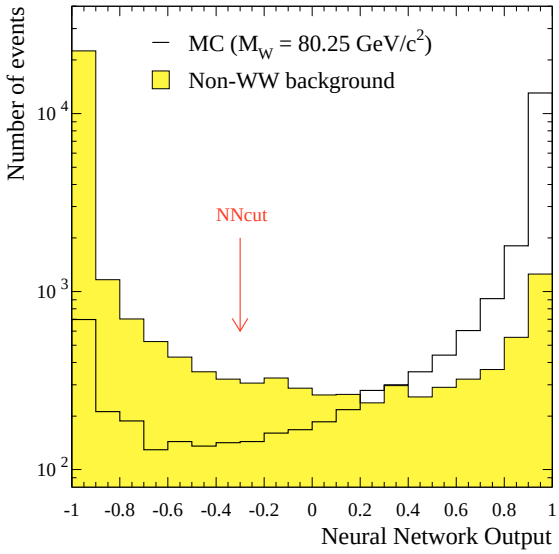

Figure 4.2: Neural network output distribution for Monte Carlo signal events generated with $M_{\mathrm{W}} = 80.25\,\mathrm{GeV}/c^2$ (open histogram) and background events—$\mathrm{q\bar{q}}(\gamma)$, $\mathrm{Z^0Z^0}$—(full histogram). Both histograms are normalized to the same integrated luminosity. The arrow indicates where the cut to the neural network output distribution is applied to select hadronic events: -0.3 .

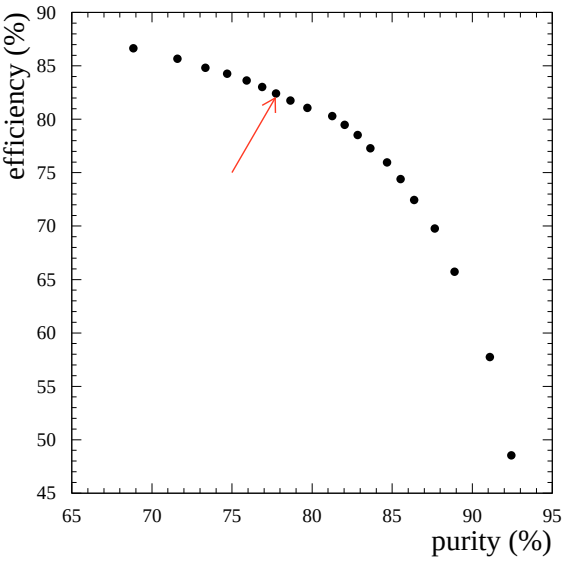

Figure 4.3: Signal efficiency versus purity curve of the neural network obtained by the application of different neural network cuts. The arrow indicates where the actual cut to the neural network output distribution is applied to select hadronic events.

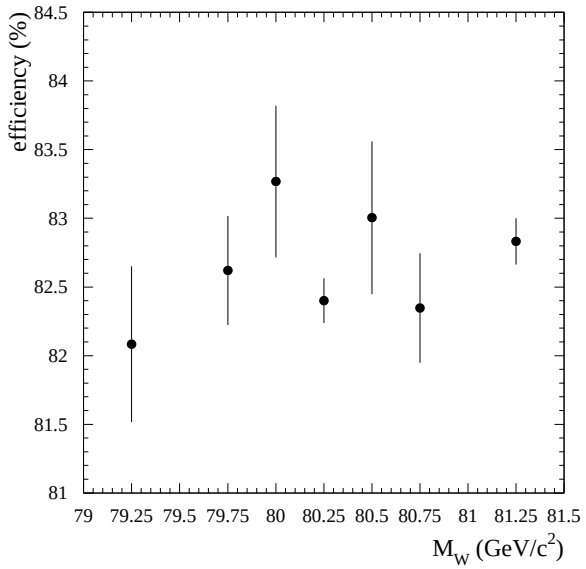

Figure 4.4: Neural network output cut signal efficiency as a function of the W mass.

The number of Monte Carlo events surviving the class 16 requirements, the number surviving the preselection cuts, and the number surviving the neural network cut are summarized in table 4.2 for the different $W^+W^\perp$ channels, and in table 4.3 for the different background processes considered. From these tables, it is obvious that sources of background other than $q\bar{q}(\gamma)$ and Z^0Z^0 are negligible after the neural network output cut.

4.2 Jet clustering algorithm

The most problematic thing when working with the hadronic channel is the reconstruction of its four-quark underlying structure because of the overlap between particles from different W's.

Different jet clustering algorithms are available to cluster the event into jets (see appendix A.1 for a full description of the algorithms). In order to choose the best one (which would match each jet to each quark), a Monte Carlo study is performed using the following matching criterion: each jet (with four-momentum p_{jet}) is matched to the quark (with four-momentum p_{quark}) with which the invariant mass ($p_{\text{jet}} \cdot p_{\text{quark}}$) is minimum. The following cluster algorithms: `DURHAM` [88], `JADE` [87] and `LUCLUS` [92] together with different recombination schemes [93]: E, P

and E_0 are tested with $\sim$19000 hadronic four-fermion KORALW W^+W^- Monte Carlo events.

The quality of each algorithm is checked by studying the energy resolution ($\sigma(E)$), the angular resolutions ($\sigma(\cos\theta)$,$\sigma(\phi)$) and the average shift between the reconstructed and the generated W masses ($< \Delta M_W >$) from both W's. Table 4.1 shows the results of this study for the different algorithms together with the different schemes.

Cluster algorithm	$\sigma(E)$(GeV)	$< \Delta M_W >$(GeV/c^2)	$\sigma(\cos\theta)$	$\sigma(\phi)$
DURHAM-P	13.42	8.07	0.303	0.397
DURHAM-E	14.46	4.01	0.328	0.418
DURHAM-E_0	14.43	4.60	0.311	0.408
DURHAM-PE	14.35	3.97	0.328	0.417
JADE-P	14.38	8.55	0.321	0.418
JADE-E	15.23	4.23	0.351	0.444
JADE-E_0	15.49	4.62	0.338	0.440
JADE-PE	14.83	4.11	0.350	0.442
LUCLUS	15.19	3.92	0.306	0.402

Table 4.1: Energy resolution ($\sigma(E)$), average W mass shift ($< \Delta M_W >$) and angular resolutions ($\sigma(\cos\theta)$, $\sigma(\phi)$) for the different jet clustering algorithms and combination schemes.

DURHAM-P is the one which is the most successful in correctly assigning particles (energy-flow objects) to jets, evaluated in terms of jet energy and angular resolution. However, because the P-scheme assumes massless particles violating energy-momentum conservation, large shifts appear between the reconstructed and the generated W masses. Therefore, in order to avoid this problem and to guarantee the full Lorentz invariance, a mixing between P- and E- schemes is used (DURHAM-PE), i.e. the P-scheme is used to decide which particles are assigned to which jet, and the E-scheme is used afterwards to compute the jet four-momenta.

4.3 Kinematical fit

The fact that four jets are reconstructed per each event results in a smearing of the original quark directions and energies as table 4.1 shows. This is mainly due to

the finite energy resolution of the detector in combination with the loss of particles (loss in the beam pipe and cracks, etc.).

A kinematical fit corrects for some of these effects and translates the measured jet momenta to corrected ones fulfilling, at least, constraints such as energy and momentum conservation. This technique improves the di-jet invariant mass resolution (reconstructed mass minus generated mass) and also provides a useful criterion of background rejection because of the small probability of the events which are originally not four quarks. The `MATHKINE` [94] package, whose principles are explained in appendix A.3, is used to do the kinematical fit.

To apply the constrained fit it is necessary to determine a suitable parametrisation of the jet momenta so that the chosen parameters have distributions close to Gaussian distributions. To allow full freedom for a jet in the constrained fit, three parameters per jet are necessary, giving a total of twelve parameters. Several choices are possible, as for example the jet energies and angles. Inspired by the Gaussian nature of the energy resolution of the detectors and so of the transverse momentum, the measured jet momenta ($\vec{p}_j^{\,m}$) are corrected ($\vec{p}_j^{\,r}$) following the equation:

$$\vec{p}_j^{\,r} = a_j|\vec{p}_j^{\,m}|\vec{u}_j^{\,a} + b_j\vec{u}_j^{\,b} + c_j\vec{u}_j^{\,c}, \tag{4.1}$$

where a_j,b_j,c_j are the correction parameters which depend on the jet energies and directions, and the unit vectors $\vec{u}_j^{\,a}$,$\vec{u}_j^{\,b}$,$\vec{u}_j^{\,c}$ are determined from the measured jet momenta and form a cartesian system. The unit vector $\vec{u}_j^{\,a}$ is defined in the direction of the measured momentum, $\vec{u}_j^{\,b}$ is in the plane defined by the object axis and the z axis, and $\vec{u}_j^{\,c}$ is perpendicular to $\vec{u}_j^{\,b}$. If the reconstruction were perfect, a_j would be 1, while b_j and c_j would be 0. The reconstructed energy of a jet is rescaled:

$$E_j^{\,r} = E_j^{\,m}\frac{|\vec{p}_j^{\,r}|}{|\vec{p}_j^{\,m}|}. \tag{4.2}$$

The expectation values and resolutions of the parameters are extracted from Monte Carlo studies by matching the measured jets to the underlying quarks. These parameters are subject to constraints and are used to built a χ^2. The minimization of this χ^2 is done via an iterative procedure and a more accurate jet energy and momenta are obtained.

Within this package, three possible constrained (C) fits are available:

- **4C** : requiring energy and momentum conservation. It gives two invariant masses per event.

- **5C** : a 4C with the additional constraint that the two reconstructed masses, corresponding to the two W's in the event, are equal to within some resolution.

- **4C+R**escaling : a 4C with the rescaling of the two reconstructed invariant masses (m_{ij}) using the beam energy (E_b):

$$m_{ij}^{resc} = m_{ij} \frac{E_b}{E_i + E_j}, \tag{4.3}$$

  where i, j refer to those jets belonging to the same di-jet and E_i, E_j are the jet energies. Therefore, the rescaled masses are directly related to the velocities of the two W's.

A comparison of the invariant mass resolution (Δm) for each constrained fit is done in figure 4.5. This figure shows that from 4C to 5C or 4C+R, there is an improvement. The invariant mass resolutions for 5C and 4C+R are similar. The 4C+R fit seems to be less sensitive to detector systematic effects [95] and is chosen for this analysis.

The kinematical fit acts as another background rejection criterion as stated in the beginning of this section. The number of Monte Carlo signal and background events for which the fit has converged are shown in tables 4.2 and 4.3 respectively.

4.4 Jet pairing

For each selected event, the four jets can be coupled into two di-jets in three different ways. For each of these combinations, two rescaled 4C masses are determined as explained in the previous section. In figure 4.6 one of the invariant mass distributions for the three possible combinations is shown, the first one being the right one [5]. It is not obvious which one of these partitions is correct and, therefore, a jet pairing algorithm to choose one of them is needed.

[5]The right combination is defined as the combination which matches best the reconstructed jets to the quarks coming from the same W. The jet (with four-momentum p_{jet}) is matched to the quark (with four-momentum p_{quark}) with which the invariant mass ($p_{\text{jet}} \cdot p_{\text{quark}}$) is minimum.

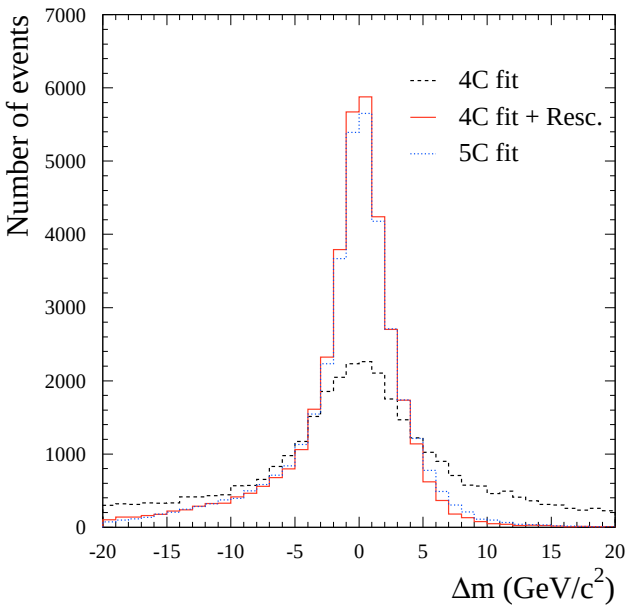

Figure 4.5: Invariant mass resolution for three different kinematical fits: 4C, 4C+R and 5C. The reconstructed invariant masses correspond to the right di-jet combination.

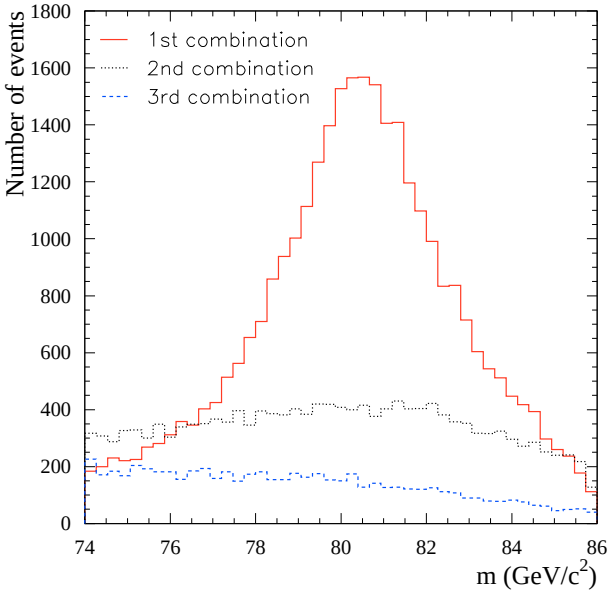

Figure 4.6: Distribution of the invariant mass for the three possible pair-combinations in the window (74,86) GeV/c^2.

Three different pairing algorithms are tested, combined with two different window cuts in the invariant mass. The two possible window cuts are:

- **Window 1**: $50 < (m_1 \text{ and } m_2) < 86$ GeV/c^2 and
  $74 < (m_1 \text{ or } m_2) < 86$ GeV/c^2;
- **Window 2**: $74 < (m_1 \text{ and } m_2) < 86$ GeV/c^2,

where m_1 and m_2 are the two reconstructed invariant masses per event. The jet pairing algorithms tested are defined as:

- **Chi2 Scheme** [35]: Among those combinations with the masses inside the window, the one with the smallest χ^2 from the 5C fit is chosen.
- **Angles Scheme** [96]: The combination chosen is the one with the smallest mass difference unless this is the one with the smallest sum of angles; in this case, the combination with the second smallest mass difference is chosen. Once the combination is chosen, the window cut is applied.
- **Reference Mass Scheme** [97]: The combination chosen is the one minimizing the distance of the two invariant masses to a certain reference mass (M_{W}^{ref}). This distance is defined as: $\Delta m = (m_1 - M_{\mathrm{W}}^{ref})^2 + (m_2 - M_{\mathrm{W}}^{ref})^2$. An iteration is performed using the fitted mass value as the new reference mass. Once the combination is chosen, the window cut is applied.

For the combination chosen by any of these algorithms, the two masses are treated separately, and they are ordered randomly so that the expected distribution for both invariant masses is exactly the same.

The performance of these algorithms is compared on the basis of their final W mass expected error. To compute this error, three hundred independent Monte Carlo samples with the number of events fixed to the expected number for the integrated luminosity of the data ($10.65\,\mathrm{pb}^{\perp 1}$) are built for each pairing algorithm, and fitted using the method explained in section 4.5.1—the reweighting technique. The dispersion of the W mass values obtained is taken as an estimation of the error in the W mass measurement. The pairing algorithm giving the smallest error is chosen.

The results of such experiments show that the errors do not differ very much between *Chi2* and *Angles* schemes, although they are slightly smaller for the second one.

The iterative *reference mass* scheme is not well defined when fitting through a reweighting technique because two distributions vary at the same time: the reference distribution and the distribution of masses because the pairing uses M_{W}^{ref}. Therefore a different type of fit, using a Breit-Wigner function for example (described in the next section), is needed in the intermediate steps.

At the end, the *Angles* scheme combined with the *Window 1* cut is chosen as jet pairing algorithm, since it is the one which provides the smallest expected W mass error and has a simple implementation. The fraction of kinematically fitted events not fulfilling this jet pairing is only 6.7%, and the fraction of selected events for which the right combination is chosen is 75.6%.

The number of Monte Carlo signal and background events fulfilling the conditions of the jet pairing are shown in tables 4.2 and 4.3 respectively. The efficiency after all selection steps is 76.8% and the purity 79.5%. The number of expected events is 59.3 (47.2 signal and 12.1 background events).

Process	$\mathrm{W^+W^-} \to 4\mathrm{q}$	$\mathrm{W^+W^-} \to \mathrm{qq}\ell\nu$	$\mathrm{W^+W^-} \to \ell\nu\ell\nu$
Generated events	45845	43070	11083
Class 16	45761	42897	115
Preselection	41121	912	0
N.N. cut	37780	276	0
Convergence fit	37743	253	0
Pairing & window	35231	229	0
Efficiency (%)	76.85 ± 0.20	0.53 ± 0.03	0
σ^{eff} (pb)	4.43	0.03	0.

Table 4.2: Number of events surviving cuts, final efficiencies and effective cross-sections for the three $\mathrm{W^+W^-}$ decays: 4q (hadronic), $\mathrm{qq}\ell\nu$ (semileptonic) and $\ell\nu\ell\nu$ (leptonic) channels. The events are fully reconstructed four-fermion `KORALW` Monte Carlo events generated with $M_{\mathrm{W}} = 80.25\,\mathrm{GeV}/c^2$.

Process	$q\bar{q}(\gamma)$	Z^0Z^0	Z^0ee	2-γ	τ pairs
Generated events	475000	13056	7000	200000	5000
Class 16	435456	8934	2327	1992	1295
Preselection	29765	1403	51	0	5
N.N. cut	4784	427	11	0	0
Convergence fit	4585	414	7	0	0
Pairing & window	3967	352	6	0	0
Efficiency (%)	0.84 ± 0.01	2.70 ± 0.14	0.09 ± 0.04	0	0
σ^{eff} (pb)	1.02	0.08	0.01	0.	0.

Table 4.3: Number of events surviving cuts, final efficiencies and effective cross-sections for different background processes.

4.5 W mass determination method

The extraction of the W mass can be done by applying different methods which make a more or less optimal use of the information of the mass contained in the $W^+W^\perp$ events. Before the description of the method actually used in this thesis, a short description of other important direct reconstruction methods follows:

(i) **Breit-Wigner method**

It is the simplest method that makes use of the invariant mass reconstruction. It uses the information contained in the invariant mass distribution of the $W^+W^\perp$ decay products. The rescaled mass distributions (m) are fitted individually using an unbinned maximum likelihood fit with a relativistic Breit-Wigner probability density function:

$$F(m) = \frac{M_W \, \Gamma_W}{(m^2 - M_W^2)^2 + M_W^2 \, \Gamma_W^2}. \tag{4.4}$$

However, the invariant mass distributions in data are not exactly Breit-Wigner distributions because of phase space restrictions, detector resolution, radiation losses, background contamination, etc., which distort them relative to the true invariant mass distributions. Therefore, the fitted mass is different from the true mass, and a calibration curve (the fitted mass of a Monte Carlo sample generated with a known input W mass versus the input mass itself) to correct

the bias is needed. In this sense, it is not easy to find a probability density function describing correctly the experimental distribution. This makes this method not optimal for the expected error. Nevertheless, it is worth for cross-checking the results obtained with other techniques.

(ii) **First generation fitting formula** [98]

The idea of this method is to extract the W mass using the information of the mass contained in the two-fold differential cross-section in terms of the two invariant masses. The W mass is obtained by minimizing an event-by-event log-likelihood function with respect to M_{W}:

$$\log(\mathcal{L}(M_{\mathrm{W}})) = \sum_{i=1}^{N} \log \mathcal{P}(s_1^i, s_2^i | M_{\mathrm{W}}), \tag{4.5}$$

where N is the number of events in the sample and $\mathcal{P}(s_1^i, s_2^i | M_{\mathrm{W}})$ is the probability of the event i characterized by the two invariant masses (s_1^i, s_2^i), given M_{W}. This method properly accounts for the kinematics and dynamics of $\mathrm{W}^+\mathrm{W}^\perp$ production but it is not optimal because not all the information of the events is used.

(iii) **Second generation fitting formula**

The W mass is extracted by fitting a probability density function which uses the information of the W mass contained not only in the invariant mass distributions but in the angular variables such as the polar W production angle and the di-jet angles as well. Therefore, an optimal use of all the information of the W boson contained in the W pair events is made. The details of this method are described in ref. [99]. This is the most sophisticated method used to extract the W mass.

A description of the method used in this thesis is detailed below.

4.5.1 Reweighting method

This method [100] consists of comparing the invariant mass distributions of the W pair events (one distribution per each W) of the Monte Carlo to the corresponding ones of the data. This would require a large generation of Monte Carlo samples

with many different W mass values. The M_{W} corresponding to the generated Monte Carlo having the most similar invariant mass distributions to the ones of the data would be taken. Technically, this would require a lot of CPU time and a reweighting procedure is used instead.

The reweighting method relies completely on Monte Carlo simulation. Consequently, it has the advantage that all of the effects distorting the invariant mass distributions are accounted for in the fit. However, it has also the caveat that the effects must be correctly implemented in the Monte Carlo. This problem is present not only in this method but in all methods studied so far.

The reweighting technique requires a generation of a large amount of Monte Carlo events with a reference W mass value (M_{W}^{ref}), e.g. $M_{\mathrm{W}}^{ref} = 80.25\,\mathrm{GeV}/c^2$. To produce reconstructed invariant mass distributions at many different values of M_{W} and W width, the distributions of the reference Monte Carlo are reweighted with the ratio of squared matrix elements:

$$w_i(M_{\mathrm{W}}, \Gamma_{\mathrm{W}}) = \frac{|\mathcal{M}(M_{\mathrm{W}}, \Gamma_{\mathrm{W}}, p_i^1, p_i^2, p_i^3, p_i^4)|^2}{|\mathcal{M}(M_{\mathrm{W}}^{ref}, \Gamma_{\mathrm{W}}^{ref}, p_i^1, p_i^2, p_i^3, p_i^4)|^2}, \tag{4.6}$$

where p_i^j denotes the four-momentum of the outgoing fermion j (f_j) for a particular event i, and $\mathcal{M}(M_{\mathrm{W}}, \Gamma_{\mathrm{W}}, p_i^1, p_i^2, p_i^3, p_i^4)$ is the matrix element of the process $\mathrm{e^+e^-} \to \mathrm{W^+W^-} \to \mathrm{f_1\bar{f}_2f_3\bar{f}_4}$. The matrix element $\mathcal{M}$ is evaluated for the so-called `CC03` diagrams (figure 2.1) [101] which correspond to the three Feynman diagrams that contribute to the W pair production at tree-level. Only the invariant mass distributions of both reconstructed W's per event are considered and reweighted in this analysis, even though other distributions containing information of the W mass (e.g. W production angles) could be as well used and reweighted with the same weight (w_i).

In this analysis, the W width is given the Standard Model value, following eq. (2.7), for a given W mass. For $M_{\mathrm{W}} = 80.25\,\mathrm{GeV}/c^2$, it is set to $\Gamma_{\mathrm{W}} = 2.086\,\mathrm{GeV}$.

The reference Monte Carlo mass distributions are binned and the probability density function for a data event to have a certain invariant mass (m) between two bins, i and $i+1$, with a given W mass is given by:

$$\text{p.d.f.}\,(m_i \le m < m_{i+1} \mid M_{\mathrm{W}}) = \rho_s(M_{\mathrm{W}})\,\frac{N_s^i(M_{\mathrm{W}})}{\Delta m_i N_s^{TOT}} + \rho_b(M_{\mathrm{W}})\,\frac{N_b^i}{\Delta m_i N_b^{TOT}}, \tag{4.7}$$

where Δm_i is the size of the bin: $m_{i+1} - m_i$, ρ_s is the signal purity, the purity of the background is $\rho_b = 1 - \rho_s$, $N_s^i(M_{\mathrm{W}})$ is the weighted number of signal events from the reference Monte Carlo in the reconstructed mass bin (i):

$$N_s^i(M_{\mathrm{W}}) = \sum_{j=1}^{n_s^i} w_j(M_{\mathrm{W}}) \tag{4.8}$$

(n_s^i being the number of signal events from the reference Monte Carlo sample found in bin i) and N_b^i is the total number of background events found in the same bin. Background events do not depend on the W mass and, therefore, the shape and absolute normalization of the background do not change in the reweighting procedure. N_s^{TOT} and N_b^{TOT} are the number of total signal and background events respectively:

$$N_s^{TOT} = \sum_{i=1}^{N_{bin}} N_s^i(M_{\mathrm{W}}); \qquad N_b^{TOT} = \sum_{i=1}^{N_{bin}} N_b^i, \tag{4.9}$$

where N_{bin} is the number of reconstructed mass bins.

The main dependence on the W mass is given by the weights, but there is a residual dependence on M_{W} through the purity of the selection. Assuming that the selection efficiency does not depend on M_{W} (see figure 4.4) there is only a marginal dependence due to the $\mathrm{W^+W^\perp}$ cross-section ($\sigma_s(M_{\mathrm{W}})$). This dependence is parametrised (by using the `GENTLE` package [102]) with a simple parabola restricted to the region nearby the reference mass ($M_{\mathrm{W}}^{ref} = 80.25\,\mathrm{GeV}/c^2$), resulting in the following expression:

$$\sigma_s(M_{\mathrm{W}}) \;=\; \sigma_s(M_{\mathrm{W}}^{ref}) \left(1 - 0.063(M_{\mathrm{W}} - M_{\mathrm{W}}^{ref}) - 0.0080(M_{\mathrm{W}} - M_{\mathrm{W}}^{ref})^2\right). \tag{4.10}$$

Denoting the efficiency of the selection for signal as ϵ_s and the background efficiency as ϵ_b, the dependence of the signal purity on M_{W} can be written as:

$$\rho_s(M_{\mathrm{W}}) = \frac{\epsilon_s\,\sigma_s(M_{\mathrm{W}})}{\epsilon_s\,\sigma_s(M_{\mathrm{W}}) \;+\; \epsilon_b\,\sigma_b}. \tag{4.11}$$

The size of the reconstructed mass bins of the reference Monte Carlo, signal and background, is the same. The bin widths are obtained by requiring a statistical precision approximately constant along the invariant mass distribution of the reference Monte Carlo: Δm_i is chosen to be narrower near the invariant mass peak ($\sim 10\,\mathrm{MeV}/c^2$) and broader in the tails ($\sim 100\,\mathrm{MeV}/c^2$).

The compatibility of the Monte Carlo and data invariant mass distributions is calculated with a likelihood procedure, and the best estimator of the W mass is the one that maximizes the likelihood function:

$$\mathcal{L}(M_{\mathrm{W}}) = \prod_{i=1}^{N_{evt}} \text{p.d.f.}(m_i \mid M_{\mathrm{W}}), \tag{4.12}$$

N_{evt} being the number of selected data events which enter in the minimization. The estimator obtained does not need to be calibrated because this method automatically gives the correct parameter to be identified with the W mass.

The reweighting method uses a rather large number of reference Monte Carlo events compared to data, typically between 15 and 20 times the luminosity of the data. As the two invariant mass distributions are used independently, this method is called the 1D-method (using one distribution at a time).

Figure 4.7 shows how the reweighting method changes the invariant mass distribution from a reference W mass value ($M_{\mathrm{W}}^{ref} = 80.25\,\mathrm{GeV}/c^2$) to two different M_{W} values: 79.25 and $81.25\,\mathrm{GeV}/c^2$. All the distributions are normalized to the same number of events.

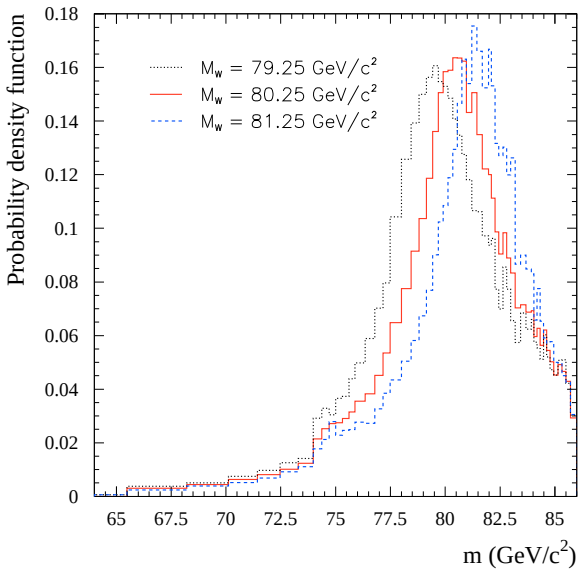

Figure 4.7: Invariant mass distributions for a reference W mass value: $80.25\,\mathrm{GeV}/c^2$ and for two reweighted values: 79.25 and $81.25\,\mathrm{GeV}/c^2$. All distributions are normalized to the same number of events.

Statistical power of weighted events

Weighted events have a limited statistical power. For a set of n events the sum of the weights (S) and the statistical error of the sum (σ_S) are given by:

$$S = \sum_{i=1}^{n} w_i \quad \text{and} \quad \sigma_S = \left(\sum_{i=1}^{n} w_i^2 \right)^{1/2}. \tag{4.13}$$

The effective number of generated events (n_{eff}) can be obtained as:

$$n_{eff} = \frac{\left(\sum_{i=1}^{n} w_i \right)^2}{\left(\sum_{n=1}^{n} w_i^2 \right)}. \tag{4.14}$$

If n_{eff} is small compared to the true number of generated events (n) the Monte Carlo simulation is inefficient. The ratio of the effective number of events when reweighting a Monte Carlo with $M_{\mathrm{W}}^{ref} = 80.25\,\mathrm{GeV}/c^2$ to different W masses, divided by n is shown in figure 4.8.

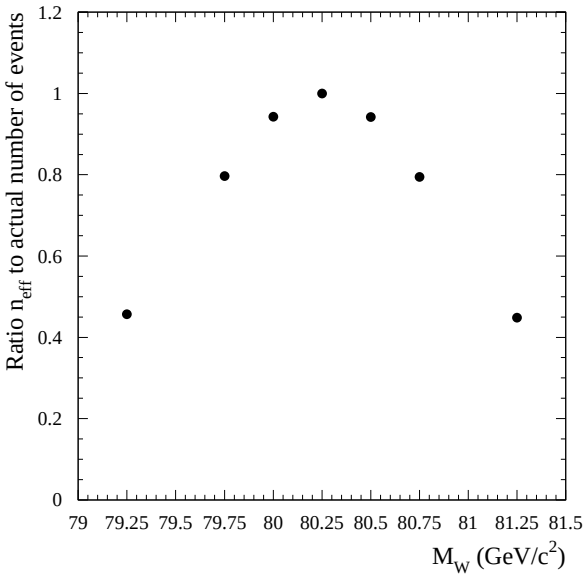

Figure 4.8: Ratio of effective to actual number of events for different W masses to which the reference Monte Carlo with $M_{\mathrm{W}}^{ref} = 80.25\,\mathrm{GeV}/c^2$ is reweighted.

It is important to note that going away $1\,\mathrm{GeV}/c^2$ from the reference W mass value, only less than half of the events are effectively taken into account because of the weighting. In order to have the biggest effective number of reference Monte Carlo events when fitting them to the data, this technique should be applied from a reference sample with M_W the closest to the fitted W mass value as possible.

Figure 4.9 shows the distributions of weights when the reference sample with $M_\mathrm{W}^{ref} = 80.25\,\mathrm{GeV}/c^2$ is reweighted to other masses. Those distributions reweighted to very different W mass values have a large RMS. This shows that the more different M_W is from M_W^{ref}, the more different from unity the weights become, lowering the effective number of events as has already been shown.

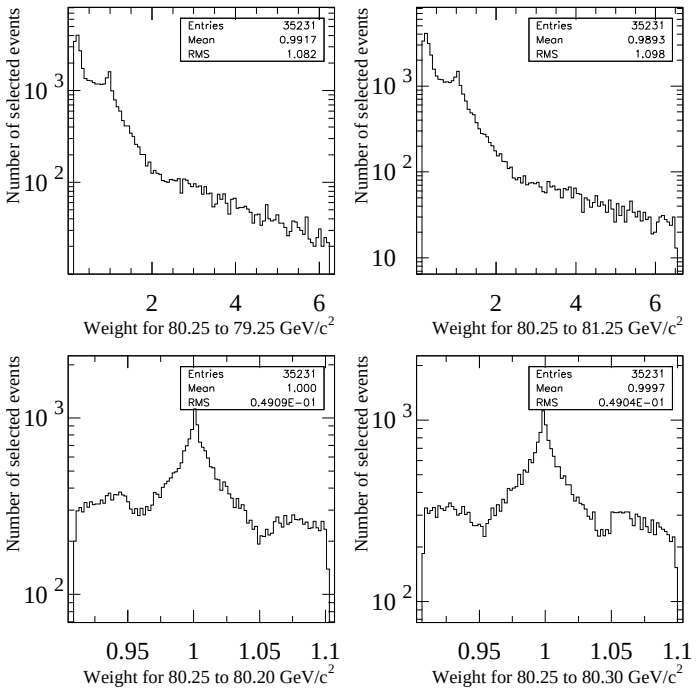

Figure 4.9: Event weights when WW $\to$ 4q events at $M_\mathrm{W} = 80.25\,\mathrm{GeV}/c^2$ are reweighted to $M_\mathrm{W} = 79.25$, 81.25, 80.20 and $80.30\,\mathrm{GeV}/c^2$ respectively.

4.6 Monte Carlo expectations

4.6.1 Correlation between reconstructed masses

Two masses, one per di-jet, are reconstructed per event. Figure 4.10 shows how these two masses (m_1 and m_2) are distributed in the mass range (74,86) GeV/c^2, defined by the window cut. The plot corresponds to approximately 4000 pb$^{\perp 1}$ of signal and background Monte Carlo events in the adequate proportion. The correlation between the two masses is found to be: $66.7 \pm 0.3\%$.

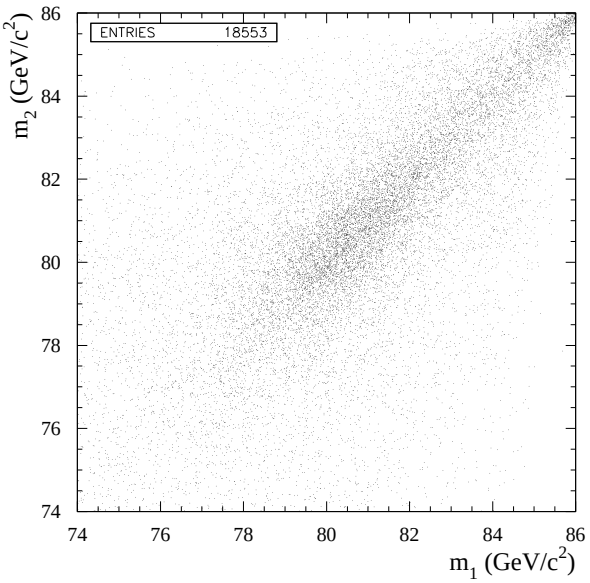

Figure 4.10: Correlation between the two event-by-event reconstructed invariant masses for Monte Carlo events.

4.6.2 Expected error

Due to the small size of the data sample (10.65 pb$^{\perp 1}$ which corresponds to 59.3 expected events) the statistical error of the fit has a large uncertainty. In order to estimate the expected statistical error, three hundred independent Monte Carlo samples of the same integrated luminosity as the data, such that they contain the expected number of events, are used to obtain an estimation of the statistical

error, called the *expected error*. Figure 4.11 shows the distributions of the two mass estimators ($\hat{m}_1$ and $\hat{m}_2$) as well as the distributions of the corresponding positive and negative errors. The agreement between the RMS of the mass estimator distributions and the mean value of the positive and negative error distributions is good. Since the uncertainty on the mean value of the mass error distribution is smaller than the uncertainty on the RMS of the mass distribution, the mean value of the fit error, which is $0.58\,\mathrm{GeV}/c^2$, is taken as the expected error for a sample of the size of the data, for each of the two hadronic masses. Note that there is no discrepancy between the expectation for both estimators.

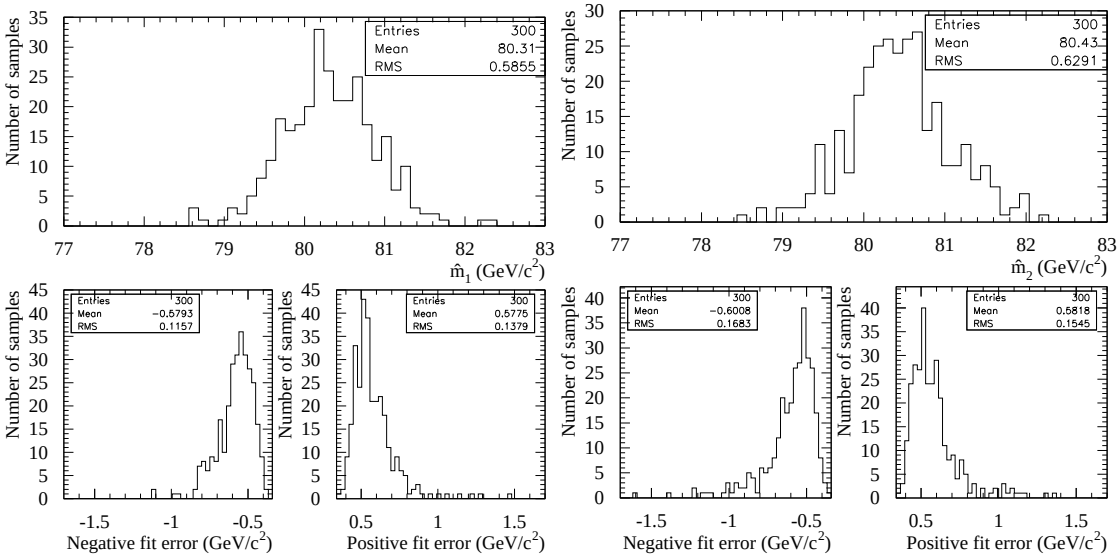

Figure 4.11: Distributions of the two estimators with their positive and negative errors for three hundred independent Monte Carlo samples of the same size of the data.

4.6.3 Correlation between estimators

The expected correlation between the two estimators can be determined using the three hundred Monte Carlo samples of the previous section. Figure 4.12 shows how these estimators are distributed. Their correlation is found to be $33.2 \pm 5.1\%$, having checked that this correlation is independent of the W mass.

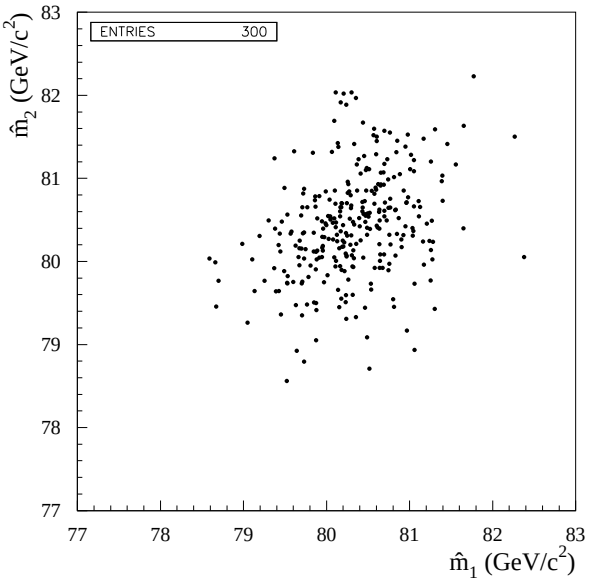

Figure 4.12: Correlation between the two mass estimators ($\hat{m}_1$ and $\hat{m}_2$) for three hundred Monte Carlo samples of the same size of the data.

4.6.4 Calibration curves

A test that ensures that the fitted W mass is not biased is the test known as the *calibration curve*: the W mass values obtained from fits of Monte Carlo samples generated with different M_{W} should match with the input Monte Carlo W masses. The linearity of the fitted mass with respect to the true input mass is studied using seven independent Monte Carlo samples (of $500\,\mathrm{pb}^{\perp 1}$ each) with different input masses (the samples contain signal and background events in the adequate proportion). Figure 4.13 shows the two fitted masses as a function of the generated ones. A straight line, $m = P_1 + P_2(M_{\mathrm{W}}^{true} - 80.25)$, is fitted to the points. The result of the fit together with the ideal line, $m = M_{\mathrm{W}}^{true}$, are shown. The fitted lines are compatible with the ideal lines with a slope value consistent with one and no significant offsets.

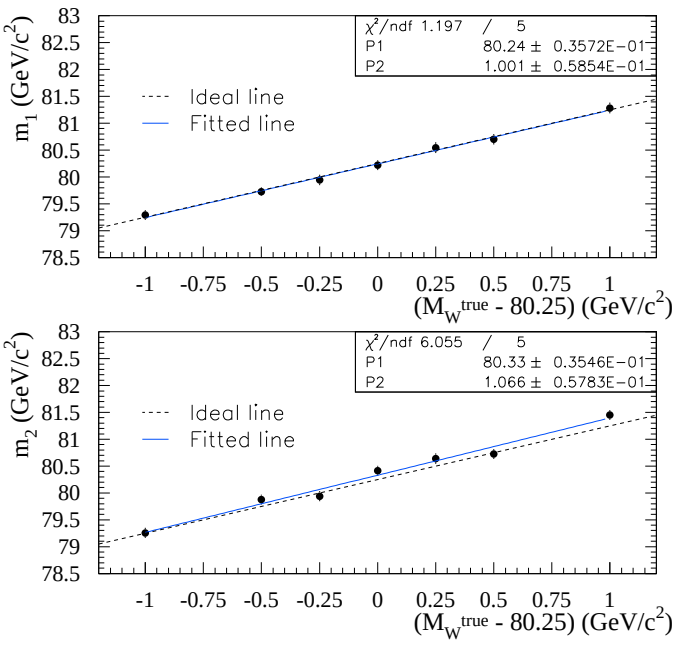

Figure 4.13: Fitted mass versus generated mass for seven Monte Carlo samples of 500 pb^{-1} each. The full lines correspond to the result of the fit and the dashed ones to the ideal case ($m = M_{\mathrm{W}}^{true}$). The two plots correspond to the two fitted masses per experiment.

4.7 Results

The number of selected events in the data after all the requirements described in the previous sections is 65. The Monte Carlo predicts 59.3 events (47.2 of signal and 12.1 of background) compatible with the number of observed events. Figure 4.14 shows the correlation between the two rescaled event-by-event invariant masses in the range (74,86) GeV/c^2. Their correlation is found to be $63.5 \pm 7.4\%$, in good agreement with the Monte Carlo expectation of $66.7 \pm 0.3\%$ (found in section 4.6.1).

By using the reweighting technique with a reference Monte Carlo sample generated with $M_{\mathrm{W}}^{ref} = 80.25\,\mathrm{GeV}/c^2$, the results of the fit to the selected data events, which fall in the mass window (74,86) GeV/c^2, are:

$$\begin{aligned} m_1 &= 81.23^{+0.56}_{\perp 0.51}\ \mathrm{GeV}/c^2 \\ m_2 &= 81.13^{+0.74}_{\perp 0.72}\ \mathrm{GeV}/c^2. \end{aligned}$$

The combination of these two results using the expected correlation (33.2%),

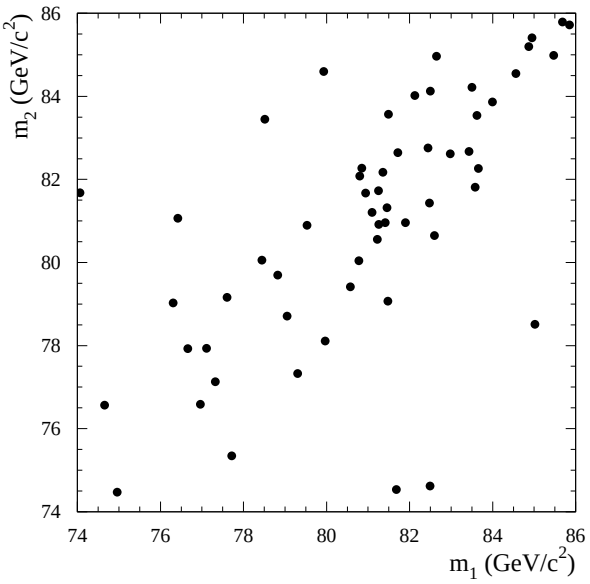

Figure 4.14: Correlation between the two event-by-event reconstructed masses for the selected data events.

found in section 4.6.3, and the expected error ($0.58\,\mathrm{GeV}/c^2$), gives:

$$M_{\mathrm{W}} = 81.18 \pm 0.47\,\mathrm{GeV}/c^2. \tag{4.15}$$

As explained in section 4.5.1, a large effective reference Monte Carlo sample is needed in the reweighting method. Since the fit result is closer to 81.25 than $80.25\,\mathrm{GeV}/c^2$, the method is reapplied to the data by using the reference Monte Carlo sample generated with $M_{\mathrm{W}} = 81.25\,\mathrm{GeV}/c^2$. The results of the fitted masses are:

$$\begin{aligned} m_1 &= 81.40^{+0.52}_{\perp 0.53}\ \mathrm{GeV}/c^2 \\ m_2 &= 81.13^{+0.56}_{\perp 0.62}\ \mathrm{GeV}/c^2. \end{aligned}$$

When the Z^0 mass was measured at LEP1, a mass definition corresponding to a propagator including a s-dependent width was used, whereas in the formulae and Monte Carlo used to extract the W mass, a Breit-Wigner propagator with fixed-width is used. To make both measurements consistent with each other, a positive

shift of 27 MeV/c^2 (see a discussion in section 2.3.3) is applied throughout on the measured W mass, giving the results:

$$m_1 = 81.43^{+0.52}_{\perp 0.53}\ \mathrm{GeV}/c^2 \quad (4.16)$$

$$m_2 = 81.16^{+0.56}_{\perp 0.62}\ \mathrm{GeV}/c^2. \quad (4.17)$$

The combination of these two measurements as done before gives a final W mass result of:

$$M_\mathrm{W} = 81.30 \pm 0.47\ \mathrm{GeV}/c^2. \quad (4.18)$$

Figure 4.15 shows the mass distribution (m_1 and m_2 combined) for the selected data events. The Monte Carlo distributions (signal+background) for the fitted mass, $M_\mathrm{W} = 81.30\ \mathrm{GeV}/c^2$, as well as the background Monte Carlo distribution are shown.

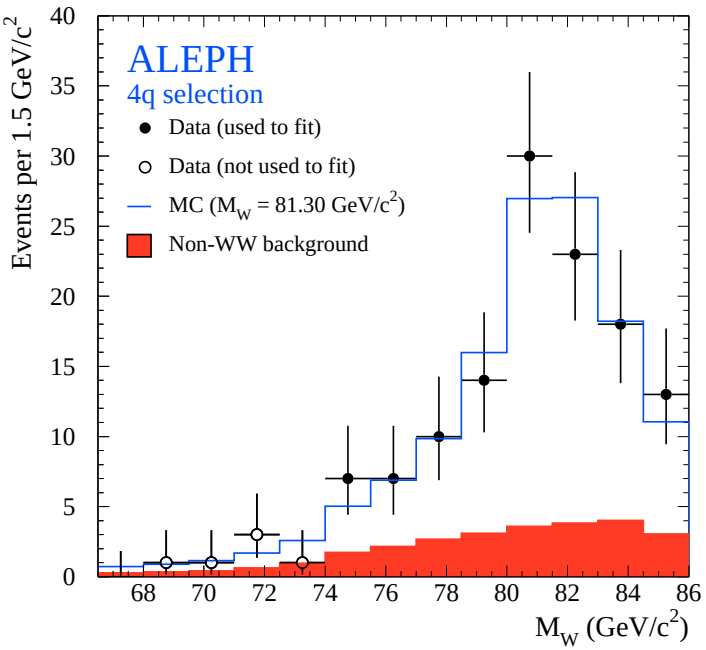

Figure 4.15: Mass distribution (m_1 and m_2) for hadronic data (points with error bars), background Monte Carlo (shaded area) and signal+background Monte Carlo for the best fit to the data taken at 172 GeV (empty histogram).

4.8 Stability checks

4.8.1 Event selection and mass range dependence

The events are selected by requiring the neural network output to be larger than -0.3 . The stability of the result as a function of this cut is studied by using a single sample of $500\,\mathrm{pb}^{\perp 1}$ Monte Carlo events. The left part of figure 4.16 (top plot) shows the fitted masses as a function of the neural network output cut. The errors on the points are highly correlated because the same single sample is used for all the points. The bottom plot on the left in the same figure shows the expected error as a function of the cut. No statistically significant differences are observed in the fitted masses. The fitted masses to the selected data events as a function of the neural network output cut is shown on the right of the same figure. The same conclusion as before is reached.

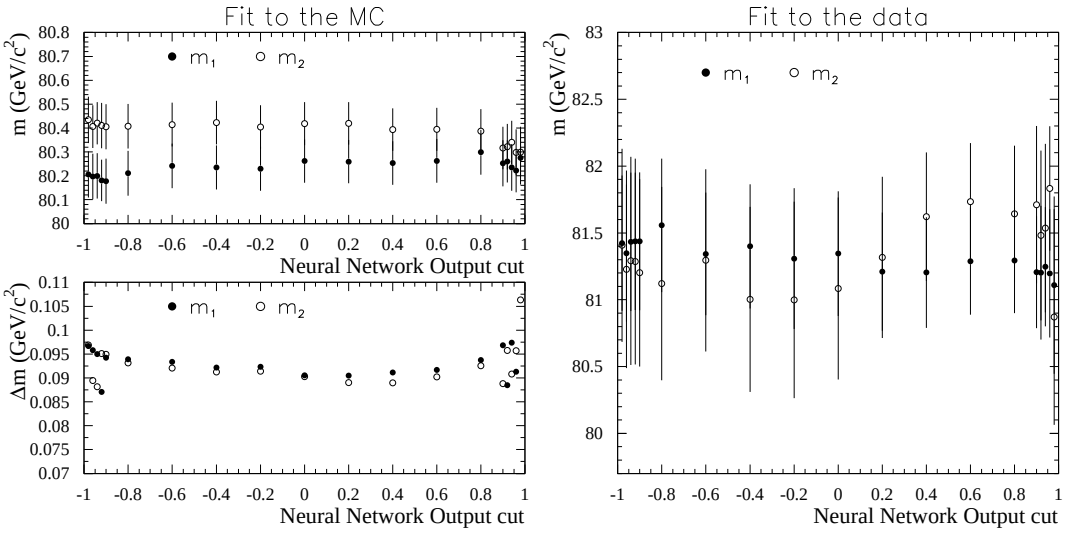

Figure 4.16: Fitted masses (top plot on the left) and expected error (bottom plot on the left) as a function of the neural network output cut for a sample of $500\,\mathrm{pb}^{-1}$ Monte Carlo events. On the right, fitted masses as a function of the neural network output cut for the selected data events.

The good agreement of the neural network output distribution between data and Monte Carlo is shown in figure 4.17. The MC histograms are normalized to the integrated luminosity of the data.

The stability of the result as a function of the mass range used for the fit is also

checked, using the data and the same Monte Carlo samples as before. Changing the lower limit of the acceptance window and keeping the higher limit fixed at 86 GeV/c^2, no significant mass range dependence on the fit result or on the expected error is observed, and the agreement between data and Monte Carlo is good (see figure 4.18).

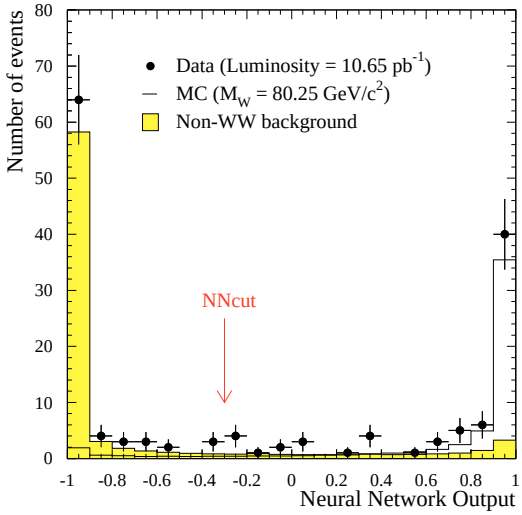

Figure 4.17: Comparison of the neural network output distribution for data and Monte Carlo.

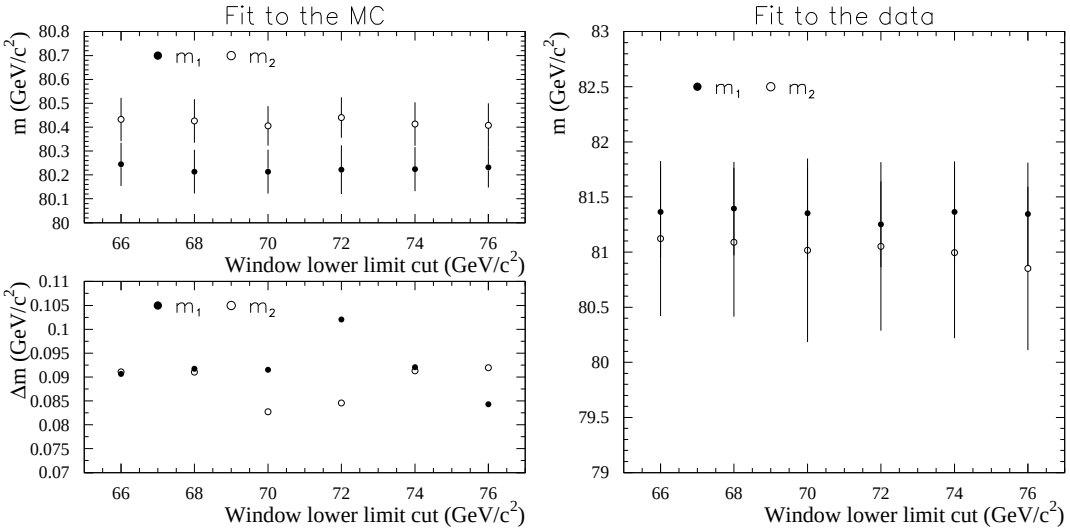

Figure 4.18: Fitted masses (top plot on the left) and expected error (bottom plot on the left) as a function of the acceptance window lower limit for a sample of 500 pb^{-1} Monte Carlo events. On the right, fitted masses as a function of the acceptance window lower limit for the selected data events.

4.8.2 Mass measurement using a Breit-Wigner fit

As a cross-check of the reweighting method, a simple relativistic Breit-Wigner function (eq. (4.4)) is fitted to the observed invariant mass distributions. In this method, the distortions described in section 4.5 introduce a bias in the fitted mass which has to be corrected for. This bias is found to be a linear function of the true input mass and is determined by fitting a straight line to the fitted mass versus the true mass, using the seven Monte Carlo samples generated with different M_{W} values (a calibration curve).

Taking the Monte Carlo generated with $M_{\mathrm{W}} = 80.25\,\mathrm{GeV}/c^2$ as the reference Monte Carlo, the fit results to the 65 selected data events are:

$$\begin{aligned} m_1 &= 81.45 \pm 0.33\,\mathrm{GeV}/c^2 \\ m_2 &= 81.32 \pm 0.35\,\mathrm{GeV}/c^2. \end{aligned}$$

The expected error for a sample of the size of the data is $0.45\,\mathrm{GeV}/c^2$ (before calibration) and the correlation between the two mass estimators is $(47.1 \pm 4.2\%)$.

Calibration curves to correct the fitted value and the expected mass error are built using the seven mass points with 52 samples of the size of the data each. A straight line is fitted to each of these curves with the following results:

$$\begin{aligned} m_1 &= (80.682 \pm 0.024) + (0.715 \pm 0.037) \times (M_{\mathrm{W}}^{true} - 80.25) \ \ (\mathrm{GeV/c^2}) \\ m_2 &= (80.689 \pm 0.022) + (0.745 \pm 0.034) \times (M_{\mathrm{W}}^{true} - 80.25) \ \ (\mathrm{GeV/c^2}). \end{aligned}$$

$m = (80.68 \pm 0.02) + (0.73 \pm 0.04) \times (m_{\mathrm{W}}^{true} - 80.25)$ $(\mathrm{GeV/c^2})$ is taken as calibration curve for both masses. After calibration, the expected error for the masses is $0.62\,\mathrm{GeV}/c^2$ and the corrected values for the masses are:

$$\begin{aligned} m_1 &= 81.30 \pm 0.62\ \mathrm{GeV}/c^2 \\ m_2 &= 81.14 \pm 0.62\ \mathrm{GeV}/c^2, \end{aligned}$$

which combined with the expected correlation (47.1%) gives a final result for the W mass of:

$$M_{\mathrm{W}} = 81.22 \pm 0.53\ \mathrm{GeV}/c^2,$$

in good agreement with the result obtained with the reweighting technique (see eq. (4.18)).

4.9 Systematic uncertainties

4.9.1 Monte Carlo fragmentation parameters

The main Monte Carlo fragmentation parameters in JETSET ($\Lambda, M_{min}, \sigma, B$ and baryon production) [6] are varied independently to extreme values, typically four standard deviations from their measured values [103]. The effect of these variations on the fitted mass is $\Delta M_{\mathrm{W}} = 10\,\mathrm{MeV}/c^2$ [104] and is quoted as systematic error due to the uncertainty on the Monte Carlo fragmentation parameters.

4.9.2 Diagrams in Monte Carlo reference

The matrix element used in this analysis corresponds to the CC03 diagrams (figure 2.1) instead of the complete matrix element which corresponds to all possible diagrams producing four fermions in the final state. The effect of this approximation is studied by comparing the weights derived from the CC03 matrix element with those derived from the complete matrix element as given by EXCALIBUR. The contribution of the non-CC03 diagrams after the event selection is negligible. Using the four-fermion matrix element to weight the Monte Carlo events, the fitted mass from the data differs only $3\,\mathrm{MeV}/c^2$ from the original one [7].

4.9.3 Selection efficiency

The selection efficiency is varied by $\pm 2\sigma$ of their statistical uncertainty, where $\sigma = 0.20\%$ (see table 4.2). In addition, the mass dependence of the selection efficiency (assumed to be independent on the W mass in this analysis) is studied over a $2\,\mathrm{GeV}/c^2$ mass range using the seven Monte Carlo samples with different M_{W} values, where a maximal difference of $1.7 \pm 0.9\%$ is observed for the selection efficiency. A linear dependence as a function of mass is implemented in the fit with

[6] Λ is the QCD scale parameter for the parton-shower, M_{min} is the infrared cut-off to stop the parton-shower, σ is the Gaussian width of the transverse momenta of the generated quarks, and B is the fragmentation parameter of light hadrons.

[7] Since the use of the four-fermion matrix element implies an increase of two orders of magnitude in the CPU time needed to perform the fit, the result obtained using only CC03 diagrams is kept and a systematic uncertainty due to this approximation is quoted.

the slope obtained from the above studies. Both variations have a negligible effect on the fitted results, hence giving no systematic uncertainty due to the selection efficiency.

4.9.4 Detector calibration

Some studies [105] indicate that there are differences between data and Monte Carlo in the global energy calibrations of the electromagnetic (ECAL) and hadronic (HCAL) calorimeters of up to 1.5% and 4% respectively. The effect of these discrepancies is estimated by globally rescaling the ECAL energy by $\pm 1.5\%$ and the HCAL energy by $\pm 4\%$ at the event reconstruction level (by recomputing the energy-flow objects) in the data. The fit is redone for all the cases (ECAL $+1.5\%$, ECAL -1.5%, HCAL $+4\%$, HCAL -4%). Using the maximum W mass deviation in both cases, the ECAL ($+53\,\mathrm{MeV}/c^2$) and HCAL ($+18\,\mathrm{MeV}/c^2$) errors are combined in quadrature to give a final uncertainty of $\Delta M_{\mathrm{W}} = 56\,\mathrm{MeV}/c^2$.

4.9.5 Jet corrections in the kinematical fit

Using the expression (4.1) described in section 4.3, the measured jet momenta ($|\vec{p_j^m}|$) are modified to allow global momentum rescalings and shifts in θ and ϕ. Since the reconstruction is not perfect because of detector effects, the expected values and resolutions of these parameters, computed from Monte Carlo, depend on both the jet energy and polar angle. However, in studies of two-jet decays of the Z^0 [106], the jet energy scale corrections differ for data and Monte Carlo by up to 30% in the region $|\cos\theta_j| \geq 0.95$, where θ_j is the angle between the jet direction and the beam axis.

To have an estimate of these effects, the correction factors, applied to the jet energies and angles, are changed by 30% of the difference of their expected values in a correlated way, and used to fit the data. The maximum variation between fitted masses is taken as systematic uncertainty: $\Delta M_{\mathrm{W}} = 40\,\mathrm{MeV}/c^2$.

4.9.6 W boson width variation

The value of the W mass obtained from the fit is studied as a function of the W width. The width is varied around its central value by the known experimental error $\pm\sigma = 0.07\,\mathrm{GeV}$ [107]. The difference in the fitted mass is at most $10\,\mathrm{MeV}/c^2$ and is taken as systematic uncertainty.

4.9.7 Initial state radiation

KORALW, the main event generator used in these studies, features QED initial state radiation up to $\mathcal{O}(\alpha^2 L^2)$, i.e. up to second order in the leading-log approximation, in the YFS style [108]. The effect of the missing terms on the W mass measurement is studied at generator level in ref. [52] by degrading KORALW to $\mathcal{O}(\alpha^1 L^1)$ and checking the size of the pure $\mathcal{O}(\alpha^2 L^2)$ correction. A systematic effect on the W mass coming from the missing higher-order terms of $15\,\mathrm{MeV}/c^2$ is quoted.

However, some checks are performed by using two different styles of soft photon exponentiation, YFS [108] and GKF [31]. A correction to the weight of eq. (4.6) is applied per event when degrading the flux function for ISR given in the YFS style from $\mathcal{O}(\alpha^2 L^2)$ to $\mathcal{O}(\alpha^1 L^1)$, and the data is fitted with the new weight. Also, another check is performed when comparing GKF to YFS in $\mathcal{O}(\alpha^2 L^2)$ in the same way. The differences observed in the fitted masses when applying these new corrections are smaller than $15\,\mathrm{MeV}/c^2$, which is taken as a conservative systematic error from initial state radiation.

4.9.8 LEP energy

The relative uncertainty on the LEP energy translates into the same relative uncertainty on the fitted mass, since the beam energy is directly used in the kinematical fit (4C + Rescaling):

$$\Delta M_{\mathrm{W}} = M_{\mathrm{W}} \frac{\Delta E_b}{E_b}. \tag{4.19}$$

For the quoted LEP beam energy uncertainty of $\Delta E_b = 30\,\mathrm{MeV}$ [65], a systematic uncertainty of $\Delta M_{\mathrm{W}} \sim 30\,\mathrm{MeV}/c^2$ is assigned.

4.9.9 Finite reference Monte Carlo statistics

Having a finite number of Monte Carlo events at the reference mass and using them in the reweighting technique contributes to a systematic uncertainty in the W mass measurement. The procedure used to study this effect consists of dividing the reference sample (signal and background) into smaller samples (10, 20, 30, 40 or 50 samples) of equal size. Each of these samples are then fitted to the same data. The RMS of the fitted masses scales as the square root of the number of samples (N_S) that the reference is divided into:

$$\mathrm{RMS} = \Delta M_{\mathrm{W}} \cdot \sqrt{N_S}. \tag{4.20}$$

Using this method, the systematic error coming from Monte Carlo statistics is estimated to be $\Delta M_{\mathrm{W}} = 30\,\mathrm{MeV}/c^2$.

4.9.10 Background contamination

The expected background remaining after the selection is about 20% of the sample. The small size of the data sample does not allow a detailed comparison of its properties (background shape and normalization) with the ones predicted by the Monte Carlo samples used. To overcome this problem, a technique using Z^0 peak data is developed to evaluate the systematic uncertainty coming from the background estimation [109]. High statistics Z^0 data taken in 1994 are compared to $\mathrm{q\bar{q}}(\gamma)$ Monte Carlo events to evaluate the effect of any discrepancy in the background shape and normalization.

Background shape

A cut-based selection similar to the preselection of this analysis (making cuts on total visible energy, missing momentum, number of energy-flow objects, number of charged tracks, etc.), but scaled down according to the ratio of beam energies (91.2/172), are applied to both Z^0 peak data and $\mathrm{q\bar{q}}(\gamma)$ Monte Carlo simulated events. Figure 4.19 shows the discrepancies between data and Monte Carlo in total energy (TotE), number of energy-flow objects (NEFLW) and number of charged tracks (NCHA).

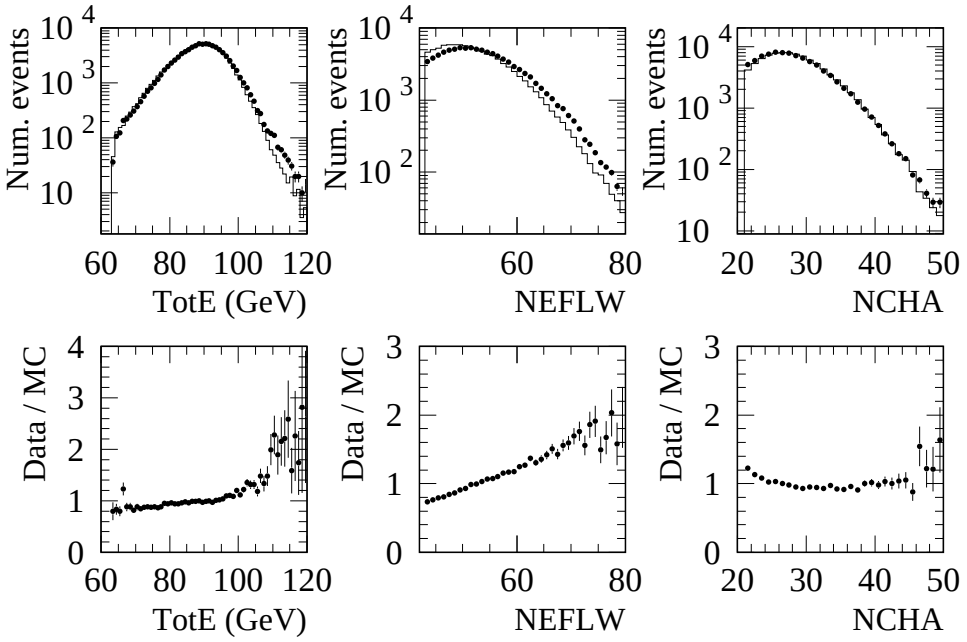

Figure 4.19: Top plots: total energy (TotE), number of energy-flow objects (NEFLW) and number of charged track (NCHA) distributions for 1994 data (points) and $q\bar{q}(\gamma)$ Monte Carlo (histogram). Bottom plots: ratio of data to Monte Carlo.

The observed disagreements at LEP1 energies are applied as correction factors to the background probability density function in the reweighting method. The resulting observed shifts in the fitted W mass are then evaluated, and the largest mass shift is taken as systematic uncertainty due to the deficient modelling of the background. The systematic uncertainty is found to be $\Delta M_{\mathrm{W}} \sim 20\,\mathrm{MeV}/c^2$.

Background normalization

The uncertainty in the background normalization is estimated by comparing the effect in the fit of the W mass when taking into account the difference between the number of data and the expected number of Monte Carlo events ($< 10\%$). The effect is negligible.

4.9.11 Colour reconnection effect

In hadronic events, the possible existence of colour reconnection (CR) effects between the two W's is pointed out as a source of systematic error on the W mass determination [110, 41, 47] some of which quote large uncertainties. However, the size of the effect is likely to be sensitive to the topology of the selected events and to the actual procedure used to extract the W mass.

The colour reconnection effect is studied using two Monte Carlo samples generated with `EXCALIBUR`, one with a colour reconnection implementation, following the ansatz of ref. [41], and another one without. The four-quark events in both samples are the same at the parton level. The selected events from both Monte Carlo samples are used as data, and the four-fermion `KORALW` Monte Carlo sample with $M_{\mathrm{W}} = 80.25\,\mathrm{GeV}/c^2$ is used as a reference to fit the W mass.

The difference when fitting the common selected events ($\sim$3200 events) of the two `EXCALIBUR` Monte Carlo's (the presence of colour reconnection slightly affects the event selection) is shown in table 4.4.

	M_{W} with C.R.	M_{W} without C.R.	$M_{\mathrm{W}}^{C} - M_{\mathrm{W}}^{NC}$
m_1 (GeV/c^2)	80.266	80.295	-0.029
m_2 (GeV/c^2)	80.273	80.261	$+0.012$

Table 4.4: Fitted W mass with and without colour reconnection and mass differences.

In order to estimate the statistical error on the mass difference, the selected events are divided into 30 subsamples (consistent results are obtained when subdividing into different number of subsamples) and the scaled RMS of the distribution of difference of estimators (following eq. (4.20)) is found to be: $\frac{\mathrm{RMS}}{\sqrt{30}} = 50\,\mathrm{MeV}/c^2$. A systematic uncertainty of $\Delta M_{\mathrm{W}} = -20 \pm 50\,\mathrm{MeV}/c^2$ due to colour reconnection effects is quoted. The statistical error is taken as the systematic error.

4.9.12 Bose-Einstein effect

In order to determine the effect of the Bose-Einstein (BE) correlations on the W mass measurement, a global event weighting method described in ref. [52] and implemented in a subroutine [111] which computes a weight per each event (w_i^{BE}), is developed.

To take into account this weight, the log-likelihood function is modified to be:

$$\log(\mathcal{L}(M_{\mathrm{W}})) = \sum_{i=1}^{N} w_i \cdot \log \mathcal{P}_i, \tag{4.21}$$

where $w_i = 1/w_i^{BE}$ is the reciprocal of the BE weight and $\mathcal{P}_i$ is the probability density function for the ith event as described in eq. (4.7).

A sample of $\sim$7000 `KORALW` selected events are fitted with (eq. (4.21)) and without (eq. (4.12)) Bose-Einstein effect. The results obtained are shown in table 4.5.

	M_{W} with BE	M_{W} without BE	$M_{\mathrm{W}}^{BE} - M_{\mathrm{W}}^{NBE}$
m_1 (GeV/c^2)	80.228	80.203	+0.025
m_2 (GeV/c^2)	80.325	80.297	+0.028

Table 4.5: Fitted W mass with and without BE effect and mass differences.

Similarly as for the colour reconnection systematic, the selected sample is divided into 50 subsamples in order to estimate the statistical error on the mass difference. The value obtained is: 40 MeV/c^2. A systematic uncertainty of $+26 \pm 40$ MeV/c^2 is quoted. The largest error, the statistical, is taken as systematic error coming from Bose-Einstein effect: $\Delta M_{\mathrm{W}} = 40$ MeV/c^2.

Systematics summary

The different sources of systematic errors investigated in this analysis are summarized in table 4.6. The total systematic error is computed adding in quadrature all different sources.

Source	ΔM_{W} (MeV/c^2)
Correlated errors	
MC fragmentation	10
Reference MC diagrams	3
Detector calibration	56
Jet corrections	40
W width	10
Initial state radiation	15
LEP energy	30
Uncorrelated errors	
Reference MC statistics	30
Background contamination	20
Colour reconnection effect	50
Bose-Einstein effect	40
Total	107

Table 4.6: Summary of systematic errors of the 172 GeV analysis.

4.10 Conclusions

A method to extract the W mass from W pair events by reweighting the Monte Carlo is proposed. The method is based on the direct comparison of the data mass distributions with those from Monte Carlo reweighted events, thus providing the correct parameter to be identified with the W mass with no need of calibration.

Fully hadronic decays are selected by means of neural network techniques with high efficiency and low background contamination. The events are forced into four jets and two invariant masses, one per di-jet, are reconstructed. A four-constraint plus rescaling fit is applied to improve the mass resolution. After choosing a jet pairing, the mass distributions are compared with those from reweighted Monte Carlo events, and the value of the W mass is extracted in a log-likelihood fit.

With 10.65 pb^{-1} collected by ALEPH in November 1996 and using only fully hadronic events, the W mass is measured to be [112]:

$$81.30 \pm 0.47(\mathrm{stat}) \pm 0.08(\mathrm{syst}) \pm 0.07(\mathrm{BE/CR}) \pm 0.03(\mathrm{LEP})\ \mathrm{GeV}/c^2. \tag{4.22}$$

The statistical error quoted corresponds to the expected error from many Monte Carlo experiments of the same size of the data. The quoted theoretical error (BE/CR) is taken from Bose-Einstein and Colour Reconnection systematics added in quadrature. BE/CR and LEP systematic uncertainties are quoted separately from the other experimental systematic errors to be able to easily combine the results with the other three LEP experiments.

Chapter 5

W mass measurement at 183 GeV

LEP reached a mean centre-of-mass energy of 182.65 GeV in 1997. With an integrated luminosity of 56.81 $pb^{\perp 1}$ collected by ALEPH at this energy, a more precise measurement of the W boson mass is achieved and described in this chapter. The reweighting method, already used in the analysis of 172 GeV data, is applied to the reconstructed invariant mass distributions of the hadronic W pair data events to obtain the W mass value. An improved jet pairing and a fit to a bidimensional invariant mass distribution are some of the new features with respect to the analysis of the previous chapter. The improvements are discussed in detail. More detailed studies of colour reconnection and Bose-Einstein W mass systematics are done.

The event selection followed by the jet clustering and kinematical fit are recalled briefly in sections 5.1 and 5.2. The description of the new jet pairing algorithm is done in section 5.3. The extraction of the W mass by means of a reweighting procedure and some Monte Carlo expectation studies are described in sections 5.4 and 5.5. In sections 5.6 and 5.7 the results and the systematic uncertainties are discussed. At the end, short conclusions are given.

5.1 Event selection

At 183 GeV the main source of background in the hadronic channel is still $e^+e^\perp \to q\bar{q}(\gamma)$ production, followed by the Z^0Z^0 and $e^+e^\perp \to W^+W^\perp \to qq\ell\nu$ processes.

Initially, the class 16 cuts are applied. A preselection, optimized for 183 GeV ,

is applied afterwards. It consists of the following cuts:

i. The longitudinal momentum (p_L) relative to the beam axis must satisfy: $|p_L| \leq 0.95\ (M_{vis} - M_Z)$ where M_{vis} is the reconstructed invariant mass of all observed energy-flow objects;

ii. The sphericity must be larger than 0.03;

The events are then forced into four jets using the DURHAM-P jet clustering algorithm. Further preselection cuts are applied to these jets:

iii. The value of y_{34} (y_{cut} value when a four-jet event becomes three-jet) must be larger than 0.001;

iv. The fraction of electromagnetic to total energy in each jet must be smaller than 0.95 .

The first cut mainly acts against events with a real Z^0 boson and large initial state radiation. The cut on sphericity takes into account that the global shape of W^+W^- hadronic events is more spherical than the shape of $e^+e^- \to q\bar{q}(\gamma)$ events. The last cut allows to eliminate events with an initial state radiation photon emitted within the detector acceptance.

The main selection is based on a neural network as it was in the previous analysis. The new neural network [113] is updated and optimized for 183 GeV and trained using the Monte Carlo samples generated at 183 GeV [1]. The neural network uses 19 input variables (instead of 21) [2], 15 hidden units and one output unit (19-15-1). The output ranges from minus one, assigned to background events, to plus one, assigned to signal events. Evaluating the discriminant power (shown in parenthesis) of many different input variables, the following set is chosen:

[1] The neural network is trained using 20k four-fermion KORALW W^+W^- events generated with $M_W = 80.35\,\mathrm{GeV}/c^2$, 10k $e^+e^- \to Z^0Z^0$ events and 100k $e^+e^- \to q\bar{q}(\gamma)$ events. These Monte Carlo events will not be taken in the rest of the analysis.

[2] Variables correlated to di-jet invariant masses are removed from the version used in the 172 GeV analysis, and some other variables are replaced by new ones having higher discriminant power.

Global event properties:

– Missing energy in the event; (4.4%)
– Sum of squared transverse momenta of all tracks in the second most energetic jet; (4.1%);
– Sphericity; (3.9%)
– Fox-Wolfram moment H0; (4.4%)
– Fox-Wolfram moment H2; (4.7%)
– Fox-Wolfram moment H4. (10.1%)

Heavy Flavour tagging:

– Sum of the b-tag probabilities for the four jets. (5.7%)

The following jet related variables are determined from kinematically fitted jet momenta using the `MATHKINE` package (described in the previous chapter) and this leads to an improvement in the discrimination power of the network.

Properties of Jets:

– Number of good tracks in the most energetic jet; (6.1%)
– Largest energy fraction carried by one energy-flow object in the most energetic jet; (3.7%)
– Largest energy fraction carried by one energy-flow object in the second most energetic jet; (4.6%)
– Largest energy fraction carried by one energy-flow object in the third most energetic jet; (4.7%)
– Sum of angles between the leading track and all the tracks in the most energetic jet; (5.5%)
– Sum of angles between the leading track and all the tracks in the second most energetic jet. (3.6%)

W^+W^- **Kinematics:**

– Total energy of the most energetic jet; (8.1%)
– Total energy of the second most energetic jet; (3.8%)
– Momentum of the least energetic jet; (5.5%)

– Sum of the cosines of the six angles between the jets; (8.7%)
– Cosine of the angle between the second and the third most energetic jets; (4.6%)
– Asymmetry between the second and the third most energetic jets [3]. (3.8%)

The agreement between data and Monte Carlo distributions of each of the 19 input variables is shown in ref. [114] and is good. A similar separation between signal and background as in the 172 GeV analysis is performed by the neural network. By requiring the neural network output larger than -0.3 , the signal events ($W^+W^\perp \rightarrow$ 4q) are selected with an efficiency of 85.2% and a purity of 80.4%.

Tables 5.1 and 5.2 give the number of Monte Carlo events surviving the class 16 cuts, events surviving the preselection requirements, and events surviving the neural network output cut for the different $W^+W^\perp$ channels and for different background processes.

5.2 Jet clustering and kinematical fit

Following the same procedure developed in the 172 GeV analysis, the `DURHAM`-PE jet clustering algorithm (where the particles are clustered by their three-momenta and then each jet four-momentum recalculated taking the particle masses into account) is used to find four jets in the event, and a 4C + Rescaling kinematical fit [4] is used to improve their invariant mass resolution. The `MATHKINE` package with a jet momenta parametrisation recalculated [115] using the `CC03 KORALW` Monte Carlo events generated at 183 GeV with $M_W = 80.35\,\mathrm{GeV}/c^2$, is again used to do the fit.

A study done with the high statistics of $Z^0 \rightarrow q\bar{q}$ events from LEP1 enables the simulation of the response of the detector to be determined for jet energies which lie in the median range of those reconstructed from $W^+W^\perp$ hadronic decays before

[3] The asymmetry between two jets with momentum $\vec{p}_1$ and $\vec{p}_2$ is defined as:

$$A_{12} = \frac{|\vec{p}_1 - \vec{p}_2|}{|\vec{p}_1 + \vec{p}_2|}.$$

[4] The LEP beam energy is recorded every 15 minutes, and more frequently if significant shifts are observed in the RF frequency of the accelerating cavities. The instantaneous values recorded nearest in time to the selected events are used to rescale the masses in this analysis.

kinematic fitting is applied. These studies show that 46 GeV jets are well simulated at all values of θ, with the largest discrepancy ($\sim$1.5%) being in the overlap region between barrel and endcaps (see figure 5.1). Average correction coefficients derived from these Monte Carlo studies are then applied to the measured jet momenta and directions before the fit. The corrections are most significant in the regions of the detector close to the beam axis. In the fitting procedure, these coefficients are allowed to vary from their average values and have been defined so that for each bin in jet energy and θ the deviations are Gaussian with minimal correlations.

The improvement due to the fit is shown in figure 5.2 where a comparison between the difference of truth and reconstructed masses without fitting and with the 4C+R fit is done.

In tables 5.1 and 5.2 the number of signal and background Monte Carlo events for which the fit has converged are shown. Most of the semileptonic $W^+W^\perp$ events that have survived the neural network cut do not fit because they are not original four-jet events and they have high missing energy due to the presence of the neutrino.

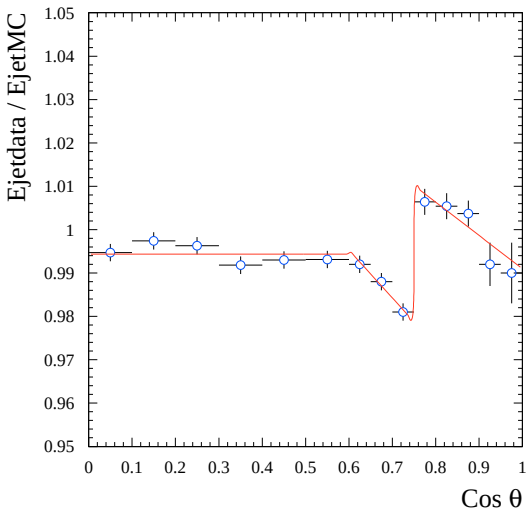

Figure 5.1: Average correction to be applied to the measured jet momenta and directions of the jets in the Monte Carlo events before the fit.

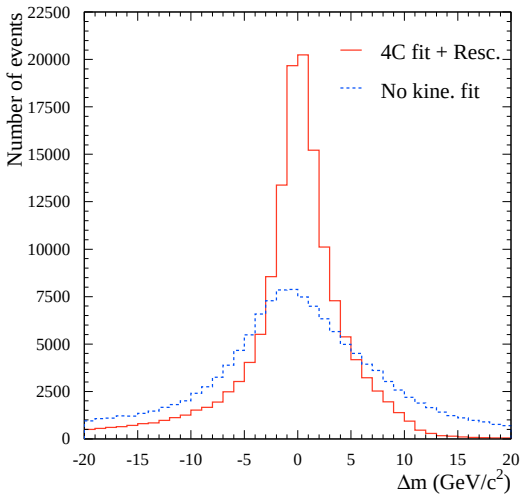

Figure 5.2: W mass resolution without applying any kinematical fit and after applying a 4C+R fit. The reconstructed masses correspond to the right di-jet pair.

5.3 Jet pairing

A pairing algorithm is used to choose one of the three possible ways into which the four jets of the selected events can be coupled. The algorithm found to be the most efficient in correctly assigning di-jet pairs to W's is a jet pairing improved from the one that was used in the 172 GeV analysis.

The *Angles* scheme algorithm (in section 4.4) is improved in the way that it uses the second best combination when the first one does not fulfil the conditions required by the algorithm. The cases where the second best combination is taken are detailed in the following.

The selected jet pair is the combination with the smallest difference between the two rescaled invariant masses unless this combination has the smallest sum of the two di-jet opening angles. In such a case, the combination with the second smallest mass difference is selected. The combination with the third smallest mass difference is never considered. Both masses for the selected combination must lie within a mass window (60,86) GeV/c^2 and at least one of the two masses must be between 74 and 86 GeV/c^2. If this condition fails then the second combination is accepted instead provided its two masses satisfy the window criteria; otherwise the event is rejected.

The two masses of the selected combinations are randomized to avoid correlations arising from ordering effects in the analysis.

The fraction of kinematically fitted signal Monte Carlo events surviving these criteria is 87.0% (see table 5.1). From the selected hadronic W pair events, 77.8% corresponds to the first selected combination while the rest corresponds to the pairs recovered from the second best combination. The invariant mass distributions of both combinations for the MC sample with $M_{\mathrm{W}} = 80.35\,\mathrm{GeV}/c^2$ are shown on the left of figure 5.3. When the first combination is chosen, it happens to be the good combination [5] 78.8% of the time, while when the second combination is chosen, only 66.8% of the time is the good one. On the right of figure 5.3 the invariant mass distributions of the good and bad combinations for the same MC sample are shown.

There is no significant W mass dependence in the final selection efficiencies applied to four-fermion `KORALW` Monte Carlo samples generated with different W mass values.

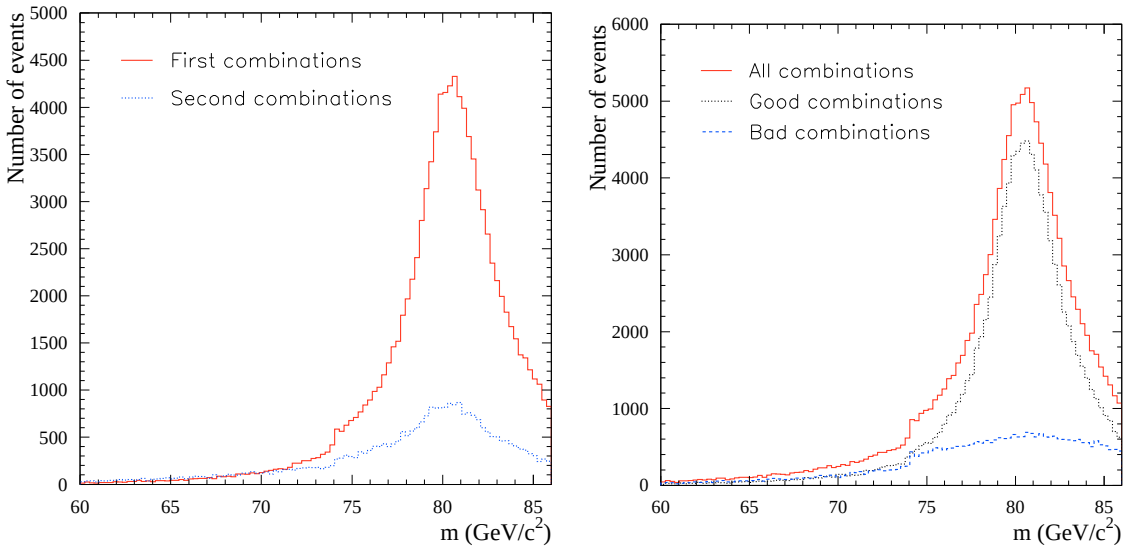

Figure 5.3: On the left, distributions of the invariant mass for the first and the second selected combinations. On the right, comparison of the invariant mass distributions for good and bad combinations.

[5] The definition of the right (good) combination is the same as in section 4.4.

The number of Monte Carlo events surviving the jet pairing criteria for $W^+W^\perp$ events and background events are shown in tables 5.1 and 5.2 respectively. A final efficiency of 74.1% and purity of 84.0% is obtained after all the selection process. The number of expected events for a data luminosity of 56.81 $pb^{\perp 1}$ is 367.5 (308.7 signal and 58.8 background events).

Process	$W^+W^\perp \to 4q$	$W^+W^\perp \to qq\ell\nu$	$W^+W^\perp \to \ell\nu\ell\nu$
Generated events	173967	164503	41530
Class 16	173416	163908	515
Preselection	165494	34362	0
N.N. cut	148238	1608	0
Convergence fit	148213	853	0
Jet Pairing	128946	641	0
Efficiency (%)	74.12 ± 0.11	0.39 ± 0.02	0
σ^{eff} (pb)	5.41	0.03	0.

Table 5.1: Number of events surviving cuts, final efficiencies and effective cross-sections for the different W decays: (4q) hadronic, ($qq\ell\nu$) semileptonic and ($\ell\nu\ell\nu$) leptonic channels. The events are four-fermion `KORALW` Monte Carlo generated with $M_W = 80.35\,GeV/c^2$.

Process	$q\bar{q}(\gamma)$	Z^0Z^0	Z^0ee
Generated events	500000	20000	60000
Class 16	449742	13988	19578
Preselection	42277	4389	451
N.N. cut	5589	1280	38
Convergence fit	5530	1275	35
Jet pairing	3882	853	29
Efficiency (%)	0.78 ± 0.01	4.27 ± 0.14	0.05 ± 0.01
σ^{eff} (pb)	0.84	0.13	0.05

Table 5.2: Number of events surviving cuts, final efficiencies and expected observable cross-sections for the most important background processes. Other processes are negligible after the selection process.

5.4 Extraction of the W mass

The Monte Carlo reweighting procedure developed in the 172 GeV analysis (section 4.5) is employed to find the value of M_{W} which best fits to the observed invariant mass distributions of the data. Selected Monte Carlo $\mathrm{W}^+\mathrm{W}^-$ events from a large four-fermion KORALW Monte Carlo sample generated with $M_{\mathrm{W}} = 80.35\,\mathrm{GeV}/c^2$ are reweighted using the weights computed by means of eq. (4.6). The small residual background of semileptonic events (0.4%) is also reweighted. The W width is set to 2.094 GeV for a mass of $80.35\,\mathrm{GeV}/c^2$ and varies in the fit with M_{W} according to eq. (2.7). Background Monte Carlo samples are included in the reference sample but not reweighted, as they do not have any information on the W mass.

In the analysis of 172 GeV data, the reweighting procedure was applied to the two rescaled invariant mass distributions independently (denoted the 1D-method). The final W mass value and statistical error were computed taking into account the expected correlation between the two fitted masses, obtained from a large number of Monte Carlo samples (section 4.6.3).

The higher statistics at 183 GeV allow a two-dimensional reweighting to be performed with the two rescaled invariant masses per event (denoted the 2D-method). The event-by-event correlations in the data are then properly accounted for and lead to an improvement in statistical precision discussed later in section 5.5.1.

A binned two-dimensional probability density function for an event having two invariant masses (m_1 and m_2) is computed similarly as with eq. (4.7)—now, two different binnings, one per signal and another one per background, are taken in order not to suffer from statistical fluctuations—:

$$\begin{aligned}\text{p.d.f.}(m_{i(k)} \le m_1 < m_{i+1(k+1)}\ ,\ m_{j(l)} \le m_2 < m_{j+1(l+1)} \mid M_{\mathrm{W}}) = \\ \rho_s(M_{\mathrm{W}})\frac{N_s^{ij}(M_{\mathrm{W}})}{\Delta m_i^s \Delta m_j^s N_s^{TOT}} + \rho_b(M_{\mathrm{W}})\frac{N_b^{kl}}{\Delta m_k^b \Delta m_l^b N_b^{TOT}},\end{aligned} \tag{5.1}$$

where $\Delta m_i^s \cdot \Delta m_j^s$ is the size of the bin (ij) for signal: $(m_{i+1} - m_i) \cdot (m_{j+1} - m_j)$; $\Delta m_k^b \cdot \Delta m_l^b$ is the size of the bin (kl) for background: $(m_{k+1} - m_k) \cdot (m_{l+1} - m_l)$; N_b^{kl} is the total number of background events found in the bin (kl); and $N_s^{ij}(M_{\mathrm{W}})$ is the weighted number of signal events from the reference Monte Carlo in the

reconstructed 2D mass bin (ij):

$$N_s^{ij}(M_{\rm W}) = \sum_{m=1}^{n_s^{ij}} w_m(M_{\rm W}), \tag{5.2}$$

where n_s^{ij} is the number of signal events from the reference Monte Carlo found in bin (ij), and $w_m(M_{\rm W})$ is the weight given by eq. (4.6). N_s^{TOT} and N_b^{TOT} are:

$$N_s^{TOT} = \sum_{i=1}^{N_{bin}^{1,s}} \sum_{j=1}^{N_{bin}^{2,s}} N_s^{ij}(M_{\rm W}); \qquad N_b^{TOT} = \sum_{k=1}^{N_{bin}^{1,b}} \sum_{l=1}^{N_{bin}^{2,b}} N_b^{kl}, \tag{5.3}$$

where $N_{bin}^{1,s}$, $N_{bin}^{2,s}$ are the number of bins in the two reconstructed mass dimensions for signal, and $N_{bin}^{1,b}$, $N_{bin}^{2,b}$ are the number of bins in the two reconstructed mass dimensions for background.

The purity is defined as in eq. (4.11), where the dependence of the cross-section on the W mass is parametrised using the `GENTLE` package:

$$\sigma_s(M_{\rm W}) = \sigma_s(M_{\rm W}^{ref}) \left(1 - 0.0071(M_{\rm W} - M_{\rm W}^{ref}) - 0.0025(M_{\rm W} - M_{\rm W}^{ref})^2\right). \tag{5.4}$$

The likelihood function to be minimized in order to obtain the W mass value which best fits to the data (which lie within the mass window of (60,86) GeV/c^2 defined by the pairing algorithm) is:

$$\mathcal{L}(M_{\rm W}) = \prod_{i=1}^{N_{evt}} \text{p.d.f.}(m_1^i, m_2^i \,|\, M_{\rm W}), \tag{5.5}$$

with N_{evt} being the number of data selected events which enter in the minimization and have m_1^i and m_2^i invariant masses.

The size of the binning needs a more careful study because the 2D probability density function suffers more from statistical fluctuations than the 1D one for a given amount of MC events. In order to avoid big fluctuations, an event having invariant mass values m_1 and m_2 (randomized) is used twice: m_1 vs m_2 and m_2 vs m_1, as if two different events were generated, for filling the 2D reference mass distribution.

5.4.1 Binning of the 2D mass distribution

In figure 5.4 the 2D mass distribution, with a fixed binning of $1\,\text{GeV}/c^2 \times 1\,\text{GeV}/c^2$, for selected Monte Carlo (with $M_{\rm W} = 80.35\,\text{GeV}/c^2$) signal events is shown.

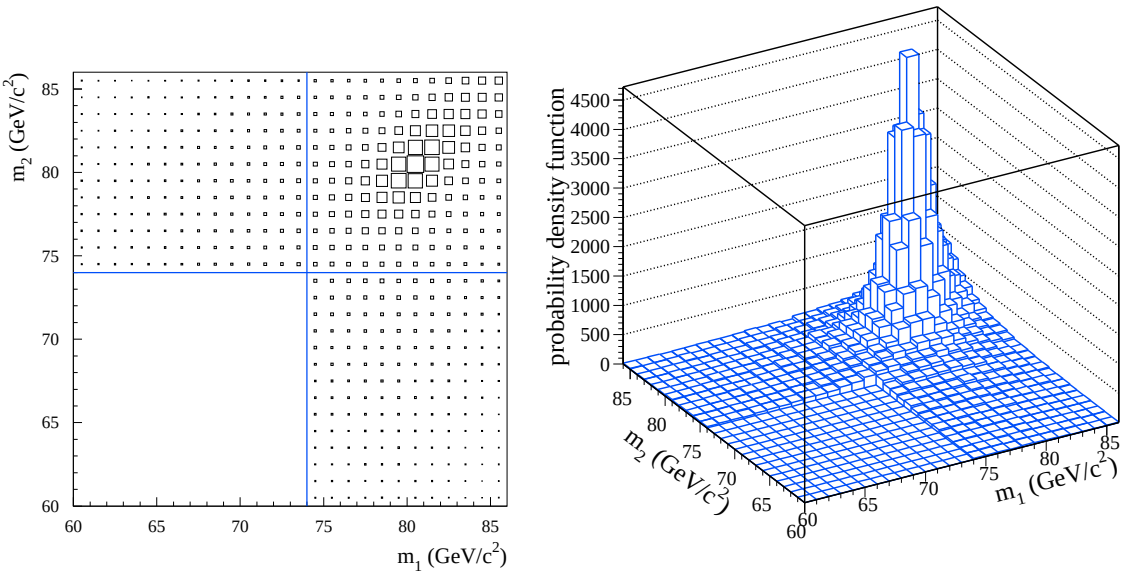

Figure 5.4: Two-dimensional reconstructed invariant mass distribution with fixed binning for four-fermion KORALW Monte Carlo selected events generated with $M_{\mathrm{W}} = 80.35\,\mathrm{GeV}/c^2$.

Due to the fluctuations from which the less populated bins can suffer, a more optimal binning is chosen. Three differently populated regions can be observed in the 2D distribution:

- $74 \leq m_1 < 86$ and $74 \leq m_2 < 86\,\mathrm{GeV}/c^2$ is the 'peak region' for both masses;
- $60 \leq m_1 < 74$ and $74 \leq m_2 < 86\,\mathrm{GeV}/c^2$ corresponds to peak for m_2 and tail for m_1: 'wing region 1';
- $74 \leq m_1 < 86$ and $60 \leq m_2 < 74\,\mathrm{GeV}/c^2$ corresponds to peak for m_1 and tail for m_2: 'wing region 2'.

By binning the 1D mass distribution for signal in each of these regions requiring the same number of events in each bin, three different variable binnings are obtained (see figure 5.5 on the left). The binning in the 2D mass distribution for signal is obtained by using these binnings in the two dimensions in the corresponding region. The number of events in each 2D mass bin is required to be above a certain minimum threshold. If this requirement is not fulfilled, the 1D mass distribution is rebinned with a bin less and the number of events in the resulting 2D mass bins rechecked. This is done iteratively until the requirement of a minimum event threshold for the 2D mass bins is fulfilled. The resulting 2D signal bins are shown on the left of figure 5.6.

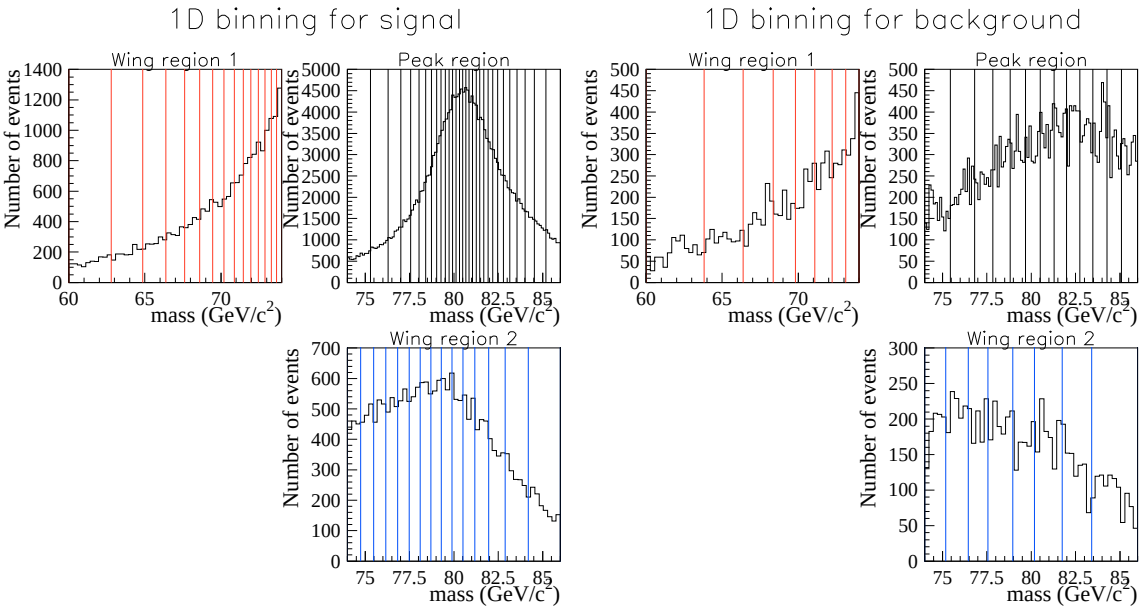

Figure 5.5: One dimensional binning to be applied into the 2D invariant mass distribution per each region: on the left, for the signal events and on the right, for background events.

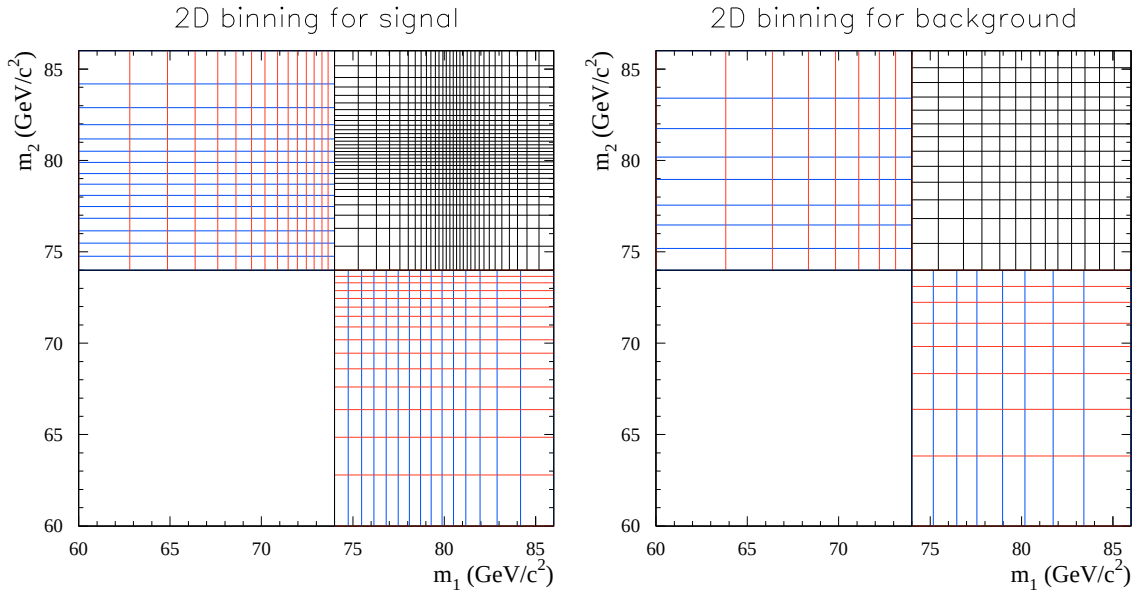

Figure 5.6: Variable binning applied to the 2D reconstructed mass distribution to compute the probability density function. On the left, the variable binning for signal, and on the right for background.

A similar procedure is applied to the background invariant mass distribution—summed $q\bar{q}(\gamma)$ and Z^0Z^0—to obtain the binning in the 2D mass distribution. Figure 5.5 on the right shows the binning for the 1D mass distribution for each region, and figure 5.6 on the right shows how the 2D mass distribution for the background is binned.

It is important to note that for the background, all regions are similarly populated as, by definition, the background does not depend on the W mass. It is not the same case for the signal that has the thinnest binning in the peak region.

MC checks of the minimum number of events in the 2D mass bins

Some Monte Carlo studies are performed in order to know the minimum number of events required in each 2D mass bin.

A study of the expected statistical error obtained from the fit of two hundred independent Monte Carlo subsamples (signal and background in the adequate proportion), each with the same number of events as the data taken, is performed depending on the minimum number of events required per 2D mass bin. The plot of the expected error for different required minimum number of events is shown on the left of figure 5.7 (the errors are correlated). The expected error is stable from a required minimum number of events per bin equal to 60.

Another check is done by looking to the linearity of the method. The slope of the calibration curve is computed as a function of this minimum number of events per bin, with the same conclusion (on the right of figure 5.7). Note that the calibration curve suffers from statistical fluctuations when less than 60 events are required per 2D mass bin.

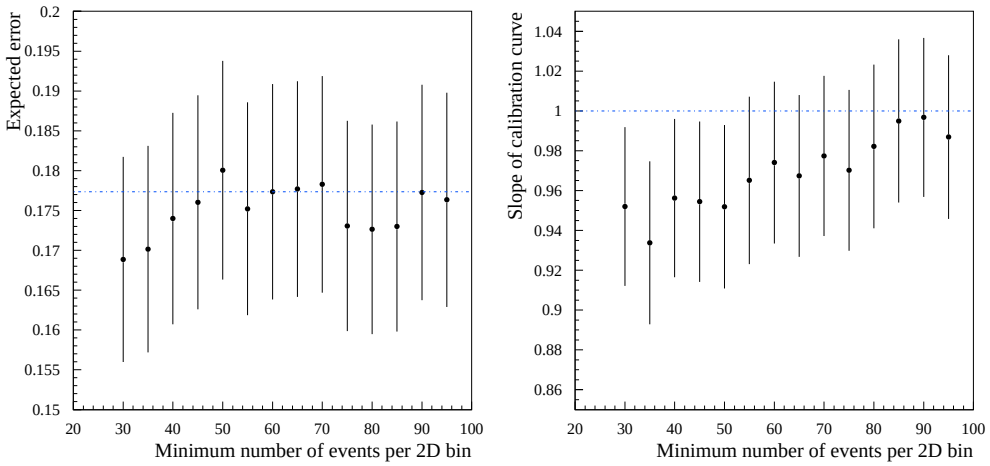

Figure 5.7: On the left, expected error distribution, and on the right, slope of the calibration curve as a function of the required minimum number of events per 2D mass bin.

5.5 Monte Carlo expectations

5.5.1 Expected error

A large number of Monte Carlo subsamples (two hundred) are used, each with the same number of events as the data, to evaluate the expected error from the RMS spread of fitted masses (shown in figure 5.8 together with their error) and the distribution of fit errors obtained. An expected error of $178 \pm 9\,\mathrm{MeV}/c^2$ is obtained, which is a $\sim$10% improvement with respect to the 1D-method ($200 \pm 9\,\mathrm{MeV}/c^2$).

5.5.2 Calibration curve

The absence of bias is checked by using five independent Monte Carlo samples generated with different M_W values (over the range $79.85 - 80.85\,\mathrm{GeV}/c^2$) with background events in the adequate proportion. Figure 5.9 shows the fitted masses as a function of the generated ones. A straight line, $m = P_1 + P_2(M_\mathrm{W}^{true} - 80.35)$, is fitted to the points. The result of the fit together with the ideal line, $m = M_\mathrm{W}^{true}$ are also shown. The fitted line is compatible with the ideal line of slope one and zero offset.

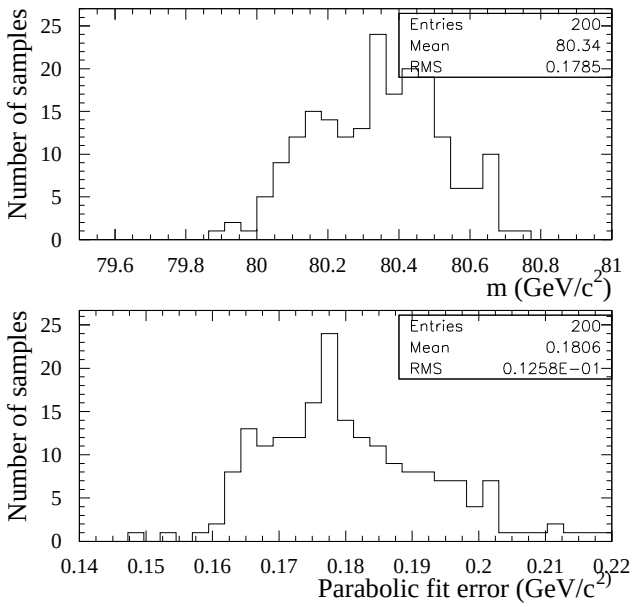

Figure 5.8: Distribution of mass estimators and fitted errors for two hundred Monte Carlo samples with the same size as the data.

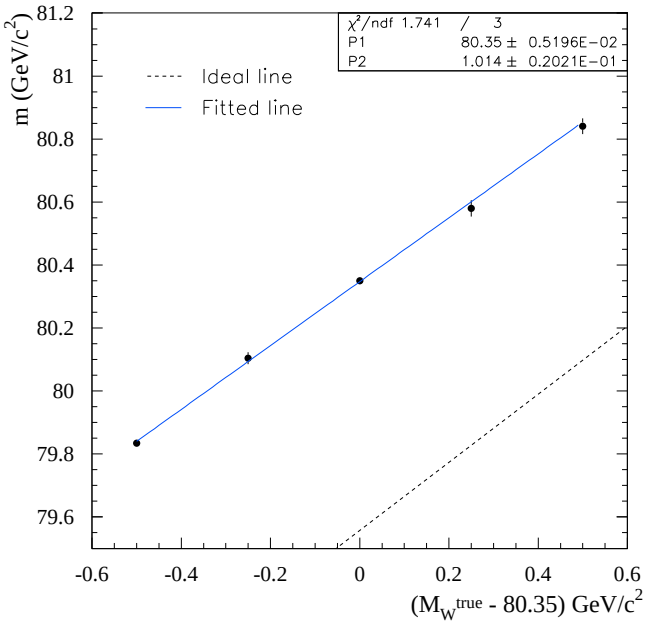

Figure 5.9: Fitted mass versus generated mass for five Monte Carlo samples of 1450 pb^{-1} each.

5.6 W mass measurement

The 2D Monte Carlo invariant mass distribution is reweighted in order to fit to the selected events of the 56.81 $\mathrm{pb}^{\perp 1}$ data integrated luminosity collected at 183 GeV.

The number of selected events of the data following the selection described in the previous sections is 384, compared with 367.5 Monte Carlo predicted events. The 2D reconstructed mass distribution for the selected data is shown in figure 5.10. The correlation between m_1 and m_2 is found to be $(24.3 \pm 4.8)\%$. When taking only the range where both masses are in the window (74,86) GeV/c^2, the correlation is $(32.7 \pm 5.1)\%$, in good agreement with the MC expectations $(22.7 \pm 0.3)\%$ and $(39.3 \pm 0.3)\%$ respectively.

The value from the fit is:

$$M_{\mathrm{W}} = 80.434^{+0.177}_{\perp 0.175}\ \mathrm{GeV}/c^2. \tag{5.6}$$

After adding 27 MeV/c^2 because the fixed-width instead of the running-width scheme is used, the W mass is measured to be:

$$M_{\mathrm{W}} = 80.461^{+0.177}_{\perp 0.175}\ \mathrm{GeV}/c^2. \tag{5.7}$$

The statistical error value obtained from the fit is in very good agreement with the expected error.

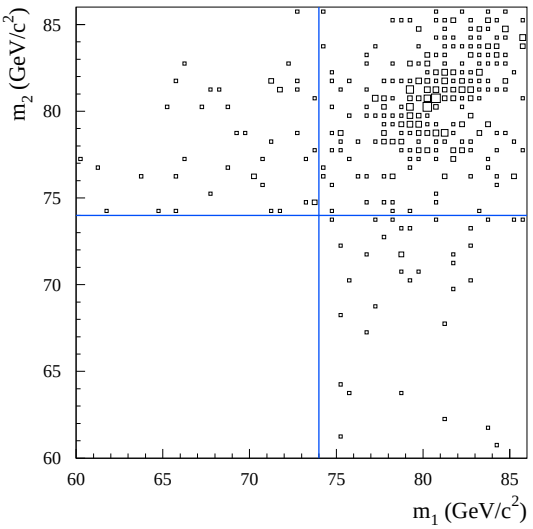

Figure 5.10: 2D invariant mass distribution for the selected data.

5.6.1 Check with the 1D-method

A check to compare the results from the 2D-method and the 1D-method is performed. The fitted m_1 and m_2 values are found to be:

$$\begin{aligned} m_1 &= 80.464^{+0.231}_{\perp 0.234}\ \mathrm{GeV}/c^2 \\ m_2 &= 80.432^{+0.259}_{\perp 0.267}\ \mathrm{GeV}/c^2 \end{aligned}$$

with an expected correlation of $(26.7 \pm 10.2)\%$. Combining both results, the W mass value obtained is:

$$m = 80.451 \pm 196\ \mathrm{GeV}/c^2.$$

Comparing the statistical error using this 1D-method, with the one using the 2D-method, an improvement of $\sim$10% using the 2D method is obtained (as expected). The W mass values obtained from both methods are compatible.

Figure 5.11 shows the 1D mass distribution (m_1 and m_2 combined) for the selected data events. The Monte Carlo distribution (signal+background) for the fitted mass, $M_{\mathrm{W}} = 80.46\ \mathrm{GeV}/c^2$ as well as the background Monte Carlo distribution itself are shown.

5.6.2 Stability checks

Some checks of the stability of the result as a function of the neural network cut output and as a function of the window mass of the pairing are performed. To study the dependence of the fitted mass with respect to the window mass, different studies are done: the dependence on the low mass of the first window (74,86), the dependence on the low mass of the second window (60,86), and the dependence on the windows high mass. Consistent results are obtained for each of these checks. Figure 5.12 on the left shows the check of the data fit and the expected error when changing the lower mass of the first window.

It is checked as well that consistent results are obtained when changing the neural network output cut (see figure 5.12 on the right) through a wide range.

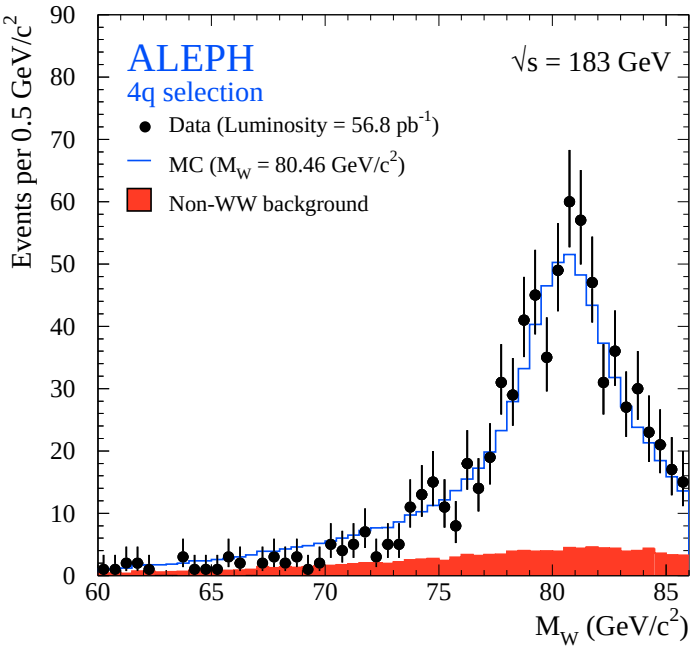

Figure 5.11: Mass distribution (m_1 and m_2) for hadronic data (points with error bars), background Monte Carlo (shaded area) and signal+background Monte Carlo for the best fit the data taken at 183 GeV (empty histogram).

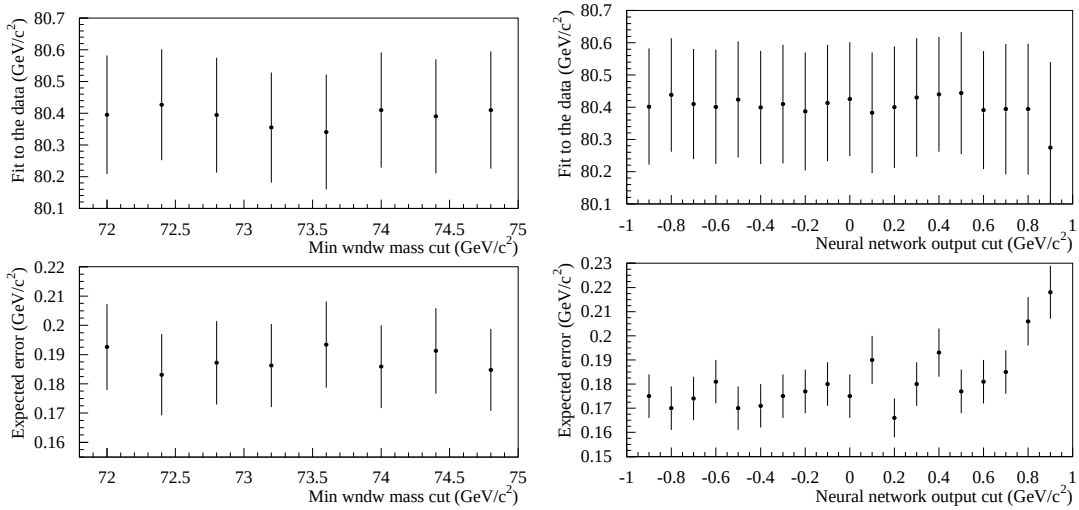

Figure 5.12: Dependence of the data fit and the expected error on the lower mass cut of the first window (on the left) and the neural network output cut (on the right).

5.7 Systematic uncertainties

5.7.1 Monte Carlo fragmentation parameters

Different Monte Carlo fragmentation packages are used to study the uncertainty coming from the MC fragmentation parameters: `JETSET` and `HERWIG`. By varying the `JETSET` fragmentation parameters (by the same amount as in the 172 GeV analysis), an effect of $\leq 10\,\mathrm{MeV}/c^2$ is obtained. However, a more significant effect is found when replacing `JETSET` by `HERWIG` to hadronise the partons in the primary reference sample. The `HERWIG` fragmentation parameters are optimized at the Z^0 using all hadronic events without flavour selection [103]. This new reference sample of 380k `HERWIG` events is then compared with the default `JETSET` sample in the reweighting procedure. Using a large number of Monte Carlo subsamples with the same size as the data taken independently from the primary reference of 380k `KORALW` events, the fitted masses obtained reweighting with each reference sample above are compared and the average shift is quoted as the systematic error. A systematic uncertainty of $35\,\mathrm{MeV}/c^2$ is found.

5.7.2 Calorimeter calibrations

The uncertainties in the global calibrations of ECAL and HCAL energy were assessed to be $\pm 0.9\%$ and $\pm 2\%$ respectively [105]. The energy-flow depositions in the data are varied in each direction by these uncertainties. The maximum shifts seen in M_{W} for each calorimeter adjustment for the common selected data sample are added in quadrature. The systematic uncertainty obtained is $\Delta M_{\mathrm{W}} = 22\,\mathrm{MeV}/c^2$.

5.7.3 Jet corrections before the kinematical fit

To estimate the systematic uncertainty coming from jet corrections before the kinematical fit, two modified parametrisations which accommodate $\pm 1\sigma$ errors in the discrepancies found in matching reconstructed Monte Carlo jets to data ($\pm 1\sigma$ of the function in figure 5.1), are evaluated. By applying these modified parametrisations to the jet energies of the data, different M_{W} values are obtained. The largest shift observed between these values and the one with no corrections, is taken as the

systematic uncertainty. Common selected data events are used to fit and an error of $\Delta M_{\mathrm{W}} = 10\,\mathrm{MeV}/c^2$ is obtained.

5.7.4 Initial state radiation

The effect of the missing terms of QED initial state radiation is estimated using a specially generated sample of `KORALW` events. These events are weighted according to the ratio of first to second order squared matrix elements: $\mathcal{O}(\alpha^1 L^1)/\mathcal{O}(\alpha^2 L^2)$, and the W mass obtained is compared to the one measured with unweighted events. A shift of $\Delta M_{\mathrm{W}} = 10\,\mathrm{MeV}/c^2$ is found and taken as systematic uncertainty.

5.7.5 LEP energy

The relative uncertainty on the LEP energy translates into the same relative uncertainty on the fitted mass (eq. (4.19)). For the quoted LEP beam energy uncertainty of $\Delta E_b = 25\,\mathrm{MeV}$ [61], a systematic uncertainty of $\Delta M_{\mathrm{W}} = 21\,\mathrm{MeV}/c^2$ is assigned.

5.7.6 Finite reference Monte Carlo statistics

The finite number of Monte Carlo events used as a reference in the reweighting method contributes a systematic uncertainty. The method used in the 172 GeV analysis subdivides the Monte Carlo reference sample into smaller samples of equal size each of which is then fitted to the same data. The RMS of the fitted masses scaled with the square root of the number of samples is taken as systematic uncertainty. However, the result relies upon an extrapolation to one sample and is less precise than another method based on a calculation of the statistical uncertainty in M_{W} evaluated from the actual number of Monte Carlo events used. Since the Monte Carlo events are used in invariant mass bins, this calculation is performed by combining the uncertainties obtained per bin, taking into account bin-by-bin efficiencies after all analysis steps and the effective number of events allowing for the reweighting procedure. The formulae used to compute this uncertainty are explained in detail in appendix B. The systematic uncertainty obtained using this method is $\Delta M_{\mathrm{W}} = 10\,\mathrm{MeV}/c^2$. This number is found to be compatible with the one computed by the previous method.

5.7.7 Background contamination

The method used to evaluate this systematic is the same as the one used for the 172 GeV data. In this case, the expected background contamination after all analysis cuts is $\sim 15\%$, and the background shape is almost flat (see figure 5.11). By re-applying the discrepancies found in the comparison between Monte Carlo and data at the Z^0 peak, to the 2D mass distribution, an uncertainty of $10\,\mathrm{MeV}/c^2$ is obtained. Both background shape and normalization uncertainties are taken into account.

5.7.8 Colour reconnection

The colour reconnection effect is studied by using Monte Carlo models based on variants of the parton evolution schemes: `JETSET`, `ARIADNE` and `HERWIG`, which have been optimized at the Z^0. The different models are explained in detail in section 2.7.1.

`JETSET` models

For the `JETSET` study, a sample of $\sim$ 45k $W^+W^- \rightarrow$ 4q is generated (with the `EXCALIBUR` Monte Carlo) and then hadronised in different ways to create:

1. a fully simulated sample with no colour reconnection;
2. three samples with different colour reconnection implementations, labelled types I, II and II' (following the description of section 2.7.1).

In type I, all events are reconnected according to the degree of string overlap. A reconnection probability, $\mathcal{P}_{reco}$, is defined as [41]:

$$\mathcal{P}_{reco} = 1. - \exp^{\perp 0.6 \cdot \phi} \tag{5.8}$$

where ϕ is the overlap between strings. Figure 5.13 shows $\mathcal{P}_{reco}$ for all generated events.

The fact that in this model all events are reconnected is considered unrealistic. Consequently, for an event to be reconnected, it is required that $\mathcal{P}_{reco} > \mathcal{P}_{cut}$, where

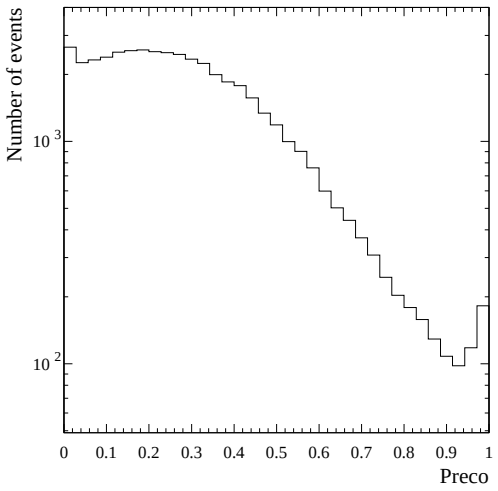

Figure 5.13: Reconnection probability values, $\mathcal{P}_{reco}$, for EXCALIBUR Monte Carlo events.

the value of $\mathcal{P}_{cut}$ is varied from 0% (all events are reconnected) to 50% (only 14% of the events are reconnected). The events that do not fulfil this requirement are left as they were originally, that is, unreconnected. The systematic uncertainty is taken as the difference between the fitted masses of the reconnected and non reconnected sample. Figure 5.14 shows the value of the systematic uncertainty when varying the value of the cut, $\mathcal{P}_{cut}$, as well as the percentage of reconnected events in the sample corresponding to each cut.

A reasonable reconnection probability for the events is $\mathcal{P}_{reco} > 0.3$ —this cut removes 60% of the sample—. Thus, the systematic quoted from this study is $\Delta M_{\mathrm{W}} = +25 \pm 21\,\mathrm{MeV}/c^2$. The RMS spread of the differences in fitted masses when doing 40 subsamples of the same size is used as the error on the uncertainty.

Model type II, where the reconnection occurs at the crossing of two vortex lines, predicts only $\sim 27\%$ reconnected events. The systematic uncertainty found with this model is $\Delta M_{\mathrm{W}} = +5 \pm 15\,\mathrm{MeV}/c^2$, smaller than the one found with model I.

Model type II', similar to type II except that the reconnection is suppressed if there is no reduction of the string length, predicts $\sim 24.4\%$ reconnected events. Computing the systematic in the same way as for model type II, the systematic uncertainty is found to be $\Delta M_{\mathrm{W}} = +17 \pm 15\,\mathrm{MeV}/c^2$.

Figure 5.15 shows the differences between the mass distributions of reconnected and non reconnected events for model types II and II'.

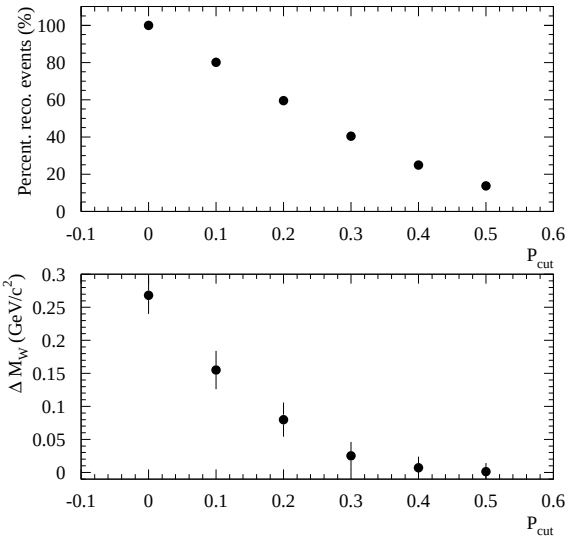

Figure 5.14: Above: percentage of reconnected events after applying the cut: $\mathcal{P}_{reco} > \mathcal{P}_{cut}$, for different values of $\mathcal{P}_{cut}$. Below: Colour reconnection systematic uncertainty using model type I when varying the value of $\mathcal{P}_{cut}$ from 0 to 0.5 .

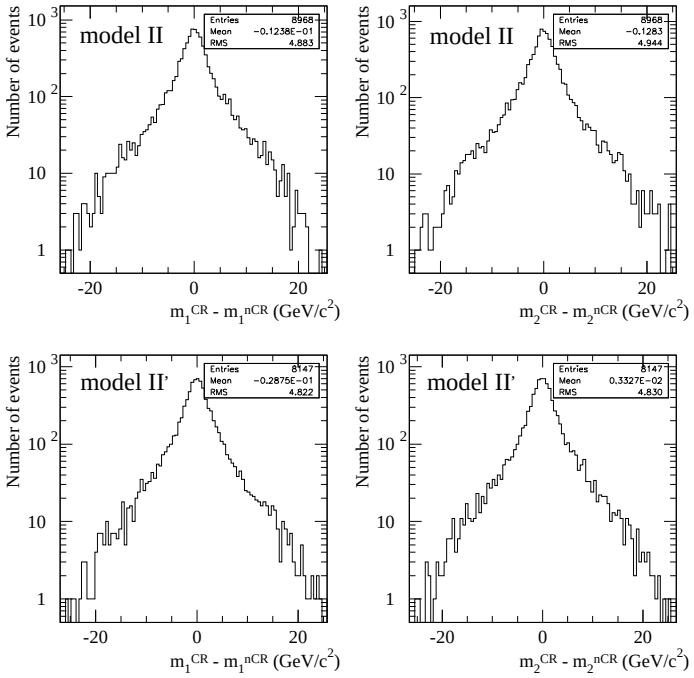

Figure 5.15: Differences between the mass distributions of reconnected and non reconnected events for model types II and II' and for both m_1 and m_2.

ARIADNE model

For the ARIADNE study, a sample of 50k hadronic events is hadronised by using the ARIADNE Monte Carlo [45]. To compare with, the same events at the parton level are hadronised with colour reconnection implemented as described in section 2.7.1. The difference between the fitted mass from the reconnected sample and the non-reconnected sample is used as systematic error. An upward shift of $27 \pm 25\,\mathrm{MeV}/c^2$ is found, where the uncertainty is computed by doing 40 subsamples of the same size.

HERWIG models

For the HERWIG models, $\mathrm{W}^+\mathrm{W}^-$ events are generated using HERWIG also for the generation of partons. Three different samples of 50k are fully simulated with the PRECO parameter (different from $\mathcal{P}_{reco}$ in eq. (5.8)), defining the level of reconnection probability, set to 0%, 11% and 60% (this last one is supposed to be unrealistic). The events are not identical at the primary parton level and, therefore, the invariant masses derived for each case are subject to statistical fluctuations. The shifts obtained relative to the 0% reconnected sample are -10 and $-31\,\mathrm{MeV}/c^2$ respectively with errors of $\pm 25\,\mathrm{MeV}/c^2$ (estimated by doing 40 samples of the same size) in each case.

The VNI model [47] has not been used to estimate a systematic error because its current implementation does not reproduce the predicted dependence of the charged event multiplicity on the minimum angle between jets from different W bosons, particle momentum distributions, and the mean value of the charged multiplicity at detector level seen in the data [116].

In conclusion, none of these models, as applied, predicts a significant effect on M_{W}. The largest uncertainty of $25\,\mathrm{MeV}/c^2$, found in the JETSET based models, is taken as the quoted systematic error.

5.7.9 Bose-Einstein effect

Two separate studies are made, using the two different approaches described in section 2.7.2.

In the first, the weighting method already used in the 172 GeV analysis is implemented using a KORALW Monte Carlo sample of 60k events generated with $M_{\mathrm{W}} = 80.35\,\mathrm{GeV}/c^2$. In figure 5.16 the distribution of weights (computed using the method described in ref. [52]) for $\mathrm{W}^+\mathrm{W}^-$ selected hadronic events is shown.

The results obtained are shown in table 5.3. A downward shift of $43 \pm 25\,\mathrm{MeV}/c^2$ is observed (the statistical error is obtained from 40 subsamples)

	M_{W} with BE	M_{W} without BE	$M_{\mathrm{W}}^{BE} - M_{\mathrm{W}}^{NBE}$
M_{W} (GeV/c^2)	80.307	80.350	−0.043

Table 5.3: Fitted W mass with and without BE weights, and the mass difference.

The second study is based on KORALW events generated with hadronisation handled by a modified version of PYTHIA, where the Bose-Einstein correlations are implemented by shifts in the momenta of identical final state particles while ensuring that energy-momentum conservation is satisfied (model BE_3 from ref. [51] is the one implemented).

In this second approach, two different samples are generated, one with correlations restricted to identical bosons within the same W, and another one where correlations between particles from different W's are also allowed. Figure 5.17 shows the difference between the mass distribution for one sample and the other.

A downward shift in M_{W} of $50 \pm 25\,\mathrm{MeV}/c^2$ is observed between the fit of both samples.

The larger shift is taken as the quoted systematic error due to Bose-Einstein correlation: $\Delta M_{\mathrm{W}} = 50\,\mathrm{MeV}/c^2$.

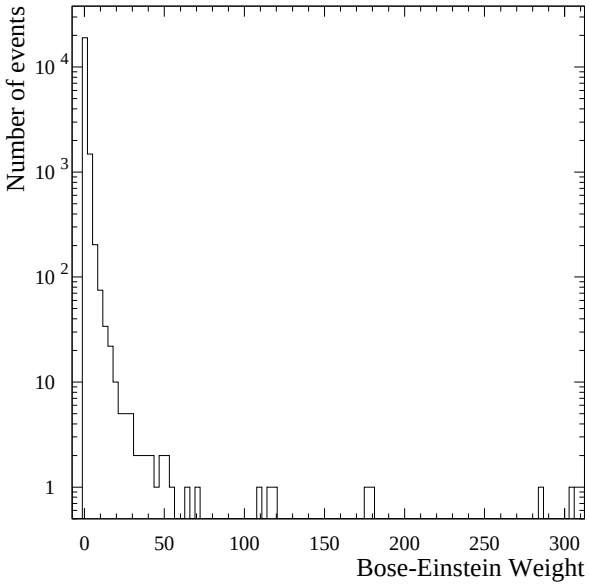

Figure 5.16: Bose-Einstein weight distribution for selected Monte Carlo hadronic events.

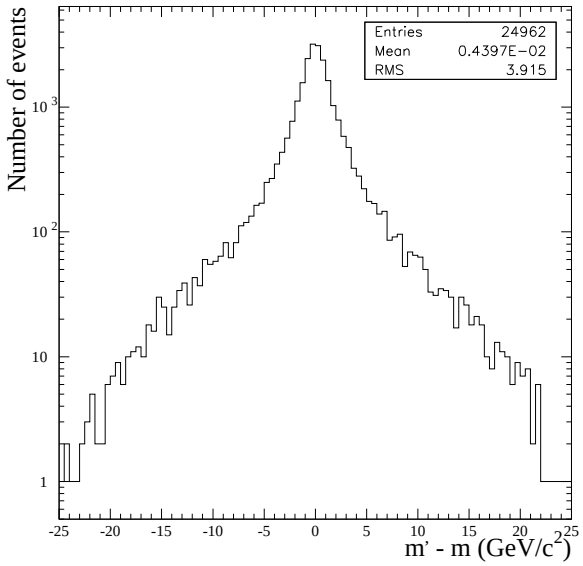

Figure 5.17: Difference between the mass distribution (m_1 and m_2) from the sample with Bose-Einstein correlations within the same W and the sample that has, in addition, correlation between the two W's.

Systematics summary

The different sources of systematic errors investigated in this analysis are summarized in table 5.4.

Source	ΔM_{W} (MeV/c^2)
Correlated errors	
MC fragmentation	35
Calorimeter calibrations	22
Jet corrections	10
Initial state radiation	10
LEP energy	21
Uncorrelated errors	
Reference MC statistics	10
Background contamination	10
Colour reconnection effect	25
Bose-Einstein effect	50
Total	75

Table 5.4: Summary of systematic errors of the 183 GeV analysis. The total systematic error is computed adding in quadrature all different sources.

5.8 Conclusions

A two-dimensional reweighting procedure performed with the two rescaled invariant masses per event is applied to 183 GeV data in the hadronic channel. Then, the event-by-event correlations in the data are properly taken into account leading to an improvement in statistical precision with respect to the one-dimensional method. Improved neural network selection and jet pairing with respect to the previous analysis are used.

With 56.81 pb^{-1} collected by ALEPH at 183 GeV, the W mass has been measured to be [117]:

$$M_{\mathrm{W}} = 80.461 \pm 0.176(\mathrm{stat}) \pm 0.046(\mathrm{syst}) \pm 0.056(\mathrm{BE/CR}) \pm 0.021(\mathrm{LEP})\ \mathrm{GeV}/c^2. \quad (5.9)$$

Chapter 6

W mass combination

The combination of the ALEPH results obtained from direct reconstruction (at 172 and 183 GeV energies) for the hadronic channel (results (4.22) and (5.9)) gives a W mass value of:

$$M_{\mathrm{W}}^{4\mathrm{q}} = 80.573 \pm 0.166(\mathrm{stat}) \pm 0.047(\mathrm{syst}) \pm 0.049(\mathrm{BE/CR}) \pm 0.022(\mathrm{LEP})\ \mathrm{GeV}/c^2. \tag{6.1}$$

When combining this result with the one obtained with the semileptonic channels ($M_{\mathrm{W}}^{\mathrm{qq}\ell\nu} = 80.334 \pm 0.170(\mathrm{stat}) \pm 0.047(\mathrm{syst}) \pm 0.022(\mathrm{LEP})\ \mathrm{GeV}/c^2$ [112] [117], which is compatible with the hadronic channel result thus indicating no interconnection effects problems), the result for the W mass measured by ALEPH using the direct reconstruction method is:

$$M_{\mathrm{W}}^{\aleph} = 80.454 \pm 0.119(\mathrm{stat}) \pm 0.045(\mathrm{syst}) \pm 0.024(\mathrm{BE/CR}) \pm 0.022(\mathrm{LEP})\ \mathrm{GeV}/c^2. \tag{6.2}$$

The combination of all direct reconstruction results of the four LEP experiments (statistical and systematic errors added in quadrature), presented at the 29th ICHEP in Vancouver, is [37]:

$$M_{\mathrm{W}}^{\mathrm{LEP}}(172 + 183\,\mathrm{GeV}) = 80.36 \pm 0.09\,\mathrm{GeV}/c^2$$

with a χ^2 per degree of freedom of 1.07/3. The value of the W mass measured at LEP after the combination with the W mass determination from the WW cross-section at threshold [39] is:

$$M_{\mathrm{W}}^{\mathrm{LEP}}(161 + 172 + 183\,\mathrm{GeV}) = 80.37 \pm 0.09\,\mathrm{GeV}/c^2\ , \tag{6.3}$$

in very good agreement with the W mass measurement coming from the hadron colliders (see figure 6.1). The combination of both measurements gives a world average (*W.A.*) W mass value of [118]:

$$M_{\mathrm{W}}^{W.A.} = 80.39 \pm 0.06\,\mathrm{GeV}/c^2\ . \tag{6.4}$$

The combination of the $\sin^2\theta_{\mathrm{W}}$ results coming from the measurements of neutrino-nucleon experiments: CCFR [119] and NuTeV [120] (the NuTeV measurement is twice as precise as the measurement by CCFR) is:

$$\sin^2\theta_{\mathrm{W}} = 0.2255 \pm 0.0021 \tag{6.5}$$

and translates to an indirect W mass measurement [1] compatible with the world average value (see figure 6.1).

By performing a global electroweak fit using as input the Z^0 measurements from LEP/SLC ($M_{\mathrm{Z}} = 91.1867 \pm 0.0021\,\mathrm{GeV}/c^2$, etc.), the $\sin^2\theta_{\mathrm{W}}$ from νN experiments (eq. 6.5), and the m_{t} measurements from CDF and D0 ($m_{\mathrm{t}} = 173.8 \pm 5.0\,\mathrm{GeV}/c^2$) [36], the M_{W} obtained is shown in figure 6.1, compatible again with the world average value.

[1] The neutrino-nucleon (νN) scattering experiments measure the neutral-current (NC) to charged-current (CC) cross-section ratio. To reduce systematics a measure of:

$$R^- = \frac{\sigma^{\nu}_{NC} - \sigma^{\bar{\nu}}_{NC}}{\sigma^{\nu}_{CC} - \sigma^{\bar{\nu}}_{CC}}$$

is performed instead. The Paschos-Wolfenstein relation [121] relates this ratio to $\sin^2\theta_{\mathrm{W}}$ in the on-shell renormalization scheme, and is (at lowest order):

$$R^- = \frac{1}{2} - \sin^2\theta_{\mathrm{W}}$$

where:

$$\sin^2\theta_{\mathrm{W}} = 1 - \frac{M_{\mathrm{W}}^2}{M_{\mathrm{Z}}^2}. \tag{6.6}$$

The small residual dependence of $\sin^2\theta_{\mathrm{W}}$ on m_{t} and M_{H} comes from the leading terms in the electroweak radiative corrections [122]:

$$\delta\sin^2\theta_{\mathrm{W}} = -0.00142\frac{m_{\mathrm{t}}^2 - (175\,\mathrm{GeV}/c^2)^2}{(100\,\mathrm{GeV}/c^2)^2} + 0.00048\ \ln\left(\frac{M_{\mathrm{H}}}{150\,\mathrm{GeV}/c^2}\right). \tag{6.7}$$

The prediction for the Higgs mass obtained is [118]:

$$\log(M_{\mathrm{H}}/(\mathrm{GeV}/c^2)) = 1.96^{+0.33}_{\perp 0.42} \qquad M_{\mathrm{H}} = 92^{+101}_{\perp 57}\ \mathrm{GeV/c^2}$$

with a χ^2 per degree of freedom of 16.2/13. After including the direct measurements of M_{W} the fit to all data gives:

$$\log(M_{\mathrm{H}}/(\mathrm{GeV}/c^2)) = 1.92^{+0.32}_{\perp 0.41} \qquad M_{\mathrm{H}} = 84^{+91}_{\perp 51}\ \mathrm{GeV/c^2}$$

with a χ^2 per degree of freedom of 16.4/15. At present the negative result of direct Higgs searches performed at LEP2 imposes a lower bound of $M_{\mathrm{H}} > 89.8\,\mathrm{GeV}/c^2$ [7] on the Higgs mass boson. Indirect information on the mass of the Higgs boson can be extracted from the M_{H} dependence of radiative corrections to the W boson mass and the effective electroweak mixing angle ($\sin^2\theta^{lept}_{eff}$). Assuming the Standard Model to be valid, a global χ^2-fit to all available electroweak precision data yields the one-sided 95% confidence level upper limit on M_{H} of $280\,\mathrm{GeV}/c^2$ [118], not including the direct Higgs search results.

Figure 6.2 shows the check of consistency between direct and indirect W mass versus top mass measurements. The contour plots are 68% confidence levels, and the Higgs mass is varied from 90 to $1000\,\mathrm{GeV}/c^2$.

In the future, if the measurements are as precise as (as expected):

$$\begin{aligned} \delta(1/\alpha(M_{\mathrm{Z}}^2)) &= \pm 0.01 \\ \delta m_{\mathrm{t}} &= \pm 2\,\mathrm{GeV}/c^2 \\ \delta M_{\mathrm{W}} &= \pm 30\,\mathrm{MeV}/c^2, \end{aligned}$$

a factor of 2.5 improvement in relative M_{H} error would be expected [8].

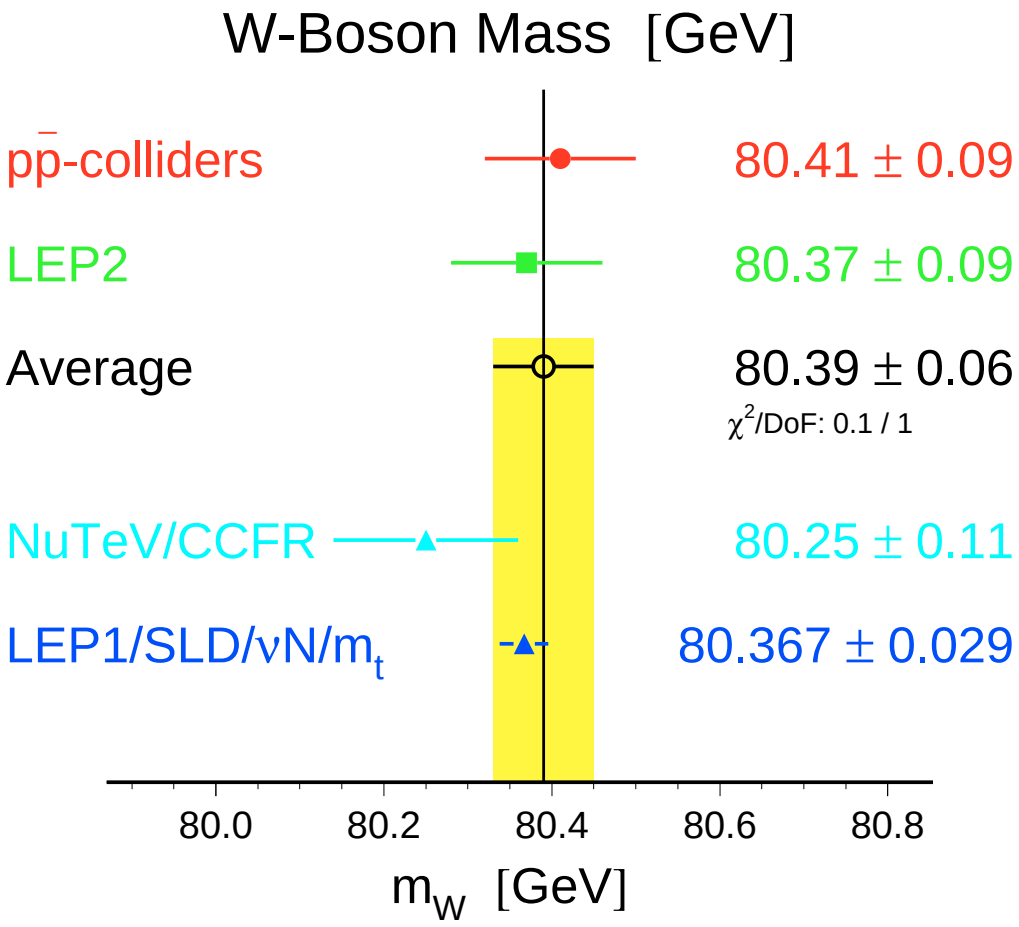

Figure 6.1: Comparison of W mass boson results between direct and indirect measurements (presented at the 29th ICHEP in Vancouver in July 1998).

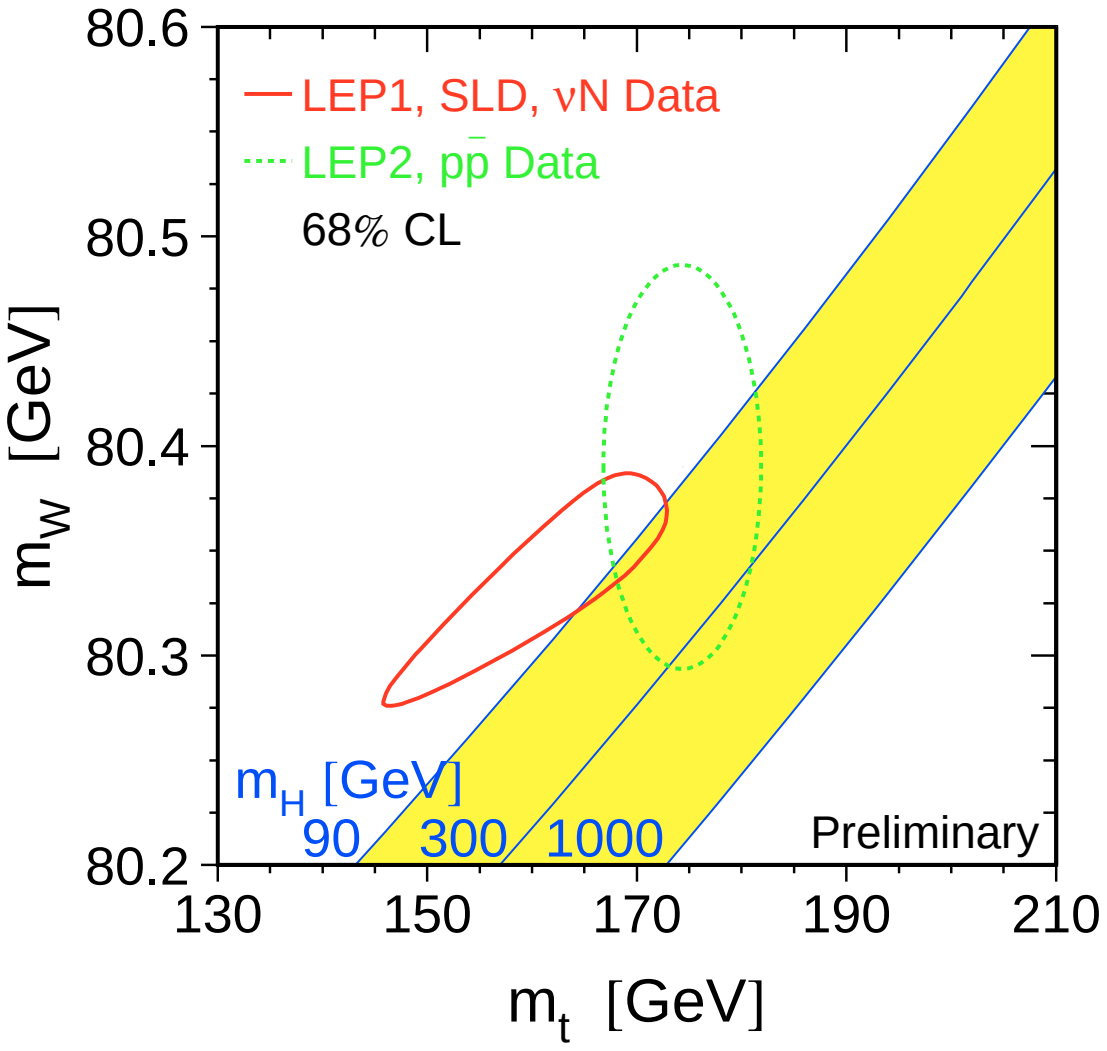

Figure 6.2: Indirect and direct measurements of the W mass and m_t (68% confidence level contour plots), compared with the Standard Model prediction for various values of M_H (from 90 to 1000 GeV/c^2).

Chapter 7

Summary and conclusions

The W mass in the fully hadronic decay channel using the data collected by ALEPH at centre-of-mass energies of 172 GeV and 183 GeV has been measured using the direct reconstruction method.

Due to the similarities between signal and background events, a feed-forward neural network—optimized for each energy—has been used for the selection. After the clustering to form jets, a kinematical fit rescaling the two invariant masses and requiring energy and momentum conservation has been applied to improve their resolution. Afterwards, a jet pairing algorithm, which takes into account the difference between the two rescaled masses and the sum of the two di-jet opening angles has been aplied. An improved jet algorithm, taking into account the second best combination, has been used in the 183 GeV analysis.

The probability density function for the data events to have a given invariant mass value has been extracted from a reference Monte Carlo, reweighted with the ratio of squared matrix elements of the reference W mass to any other W mass value. By using this technique, no calibration was needed. In the 172 GeV analysis, the two invariant mass distributions of the Monte Carlo events have been reweighted independently to fit the data events. The W mass value has been obtained by combining the two masses with the expected correlation of the two estimators.

A different procedure has been used to extract the W mass from the 183 GeV data. The reweighting technique has been applied with the two invariant masses of the Monte Carlo events at the same time. Consequently, the event-by-event correlations in the data has been properly taken into account, and a 10% improvement

with respect to the previous reweighting procedure, has been achieved.

Finally, the combination of both measurements has given a W mass value for the hadronic channel of $M_{\mathrm{W}} = 80.57 \pm 0.18\,\mathrm{GeV}/c^2$. After the combination with the W mass measurements coming from the other three LEP experiments and the hadron collider experiments, a world average W mass value of $M_{\mathrm{W}} = 80.39 \pm 0.06\,\mathrm{GeV}/c^2$ has been obtained, which has been found to be compatible with the indirect W mass measurements coming from LEP1/SLD and the νN experiments. A global fit to the available electroweak precision data has led to an upper-bound limit to the Higgs boson mass of $280\,\mathrm{GeV}/c^2$.

In the future, with all the data collected by LEP, an accuracy of $30\,\mathrm{MeV}/c^2$ in the W mass measurement is expected. If an accuracy of $2\,\mathrm{GeV}/c^2$ in the top mass measurement were achieved, a factor of 2.5 improvement in relative M_{H} error would be expected.

Appendix A

Hadronic events analysis

Some of the important aspects when dealing with hadronic events are described in this appendix, starting with the finding of jets and the definition of variables intended to provide a global view of the properties of these events. At the end, some technical aspects of kinematic fitting and some features of neural networks tools are discussed.

A.1 Jet finding

The cluster algorithms most commonly used in jet finding when analysing hadronic events are described.

Initially, each final state particle resulting from the hadronisation process, is considered to be a cluster. Using some distance measure (this will differ from one algorithm to another), the two nearest clusters are found. If their distance is smaller than some cut-off value, the two clusters are joined into one. In this new configuration with one cluster less, the two clusters that are now nearest are found and joined, and so on until all clusters are separated by a distance larger than the cut-off. This cut-off is called y_{cut} and the clusters remaining at the end are called *jets*.

Another usual way of finding jets without using a cut-off is to join the clusters till a predetermined number of jets is reached. This is the method used in both 172 and 183 GeV analyses (sections 4.2, 5.2), and the number of jets asked for is four.

The different definitions of the distance (d_{ij}^2) between clusters determine the different *cluster algorithms*:

- `DURHAM` algorithm [88]:

$$d_{ij}^2 = 2\,(\min(E_i, E_j))^2\,(1 - \cos\theta_{ij}) \tag{A.1}$$

- `JADE` algorithm [87]:

$$d_{ij}^2 = 2\,E_i E_j\,(1 - \cos\theta_{ij}) \tag{A.2}$$

- `LUCLUS` algorithm [92]:

$$d_{ij}^2 = \frac{4\,|\mathbf{p}_i|^2|\mathbf{p}_j|^2\,\sin^2(\theta_{ij}/2)}{(|\mathbf{p}_i| + |\mathbf{p}_j|)^2}, \tag{A.3}$$

where $E_i, E_j, \mathbf{p}_i, \mathbf{p}_j$ are the energy and momenta of two different clusters i and j, and θ_{ij} is the angle between them.

In order to combine the nearest clusters, different *schemes* are available for all cluster algorithms. The energy (E_{ij}) and momenta ($\mathbf{p}_{ij}$) resulting of the combination of clusters i and j for the different schemes are:

E-scheme:
$$\begin{aligned} \mathbf{p}_{ij} &= \mathbf{p}_i + \mathbf{p}_j \\ E_{ij} &= E_i + E_j \end{aligned}$$

P-scheme:
$$\begin{aligned} \mathbf{p}_{ij} &= \mathbf{p}_i + \mathbf{p}_j \\ E_{ij} &= |\mathbf{p}_{ij}| \end{aligned}$$

E_0-scheme:
$$\begin{aligned} E_{ij} &= E_i + E_j \\ \mathbf{p}_{ij} &= \frac{E_{ij}(\mathbf{p}_i + \mathbf{p}_j)}{|\mathbf{p}_i + \mathbf{p}_j|}. \end{aligned}$$

The E-scheme is Lorentz invariant while the P and E_0-schemes have to be applied in the laboratory frame.

A.2 Global event shape variables

To describe the complicated geometries encountered in hadronic events, a number of measures are introduced. These measures are intended to provide a global view

of the properties of a given event, wherein the full information content of the event is condensed into one or a few numbers.

These quantities are required to be *infrared* and *collinear* safe. Infrared safe means that the quantity should not change abruptly if one adds one soft particle to the final state, while collinear safe means that the quantity does not change abruptly if one splits one particle in the final state into two particles sharing proportionally its momentum.

Sphericity and aplanarity

The sphericity tensor ($S^{\alpha\beta}$) is defined as:

$$S^{\alpha\beta} = \frac{\sum_i p_i^\alpha p_i^\beta}{\sum_i |\mathbf{p}_i|^2},$$

where α, β=1,2,3 correspond to the x, y and z components. By diagonalizing this tensor one may find three eigenvalues $\lambda_1 \geq \lambda_2 \geq \lambda_3$, with $\lambda_1 + \lambda_2 + \lambda_3 = 1$. The *sphericity* ($S$) of the event is then defined as:

$$S = \frac{3}{2}(\lambda_2 + \lambda_3) \tag{A.4}$$

so that $0 \leq S \leq 1$. Sphericity is essentially a measure of the summed transverse momenta with respect to the event axis ($\mathbf{p}_\perp^2$). A di-jet event corresponds to $S \approx 0$ while an isotropic event to $S \approx 1$.

The sphericity tensor is quadratic in particle momenta. This means that the sphericity value is changed if one particle is split up into two collinear ones which share the original momentum. Thus sphericity is not a collinear safe quantity but it is an infrared safe quantity.

Eigenvectors ($\mathbf{v}_i$) corresponding to the eigenvalues (λ_i) of the spheriticy tensor can be found. The $\mathbf{v}_1$ is called the sphericity axis, while the sphericity event plane is spanned by $\mathbf{v}_1$ and $\mathbf{v}_2$.

A measure of the transverse momentum component out of the event plane is called *aplanarity* (A). It is defined as:

$$A = \frac{3}{2}\lambda_3. \tag{A.5}$$

The constrained range is $0 \leq A \leq \frac{1}{2}$. A planar event has $A \approx 0$ while an isotropic one has $A \approx \frac{1}{2}$.

Thrust and oblateness

The quantity *thrust* (T) is defined as the sum of the lengths of the longitudinal momenta of the final state particles relative to the axis $\mathbf{n}$ chosen to maximize this sum:

$$T = \max_{|\mathbf{n}|=1} \frac{\sum_i |\mathbf{n} \cdot \mathbf{p}_i|}{\sum_i |\mathbf{p}_i|}, \tag{A.6}$$

where i runs over all final state particles. The allowed range is $\frac{1}{2} \leq T \leq 1$, with a di-jet event corresponding to $T \approx 1$ and an isotropic event to $T \approx \frac{1}{2}$.

In the plane perpendicular to the thrust axis, a major axis and major value (M_a) may be defined in just the same fashion as thrust, i.e.

$$M_a = \max_{|\mathbf{n}|=1, \mathbf{n}\cdot\mathbf{v}_i=0} \frac{\sum_i |\mathbf{n} \cdot \mathbf{p}_i|}{\sum_i |\mathbf{p}_i|}.$$

The minor axis is defined perpendicular to the thrust and major axis, and a minor value (M_i) is calculated just as thrust and major. *Oblateness* (O) is defined as the difference between major and minor values:

$$O = M_a - M_i. \tag{A.7}$$

The upper limit on oblateness depends on the thrust value in a not so simple way. In general $O \approx 0$ corresponds to an event symmetrical around the thrust axis and high O to a planar event.

Fox-Wolfram moments

The *Fox-Wolfram moments* ($H_l, l = 0, 1, 2, ...$) are defined by:

$$H_l = \sum_{i,j} \frac{|\mathbf{p}_i|\,|\mathbf{p}_j|}{E_{vis}^2} P_l(\cos\theta_{ij}), \tag{A.8}$$

where θ_{ij} is the opening angle between hadrons i and j and E_{vis} the total visible energy of the event. The $P_l(x)$ are the Legendre polynomials.

In the approximation that particle masses may be neglected, $H_o \equiv 1$. Usually the results are normalized to H_0, i.e. $H_{l0} = H_l/H_0$. If momentum is balanced then $H_1 \equiv 0$. Di-jet events tend to give $H_l \approx 1$ for l even and $H_l \approx 0$ for l odd.

A.3 Kinematic fitting

The constrained fit package used in the hadronic channel to improve the di-jet invariant mass resolution is called `MATHKINE` [94] and its description follows. The method is general and allows all measured quantities to vary in order to fulfil a set of constraints.

The procedure that is adopted to minimize a function subject to constraints is the use of Lagrange multipliers [123]. A function (S) is defined as:

$$S(\vec{y},\vec{\lambda}) = (\vec{y}-\vec{y_0})^\top \, \mathbf{V}^{\perp 1} \, (\vec{y}-\vec{y_0}) \; + \; 2\vec{\lambda}\cdot\vec{f}(\vec{y}), \tag{A.9}$$

where $\vec{y_0}$ is the expectation value of the fitted variables $\vec{y}$, $\mathbf{V}$ is the error matrix, $\vec{\lambda}$ are the Lagrange multipliers and $\vec{f}(\vec{y})$ is a vector containing the constraints written as functions that must vanish, i.e. $\vec{f}(\vec{y}) = \vec{0}$.

The problem of minimizing $S(\vec{y},\vec{\lambda})$ reduces to solving simultaneously the equations:

$$\begin{aligned} \frac{\partial S}{\partial \vec{y}} &= \vec{0} \\ \frac{\partial S}{\partial \vec{\lambda}} &= \vec{0}. \end{aligned} \tag{A.10}$$

In order to construct a fast iterative procedure to find the minimum, the constraints $\vec{f}(\vec{y})$ are linearised using a first-order Taylor expansion:

$$\vec{f}(\vec{y}) \approx \vec{f}(\vec{y}^{\,(l)}) \; + \; \left.\frac{\partial \vec{f}(\vec{y})}{\partial \vec{y}}\right|_{\vec{y}=\vec{y}^{\,(l)}} \cdot (\vec{y}-\vec{y}^{\,(l)}). \tag{A.11}$$

Defining $\mathbf{B}$ as:

$$\mathbf{B} = \left.\frac{\partial \vec{f}(\vec{y})}{\partial \vec{y}}\right|_{\vec{y}=\vec{y}^{\,(l)}},$$

replacing $\vec{y}$ by $\vec{y}^{(l+1)}$, and making use of eq. (A.11), the equation (A.9) can be written as an iterative equation:

$$S(\vec{y}^{(l+1)}, \vec{\lambda}) = (\vec{y}^{(l+1)} - \vec{y_0})^\top \, \mathbf{V}^{\perp 1} \, (\vec{y}^{(l+1)} - \vec{y_0}) + 2\vec{\lambda} \cdot (\vec{f}(\vec{y}^{(l)}) + \mathbf{B} \, (\vec{y}^{(l+1)} - \vec{y}^{(l)})). \tag{A.12}$$

Substituting eq. (A.12) into equations (A.10), after some algebra the following formulae are found:

$$\begin{aligned} \mathbf{V}^{\perp 1} \, (\vec{y}^{(l+1)} - \vec{y_0}) + \mathbf{B}^\top \vec{\lambda} &= \vec{0} \\ \vec{f}(\vec{y}^{(l)}) + \mathbf{B} \, (\vec{y}^{(l+1)} - \vec{y}^{(l)}) &= \vec{0}, \end{aligned}$$

which can be written as:

$$\begin{pmatrix} \mathbf{V}^{\perp 1} & \mathbf{B}^\top \\ \mathbf{B} & \mathbf{0} \end{pmatrix} \begin{pmatrix} \vec{y}^{(l+1)} \\ \vec{\lambda} \end{pmatrix} = \begin{pmatrix} \mathbf{V}^{\perp 1} \vec{y_0} \\ -\vec{f}(\vec{y}^{(l)}) + \mathbf{B}\vec{y}^{(l)} \end{pmatrix}.$$

By inverting the first matrix a recursion formula for determining $\vec{y}^{(l+1)}$ is obtained:

$$\vec{y}^{(l+1)} = \vec{y_0} + \mathbf{V}\mathbf{B}^\top (\mathbf{B}\mathbf{V}\mathbf{B}^\top)^{\perp 1} \, (\, \mathbf{B} \, (\vec{y}^{(l)} - \vec{y_0}) - \vec{f}(\vec{y}^{(l)}) \,). \tag{A.13}$$

This recursion formula converges and minimizes $S(\vec{y}, \vec{\lambda})$ if the distribution of each parameter y_i is close to a Gaussian.

It is possible to take into account initial state radiation and Breit-Wigner mass distributions in the constrained fit by including in eq. (A.9) a function $g(x)$, which only depends on a scalar variable (x) and represents a penalty function. Following the likelihood concept, this function takes the form $-2\ln(p(x))$, where $p(x)$ is a probability distribution function connected to the variables $\vec{y}$ via constraints: $x - f(\vec{y}) = 0$ [124].

A.4 Neural Network description

Neural Networks (NN) [125] have become very useful tools for event classification and more generally, for pattern recognition problems where the number of variables considered is large. The use of neural networks has increased in high energy physics mostly to classify signal versus background events as the information carried by

many physical variables is used at the same time (multidimensional method). The multidimensional neural network technique allows to handle non-linear classification problems, which cannot be solved by using linear cuts in the variables and allows also to treat the correlations between the different variables in an optimal way.

In the case of the hadronic $W^+W^\perp$ channel selection, the neural network is used to distinguish two similar type of events: $e^+e^\perp \rightarrow W^+W^\perp \rightarrow 4q$ (signal process) and $e^+e^\perp \rightarrow q\bar{q}(\gamma)$ (background process). It is a very efficient way to improve the efficiency and the purity in the selection of signal events.

A.4.1 Description of a multilayered feed forward neural network

A multilayered feed forward neural network (MLNN) used for pattern recognition needs several layers. Each neuron of a layer (l) is directly connected with all neurons of the next layer ($l+1$) but there is no connection with the neurons of the same layer. The strength of each connection is described by a weight. A typical architecture (number of units and their arrangement) is shown in figure A.1. Each neuron (i) in

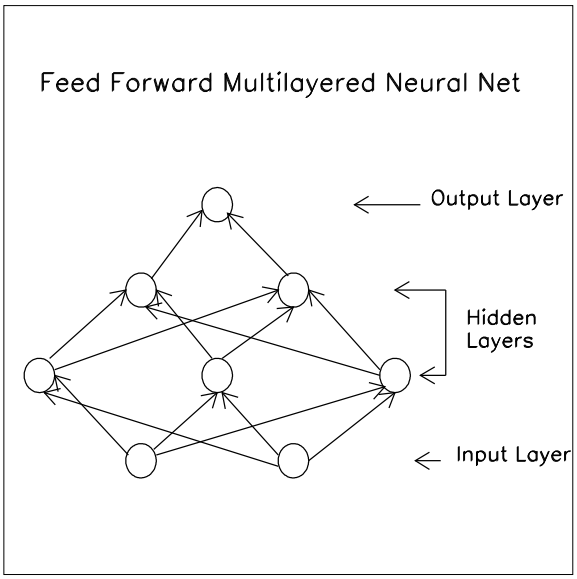

Figure A.1: Typical architecture of a multilayered feed forward neural network with two hidden layers. The information flows only in one direction and the neurons are grouped into layers.

the network will give an output (O_i), which is a non-linear function of the weighted sum of the O_j outputs of the j neurons it is connected with.

The output of a MLNN used for pattern recognition involves three steps:

1. Supervised learning: events belonging to each class are presented to the system to train it to recognize their features. The class of the event is given as input at this stage. The weights connecting neurons are determined by using the gradient descent method, explained later [126].

2. Validation step: checking the ability of the network already trained to recognize events it has never seen before. Therefore, another sample of events is presented to the network without class indication.

3. The system is finally used to perform an event by event classification on real experimental events.

The learning consists of tuning the weight values to minimize the *error function* (E) defined as:

$$E = \sum_{p} \sum_{m=1}^{N} (O_m^{(p)} - d_m^{(p)})^2, \tag{A.14}$$

where $d_m^{(p)}$ is the desired output of neuron (m) for a given event (p), N is the number of neurons in the output layer, and p runs over all the events of the training sample. The minimization of this function is done by an iterative process (gradient descent method), modifying the values of the weights in the opposite direction of the gradient function. The update of the weights between neurons i and j (w_{ij}) in a given number of iterations (n) is done following the formulae:

$$w_{ij}(n) = w_{ij}(n-1) + \Delta w_{ij}(n) \tag{A.15}$$

$$\Delta w_{ij}(n) = -\epsilon \frac{\partial E}{\partial w_{ij}} + \alpha \, \Delta w_{ij}(n-1), \tag{A.16}$$

where ϵ and α are two learning parameters (so-called learning and momentum rate respectively) and must be adapted for an efficient learning of the network. A positive weight means an excitation and a negative weight an inhibition of the neurons.

The architecture of the multilayered neural network is decided taking into account that: the number of input units must be equal to the number of the selected

discriminating variables; the number of output units is governed by the number of classes to be separated; and the number of hidden layers as well as the number of units per layer have to be optimized for the separation.

The output of the neural network can be interpreted as a measurement of the probability of an input event to belong to a certain category, signal or background in our case [127].

A.4.2 Optimization of the number of inputs

Information concerning the relative contribution of the different variables to the NN selection capability can be deduced from the weights values. In other words, connections with strong weights lead to strong triggering of the ouput neuron unit which is bound to them. This is due to the fact that the weights values are continuously modified during the learning step (following eq. (A.15)) to give the best fit of the NN output for the classes to be separated.

To handle the information carried by the weights values, the vector S_{w_k} is introduced such that [128]:

$$S_{w_k} = \sum_{i=1}^{N_{hl}} |w_{ik}|,$$

where N_{hl} is the number of neurons on the first hidden layer, and w_{ik} the weight of the connection between the input neuron k and the neuron i of the first hidden layer.

The larger S_{w_k} the stronger the role of the variable corresponding to neuron k in the separation of $W^+W^\perp \rightarrow 4q$ events from background events. This last quantity can be normalized by taking:

$$S^*_{w_k} = \frac{S_{w_k}}{\sum_{k=1}^{N_V} S_{w_k}}, \tag{A.17}$$

where N_V is the total number of variables of the input layer. This quantity ($S^*_{w_k}$) gives the *discriminant power* of each variable and can be used to take out the less discriminating ones from the set originally chosen.

Appendix B

Monte Carlo statistics systematic calculation

The systematic uncertainty on the W mass due to the Monte Carlo statistics can be computed using the fact that each bin in the invariant mass (m) distribution plot has different sensitivity. This is an analytical way to compute this systematic uncertainty instead of doing Monte Carlo subsamples of the reference and extrapolating to one sample the fit to the data.

The contribution to the error on M_{W} from each invariant mass bin (i) is:

$$\Delta M_{\mathrm{W}}^{i} = \frac{\Delta\sigma_i}{\frac{\partial\sigma_i}{\partial M_{\mathrm{W}}}}, \tag{B.1}$$

where σ_i is the differential cross-section integrated over the invariant mass bin (i):

$$\sigma_i = \int_i \frac{d\sigma}{dm}\, dm, \tag{B.2}$$

and can be estimated as:

$$\sigma_i = \frac{N_i}{\mathcal{L}\cdot\epsilon} \tag{B.3}$$

with an error of:

$$\Delta\sigma_i = \frac{\sqrt{N_i}}{\mathcal{L}\cdot\epsilon}, \tag{B.4}$$

where N_i is the number of events in the bin (i), $\mathcal{L}$ is the total integrated luminosity and ϵ is the selection efficiency.

The probability density function for an event to have an invariant mass (m), defined as:

$$\rho(m) = \frac{d\sigma/dm}{\sigma_T}; \quad \sigma_T = \int \frac{d\sigma}{dm}\, dm, \tag{B.5}$$

is approximated as:

$$\rho_i(m) = \frac{1}{N_T} \cdot \frac{N_i}{\Delta m_i}, \tag{B.6}$$

where N_T is the total number of events and Δm_i is the width of the invariant mass bin (i).

Deriving this probability in terms of M_{W} and making use of eq. (B.3), the following equation is obtained:

$$\frac{\partial \rho_i}{\partial M_{\mathrm{W}}} = \frac{1}{N_T} \cdot \frac{\partial}{\partial M_{\mathrm{W}}} \left(\frac{N_i}{\Delta m_i} \right) = \frac{1}{\sigma_T \Delta m_i} \cdot \frac{\partial \sigma_i}{\partial M_{\mathrm{W}}}, \tag{B.7}$$

where σ_T is the total cross-section.

Making use of this last equation and eq. (B.4), the contribution to the error on M_{W} per each invariant mass bin (i) is:

$$\Delta M_{\mathrm{W}}^i = \frac{1}{\Delta m_i \cdot \dfrac{\partial \rho_i}{\partial M_{\mathrm{W}}} \cdot \dfrac{N_T}{\sqrt{N_i}}}, \tag{B.8}$$

The final error in M_{W} covering the whole invariant mass distribution is:

$$(\Delta M_{\mathrm{W}}^T)^2 = \frac{1}{\displaystyle\sum_i \left(\Delta m_i \cdot \frac{\partial \rho_i}{\partial M_{\mathrm{W}}} \cdot \frac{N_T}{\sqrt{N_i}} \right)^2}, \tag{B.9}$$

where the contribution from each bin is assumed to be independent.

This equation gives the systematic uncertainty due to Monte Carlo statistics, and it is used in the analysis of 183 GeV data.

Bibliography

[1] S.L. Glashow, Nucl. Phys. **22** (1961) 579;
S. Weinberg, Phys. Rev. Lett. **19** (1967) 1264;
A. Salam, *Elementary Particle Theory*, N. Svartholm (ed.), Almqvist and Wiksell, Stockholm (1968) 367.

[2] S.L. Glashow, J. Iliopoulos and L. Maiani, Phys. Rev. **D2** (1970) 1285.

[3] G. 't Hooft, Nucl. Phys. **B33** (1971) 173.

[4] The LEP Collaborations (ALEPH, DELPHI, L3 and OPAL), The LEP Electroweak Working Group and the SLD Heavy Flavour Group, *A combination of preliminary electroweak measurements and constraints on the Standard Model*, ALEPH internal report, ALEPH 98-037 (1998).

[5] N. Cabbibo, Phys. Rev. Lett. **10** (1963) 531;
M. Kobayashi and K. Maskawa, Prog. Theor. Phys. **49** (1973) 652.

[6] Super-Kamiokande Collaboration, Contribution to the Neutrino '98 Conference, Japan, June 1998.

[7] D. Treille, *Searches at existing machines*, Contribution to the 29th ICHEP, Vancouver, Canada, July 1998;
P. McNamara, *The Search for the Standard Model Higgs Boson at LEP*, Contribution to the 29th ICHEP, Vancouver, Canada, July 1998.

[8] M.W. Grünewald, *Combined Analysis of Precision Electroweak Results*, Contribution to the 29th ICHEP, Vancouver, Canada, July 1998.

[9] J. Fujimoto *et al.*, MINAMI-TATEYA Collaboration, *GRACE User's manual, version 2.0*, KEK report 92-19 (1993) (submitted to Comput. Phys. Commun.).

[10] W. Beenakker and A. Denner, Int. J. Mod. Phys. **A9** (1994) 4837.

[11] V. Barger *et al.*, Phys. Rev. **D28** (1983) 2912;
X. Tata, M. Drees and C.S. Kim, Phys. Rev. **D37** (1988) 784;
J. Terrón, T. Álvarez and A. Leites, Nucl. Phys. **B301** (1988) 1.

[12] Particle Data Group, Eur. Phys. J. **C3** (1998) 19.

[13] A. Denner, Fortschr. Phys. **41** (1993) 307.

[14] M. Demarteau, *Electroweak measurements from the Tevatron*, Contribution to the workshop on New Directions for High Energy Physics (Snowmass 96) Snowmass, Colorado, USA, June-July 1996.

[15] Particle Data Group, Eur. Phys. J. **C3** (1998) 225 and 94.

[16] T. Muta, R. Najima and S. Wakaizumi, Mod. Phys. Lett. **A1** (1986) 203.

[17] M. Consoli and A. Sirlin, *Physics at LEP*, J. Ellis and R. Peccei (eds.), CERN 86-02 (1986) vol.1, 63;
F. Jegerlehner, *Testing the Standard Model*, M. Cvetič and P. Langacker (eds.), Proc. of the 1990 Theor. Adv. Study Inst. (World Scientific, Singapore, 1991) 476.

[18] D. Bardin, A. Leike, T. Riemann and M. Sachwitz, Phys. Lett. **B206** (1988) 539.

[19] W. Beenakker, $e^+e^\perp$ *Collisions at* 500 GeV*: The Physics Potential*, P.M. Zerwas (ed.) (DESY 92-123, Hamburg, 1992) part A, 195.

[20] U. Baur and D. Zeppenfeld, Phys. Rev. Lett. **75** (1995) 1002.

[21] M. Veltman, Physica **29** (1963) 186;
R.G. Stuart, Phys. Lett. **B262** (1991) 113;
A. Aeppli, G.J. van Oldenborgh and D. Wyler, Nucl. Phys. **B428** (1994) 126.

[22] J. Papavassiliou and A. Pilaftsis, Phys. Rev. **D53** (1996) 2128.

[23] E.N. Argyres *et al.*, Phys. Lett. **B358** (1995) 339.

[24] W. Beenakker and F.A. Berends, *Physics at LEP2*, G. Altarelli, T. Sjöstrand and F. Zwirner (eds.), CERN 96-01 (1996) vol.1, 79.

[25] J. Fleischer, F. Jegerlehner and M. Zralek, Z. Phys. **C42** (1989) 409;
K. Kolodziej and M. Zralek, Phys. Rev. **D43** (1991) 3619;
J. Fleischer, F. Jegerlehner and K. Kolodziej, Phys. Rev. **D47** (1993) 830.

[26] M. Böhm *et al.*, Nucl. Phys. **B304** (1988) 463;
W. Beenakker, F.A. Berends and T. Sack, Nucl. Phys. **B367** (1991) 287;
W. Beenakker, K. Kolodziej and T. Sack, Phys. Lett. **B258** (1991) 469.

[27] A. Sommerfeld, *Atombau und Spektrallinien*, Band 2, (Vieweg, Braunschweig, 1939);
A.D. Sakharov, JETP **18** (1948) 631.

[28] V.S. Fadin, V.A. Khoze, A.D. Martin and A. Chapovsky, Phys. Rev. **D52** (1995) 1377.

[29] V.S. Fadin, V.A. Khoze, A.D. Martin and W.J. Stirling, Phys. Lett. **B363** (1995) 112;
V.A. Khoze and T. Sjöstrand, Z. Phys. **C70** (1996) 625.

[30] V.A. Khoze and W.J. Stirling, Phys. Lett. **B356** (1995) 373.

[31] E.A. Kuraev and V.S. Fadin, Sov. J. Nucl. Phys. **41** (1985) 466.

[32] D. Bardin, M. Bilenky, A. Olchevski and T. Riemann, Phys. Lett. **B308** (1993) 403; **B357** (1995) 725(E);
D. Bardin, D. Lehner and T. Riemann, *Complete Initial State QED Corrections to Off-Shell Gauge Boson Pair Production in* $e^+e^\perp$ *Annihilation*, DESY 96-028 (1996).

[33] D. Bardin and T. Riemann, *Off shell W pair production in* $e^+e^\perp$ *annihilation: The* `CC11` *process*, DESY 95-167 (1995).

[34] J. Fleischer, F. Jegerlehner and M. Zralek, Z. Phys. **C42** (1989) 409;
F. Jegerlehner, *Radiative corrections: Results and Perspectives*, N. Dombey and F. Boudjema (eds.), NATO ASI Series, Plenum Press, New York (1990) 185.

[35] Z. Kunszt and W.J. Stirling, *Physics at LEP2*, G. Altarelli, T. Sjöstrand and F. Zwirner (eds.), CERN 96-01 (1996) vol.1, 141.

[36] R. Partridge, *Heavy Quark Production and Decay (*t *and* b *Onia)*, Contribution to the 29th ICHEP, Vancouver, Canada, July 1998.

[37] LEPEWWG/MW/98-02, *LEP WW cross-section and W mass for '98 Summer conferences*, (1998).

[38] Y.K. Kim, Contribution to the Lepton-Photon Symposium 1997, Hamburg, July-August 1997.

[39] R. Barate *et al.*, ALEPH Collaboration, Phys. Lett. **B401** (1997) 347;
P. Abreu *et al.*, DELPHI Collaboration, Phys. Lett. **B397** (1997) 158;
M. Acciarri *et al.*, L3 Collaboration, Phys. Lett. **B398** (1997) 223;
K. Ackerstaff *et al.*, OPAL Collaboration, Phys. Lett. **B389** (1996) 416.

[40] T. Sjöstrand, Comput. Phys. Commun. **82** (1994) 74.

[41] T. Sjöstrand and V.A. Khoze, Z. Phys. **C62** (1994) 281; Phys. Rev. Lett. **72** (1994) 28.

[42] F.A. Berends, R. Kleiss and R. Pittau, Comput. Phys. Commun. **85** (1995) 437.

[43] G. Marchesini and B.R. Webber, Nucl. Phys. **B310** (1988) 461;
I. Knowles, Nucl. Phys. **B310** (1988) 571;
G. Marchesini *et al.*, Comput. Phys. Commun. **67** (1992) 465.

[44] G. Gustafson, Phys. Lett. **B175** (1986) 453;
G. Gustafson and U. Pettersson, Nucl. Phys. **B306** (1988) 746.

[45] L. Lönnblad, Comput. Phys. Commun. **71** (1992) 15;
L. Lönnblad, Z. Phys. **C70** (1996) 107.

[46] K. Geiger, Comput. Phys. Commun. **104** (1997) 70.

[47] J. Ellis and K. Geiger, Phys. Rev. **D54** (1996) 1967;
Phys. Lett. **B404** (1997) 230.

[48] K. Geiger, Phys. Rev. **D54** (1996) 949.

[49] R. Hanbury-Brown and R.Q. Twiss, Nature **178** (1956) 1046;
G. Goldhaber *et al.*, Phys. Rev. **120** (1960) 300.

[50] L. Lönnblad and T. Sjöstrand, Phys. Lett. **B351** (1995) 293.

[51] L. Lönnblad and T. Sjöstrand, Eur. Phys. J. **C2** (1998) 165.

[52] S. Jadach and K. Zalewski, CERN-TH/97-029 (1997).

[53] K. Fialkowski and R. Wit, Z. Phys. **C74** (1997) 145;
K. Fialkowski and R. Wit, hep-ph/9703227 (1997).

[54] Q.H. Zhang *et al.*, Phys. Lett. **B407** (1997) 33.

[55] B. Andersson and M. Ringnér, Nucl. Phys. **B513** (1998) 627.

[56] D. Decamp *et al.*, ALEPH Collaboration, Nucl. Inst. and Meth. **A294** (1990) 121.

[57] P. Aarnio *et al.*, DELPHI Collaboration, Nucl. Inst. and Meth. **A303** (1991) 233.

[58] B. Adeva *et al.*, L3 Collaboration, Nucl. Inst. and Meth. **A289** (1990) 33.

[59] K. Ahmet *et al.*, OPAL Collaboration, Nucl. Inst. and Meth. **A305** (1991) 275.

[60] LEP Design Report, vol.1: *The LEP Injector Chain*, CERN-LEP/83-29 (1983);
LEP Design Report, vol.2: *The LEP Design Report*, CERN-LEP/84-01 (1984).

[61] LEP Energy Working Group, *LEP energy calibration above the W pair production threshold*, Contribution to the 29th ICHEP, Vancouver, Canada, July 1998.

[62] LEP Energy Working Group, *Calibration of centre-of-mass energies at LEP1 for precise measurements of Z properties*, CERN-EP/98-040, CERN-SL/98-012, submitted to Eur. Phys. J.

[63] A.A. Sokolov and I.M. Ternov, Sov. Phys. Dokl. **8** (1964) 1203.

[64] J. Billan *et al.*, *Determination of the Particle Momentum in LEP from Precise Magnet Measurements*, Proc. of the 1991 Particle Accelerators Conference, San Francisco, USA, May 1991.

[65] LEP Energy Working Group, *LEP energy calibration in 1996*, LEP Energy Group/97-01;
`http://www.cern.ch/LEPECAL/reports/reports.html` .

[66] ALEPH Collaboration, *The ALEPH Handbook*, C. Bowdery (ed.), vol.1 (1995); vol.2 (1997). Published by CERN.

[67] D. Buskulic *et al.*, ALEPH Collaboration, Nucl. Inst. and Meth. **A360** (1995) 481.

[68] S. Jadach, W. Placzek, E. Richter-Wąs, B.F.L. Ward and Z. Wąs, Comput. Phys. Commun. **102** (1997) 229.

[69] P. Mató, *Data processing for Large* $e^+e^\perp$ *Experiments*, Ph.D. thesis, Universitat de Barcelona, Barcelona (1990).

[70] M. Delfino *et al.*, Comput. Phys. Commun. **57** (1989) 401.

[71] J. Knobloch, *JULIA Users and Programmers guide*, ALEPH internal report, ALEPH 90-11 (1990).

[72] H. Albrecht, E. Blucher and J. Boucrot, *ALPHA: Aleph Physics Analysis Package*, ALEPH internal report, ALEPH 97-058 (1997).

[73] D. Casper, *The ALEPH Tracking Upgrade. Part 1: VDET Global Pattern Recognition, Technical Documentation*, ALEPH internal report, SOFTWR 97-004 (1997).

[74] R. Frühwirth, HEPHY-PUB 503/87 (1987).

[75] B. Bloch-Devaux *et al.*, *KINGAL Users Guide*, ALEPH internal report, ALEPH 87-53 (1988).

[76] R. Brun *et al.*, *GEANT3 Users Guide*, CERN-DD/EE/84-1 (1987).

[77] F. Ranjard, *GALEPH-Monte Carlo program for ALEPH*, ALEPH internal report, ALEPH 88-119 (1988).

[78] H. Fesefeldt, *GHEISHA*, Aachen 3rd Inst. Nucl. Phys. **A23** (Proc. Suppl.) (1991) 291.

[79] M. Skrzypek, S. Jadach, W. Placzek and Z. Wąs, Comput. Phys. Commun. **94** (1996) 216.

[80] M. Skrzypek *et al.*, Phys. Lett. **B372** (1996) 289.

[81] E. Barberio and Z. Wąs, Comput. Phys. Commun. **79** (1994) 291.

[82] I.G. Knowles and T. Sjöstrand, *Physics at LEP2*, G. Altarelli, T. Sjöstrand and F. Zwirner (eds.), CERN 96-01 (1996) vol.2, 103.

[83] F.A. Berends, G. Burgers and W.L. Van Neerven, Phys. Lett. **B185** (1987) 395;
Nucl. Phys. **B297** (1988) 429; Nucl. Phys. **B304** (1988) 921.

[84] D. Buskulic *et al.*, ALEPH Collaboration, Phys. Lett. **B313** (1993) 509.

[85] S. Jadach, B.F.L. Ward and Z. Wąs, Comput. Phys. Commun. **79** (1994) 466.

[86] H. Anlauf *et al.*, Comput. Phys. Commun. **79** (1994) 466.

[87] W. Bartel *et al.*, JADE Collaboration, Z. Phys. **C33** (1986) 23;
S. Bethke, Habilitation thesis, LBL 50-208 (1987).

[88] S. Catani *et al.*, Phys. Lett. **B269** (1991) 432.

[89] C. Guicheney *et al.*, *WW cross-section measurement at 172 GeV using a Neural Network*, ALEPH internal report, ALEPH 97-053 (1997).

[90] C. Guicheney *et al.*, Nucl. Inst. and Meth. **A362** (1995) 478;
C. Guicheney *et al.*,
`http://alephwww.cern.ch/~guichene/ww_tools/version13.html` .

[91] D. Buskulic *et al.*, ALEPH Collaboration, Phys. Lett. **B313** (1993) 535.

[92] T. Sjöstrand, Comput. Phys. Commun. **28** (1983) 227.

[93] Z. Kunszt and P. Nason, *Z Physics at LEP 1*, G. Altarelli, R. Kleiss and C. Verzegnassi (eds.), CERN 89-08 (1989) vol.1, 373.

[94] A. Trabelsi, P. Pérez and J. Schwindling, *W mass reconstruction at LEP 200 using $WW \to QQQQ$ events*, ALEPH internal report, ALEPH 94-73 (1994);
A. Tilquin, *Constrained fit and Initial State Radiation in Four Jet Events at LEP II*, ALEPH internal report, ALEPH 95-129 (1995);
A. Tilquin *et al.*,
`http://alephwww.cern.ch/LEP2ANALYSIS/WTF/code/mathkine.doc` .

[95] A. Blondel, Private communication, 22 April 1997.

[96] A. Moutoussi,
`http://alephwww.cern.ch/~moutouss/ww/wpairs.html` .

[97] A. Trabelsi, *Direct* W *mass measurement from 170 and* 172 GeV *data*, ALEPH internal report, ALEPH 97-025 (1997).

[98] S. Goodsir, Ph.D. in progress.

[99] A. Juste, *Measurement of the W mass in* $e^+e^\perp$ *annihilation*, Ph.D. thesis, Universitat Autònoma de Barcelona, Barcelona (1998).

[100] G. Boix *et al.*, *W mass measurement in the four jet channel using a MC reweighting technique*, ALEPH internal report, ALEPH 97-067 (1997).

[101] M. Vreeswijk,
`http://alephwww.cern.ch/~jezeques/WmassWeiKWCC03.F` .

[102] D. Bardin *et al.*, Nucl. Phys. **B37** (1994) 148;
D. Bardin *et al.*, *GENTLE/4fan v2.0 – A program for the Semi-Analytic Calculation of Predictions for the Process* $e^+e^\perp \to 4f$, Comput. Phys. Commun. **104** (1997) 161.

[103] R. Barate *et al.*, ALEPH Collaboration, Phys. Rep. **294** (1998) 1.

[104] A. Trabelsi, *Mesure de la masse du boson W± dans l'expérience ALEPH du LEP*, Ph.D. thesis, Université de la Mediterrannée, Marseille (1997).

[105] F. Ligabue,
`http://alephwww.cern.ch/~ligabue/syst/syst.html` .

[106] M.N. Minard, Private communication, 12 March 1997.

[107] R.M. Barnett *et al.*, Phys. Rev. **D54** (1996) 1.

[108] D.R. Yennie, S.C. Frautschi and H. Suura, Annuals of Phys. **13** (1961) 379; S. Jadach and B.F.L. Ward, TPJU - 15/88 (1988).

[109] I. Riu, *W mass Background Systematic Study using Z peak data*, ALEPH internal report, ALEPH 97-060 (1997).

[110] G. Gustafson, U. Pettersson and P. Zerwas, Phys. Lett. **B209** (1988) 90; G. Gustafson and J. Häkkinen, Z. Phys. **C64** (1994) 659.

[111] S. Jezequel, `http://alephwww.cern.ch/~jezeques/bose.F` .

[112] R. Barate *et al.*, ALEPH Collaboration, Phys. Lett. **B422** (1998) 384.

[113] C. Guicheney *et al.*, `http://alephwww.cern.ch/~guichene/ww_tools/version17.html` .

[114] P. Azzurri *et al.*, *WW cross-section and W branching ratios at* $\sqrt{s} = 183$ GeV, ALEPH internal report, ALEPH 98-078 (1998).

[115] O. Buchmüller, Private communication, 25 May 1997.

[116] O. Buchmüller *et al.*, *On Colour Rearrangement Effects in Hadronic WW Events - Predictions of the HERWIG and VNI Generators* -, ALEPH internal report, ALEPH 98-059 (1998).

[117] R. Barate *et al.*, ALEPH Collaboration, *Measurement of the W mass in* e^+e^- *Collisions at* 183 GeV, paper in preparation.

[118] D. Karlen, *Experimental Status of the Standard Model*, Contribution to the 29th ICHEP, Vancouver, Canada, July 1998.

[119] K. McFarland *et al.*, CCFR Collaboration, Eur. Phys. J. **C1** (1998) 509.

[120] The NuTeV, D0, CDF Collaborations, *Precision Measurement of* $\sin^2\theta_W$ *from* νN *Scattering at NuTeV and Direct Measurements of* M_W, Fermilab-Conf-98-200-E, to be published in the proceedings of the 6th international workshop of Deep Inelastic Scattering, Brussels, Belgium (1998);
T. Bolton, Contribution to the 29th ICHEP, Vancouver, Canada, July 1998.

[121] E.A. Paschos and L. Wolfenstein, Phys. Rev. **D7** (1973) 91.

[122] D.Yu. Bardin, V.A. Dokuchaeva, JINR-E2-86-260 (1986).

[123] V. Blobel in: European Physical Society, *Formulae and methods in experimental data evaluation*, vol.3 (1984) p. L1.

[124] J.B. Hansen, *Triple Gauge-boson Couplings in W pair Production via* e^+e^- *Annihilation*, Ph.D. thesis, Niels Bohr Institute, Copenhagen (1996).

[125] K. Hornik, M. Stinchcombe and H. White, *Neural Networks* **2** (1989) 359;
J.A. Hertz, A. Krogh and R.G. Palmer, *Introduction to the theory of neural computation*, Addison-Wesley, Redwood City CA (1991);
B. Müller and J. Reinhardt, *Neural networks: an introduction*, Springer-Verlag, Berlin (1991).

[126] Y. Le Cun, Proc. Cognitiva **85** (1985) 599.

[127] V. Gaitan, *Neural Networks in High Energy Physics: From Pattern Recognition to Exploratory Data Analysis*, Ph.D. thesis, Universitat Autònoma de Barcelona, Barcelona (1993).

[128] V. Breton *et al.*, Nucl. Inst. and Meth. **A362** (1995) 478.